Coherent Structures in the Atmospheric Boundary Layer Measured by Dual Doppler Lidar

Zur Erlangung des akademischen Grades
Doktor der Naturwissenschaften
der Fakultät für Physik
Karlsruher Institut für Technologie (KIT)

genehmigte
Dissertation
von

Dipl.-Met. Thomas Damian

Tag der mündlichen Prüfung:	13. Mai 2016
Referent:	Prof. Dr. Christoph Kottmeier
Korreferent:	PD Dr. Michael Kunz

Abstract

Coherent structures describe areas in a fluid, where a turbulent variable like wind speed or temperature exhibits a high correlation with itself or another variable. These organized motions are subject of current research as they have an impact on turbulent fluxes and thereby influence mixing and transport processes within the atmospheric boundary layer. In recordings of the horizontal wind field, coherent structures manifest as distinct regions of reduced and enhanced wind speed. A dual-Doppler lidar setup in a synchronized scan-mode enables to measure the horizontal wind field in the atmospheric surface layer. Measurements are conducted during the HOPE field campaign in April and May 2013 in Jülich, Germany. Using a synchronized dual-Doppler lidar setup yields in a wind field data set with a 12 s temporal resolution and a 60 m horizontal resolution. The measurement domain is aligned as a tilted plane with a coverage of 10 km^2 located at altitudes between 55 m agl and 155 m agl. Within 320 hours, coherent structures occur frequently and exhibit various appearances and characteristics.
This thesis aims to characterize coherent structures in the horizontal wind field and focuses on the identification of triggering mechanisms of coherent structure formation. Developing a characterization method which describes coherent structures in regards to their intensity and their horizontal extent allows to compare coherent structures to the underlying meteorological conditions. This enables to conclude that the formation of coherent structures depends on buoyantly-driven turbulence as well as mechanically-generated turbulence. The presence of coherent structures in general follows a diurnal cycle. Mostly during nighttime – within a stably stratified environment – coherent structures do not tend to form. In a neutrally stratified boundary layer in the morning, low-intensity turbulence arises. Increasing buoyantly-driven turbulence leads to coherent structures for-

mation within daytime hours. In the evening when buoyancy decays, coherent structures revert to low-intensity turbulence and vanish at night. In the absence of buoyancy, occurring structures within a neutrally and stably stratified boundary layer are related to mechanically-generated turbulence and appear to be smaller than 1 km. During daytime from 06:00 UTC to 18:00 UTC, about 50 % of all coherent structures are longer than 1 km, whereas during nighttime the wind field mostly exhibits homogeneity ($\approx 50\,\%$).

Applying a threshold-based automated detection method enables quantitative analysis regarding the length and the elongation of the coherent structures and generally agrees with the findings gained from the manual characterization. Under unstable conditions, large coherent structures are able to form; the longest structures occur, when the sensible heat flux is between $50\,\mathrm{W\,m^{-2}} \leq H_0 \leq 80\,\mathrm{W\,m^{-2}}$. Increasing values of friction velocity correlate with the length of the structures, indicating that very large coherent structures $\geq 2\,\mathrm{km}$ rather depend on mechanically-generated turbulence than on buoyancy-driven turbulence. In a shear-driven environment, the elongation of the coherent structures also increases, forming streak-like coherent structures. Quantitatively, the median of the length of all detected coherent structures during daytime is 1312 m, 959 m during nighttime, and 883 m in the morning and evening hours. The aspect ratio during daytime (2.1), during nighttime (1.9), and in the morning and the evening (1.8) indicates that the most elongated structures occur during daytime.

Additional lidar measurements provide information on the three-dimensional coherent structures. In the framework of a case study, the development of the boundary layer within the morning hours reveals that the length of the coherent structures depends on the height of the mixed layer. A strongly sheared situation within an unstably stratified boundary layer yields the hypothesis that shear-generated coherent structures form in the surface layer, whereas buoyancy supports an upward movement of coherent structures within their life-cycle. Coherent structures with small aspect ratios occur under calm wind situations in the presence of strong buoyancy. These structures form approximately cellular hexagonal patterns and are driven by distinct up- and downdrafts.

All analysis support the notion of a conceptual model summarizing coherent structure formation processes within the atmospheric boundary layer. Mechanically-driven coherent structures are generated by eddies occurring in the lowest part of the boundary layer due to wind shear. In an unstably, respectively neutrally stratified boundary layer, shear occurs within the surface layer, whereas an unstably stratified boundary layer often provides shear also at higher altitudes. During daytime buoyancy is able to form eddies with the size of the mixed layer, which are considerably larger. The conceptual model suggests that the length of coherent structures depends on the size of the corresponding eddies.

Contents

1 Introduction

> *Big whorls have little whorls, that feed on their velocity;*
> *And little whorls have lesser whorls, and so on to viscosity.*

Lewis Fry Richardson, *Meteorologist*, 1881 – 1953

The atmosphere in which we live constantly changes and meteorological parameters exhibit fluctuations, defining atmospheric turbulence. The random and chaotic changes are entirely unpredictable, making them simultaneously fascinatingand for atmospheric researchers challenging to analyse. Like many state variables in the atmosphere, moving air also exhibits turbulence. The atmospheric boundary layer is characterized by eddies of many different sizes, from viscous eddies to large eddies, covering the whole extent of the boundary layer. These eddies are responsible for transfer processes of heat, moisture, and momentum taking place in boundary layer flows. In 1922, the meteorologist Lewis Fry Richardson introduced the notion of the energy cascade (Richardson, 2007). The poem by Richardson depicts the interaction between eddies of different sizes and the transport of energy from large scale eddies to small scale eddies, finally dissipating into heat at the inertial subrange (Kolmogorov, 1941). Atmospheric turbulence can be mechanically generated by the friction of the earth's surface, or buoyantly-driven by surface heating during daytime hours. Deardorff (1983) described the processes of convection and condensation, as well as internal sources of turbulent kinetic energy relevant for the production of turbulence.

Coherent structures are quasi-periodic fluctuations in turbulent environments that can be found in many meteorological quantities, including temperature, humidity, and wind recordings (Grant, 1958). A turbulent coherent variable exhibits organized fluctuations in terms of time and space. Point measurements of the wind speed, for example, reveal coherent structures as wave-like and ramp-like patterns (Barthlott et al., 2007). The mathematical method of Reynolds-averaging accounts for turbulent processes, as every turbulent state variable is separated into two parts: the average and the fluctuation. Other than stochastic turbulence, coherent structures exhibit quasi-periodic fluctuations. Most atmospheric models are based on Reynolds-averaged Navier-Stokes equations, considering prevalent coherent structures as stochastic turbulence. If it were possible to construct a general parametrization describing coherent structures enabling a separation from the stochastic turbulence.

In wind fields, coherent structures were first observed in laboratory experiments related to low Reynolds-number flows (Grant, 1958). In the past decades, many simulations and measurements have been conducted to observe and analyse coherent structures in the atmosphere. Adrian et al. (2000) used a shear-driven simulation of hairpin-like structures under statically neutral conditions, analysing the impact of the structures in the boundary layer. Moeng and Sullivan (1994) addressed a different approach by simulating streak-like coherent structures within a shear-driven unstably stratified boundary layer. Feingold et al. (2010) investigated coherent structures with a hexagonal shape in simulations of a buoyantly-driven boundary layer in the absence of shear. Below the hexagonal shape, up- and downdraft areas with converging and diverging wind fields are characteristic.

Many in-situ measurements of coherent structures are based on point measurements of meteorological towers (Thomas and Foken, 2005; Barthlott et al., 2007). Using Taylor's hypothesis of frozen turbulence allows researchers to transfer coherent structures into the spatial domain. In-situ methods provide time series of a quantity as point measurements. Spatially distributed measurements require a

serious amount of measurement systems. For the purpose of coherent structure research, Inagaki and Kanda (2010) placed 40 sonic anemometers in order to apply a two-dimensional analysis within a horizontal domain, and then compared the results to the output of a COSMO model. They were able to detect two-dimensional coherent structures with a streak-like appearance.

Remote sensing instruments use indirect methods to measure quantities over large distances and therefore have advantages regarding the flexibility compared to in-situ measurements. Doppler lidar (*Light Detection and Ranging*) systems use highly coherent laser light to detect air movement within the atmospheric boundary layer. A scanner is able to direct the laser light into the upper half hemisphere in a flexible manner. Aerosol and dust particles moving with the wind reflect the light. The Doppler effect causes a shift in frequency, which allows observers to determine the movement of the particles relative to the lidar. In this way, a lidar is able to measure the one-dimensional wind component along the beam line over distances $> 10\,\mathrm{km}$. Using two Doppler lidars within a dual-Doppler lidar setup provides two independent wind components, allowing researchers to determine the horizontal wind speed. Newsom et al. (2008) combined two lidar systems and were able to observe coherent structures. Based on this idea, Stawiarski (2014) developed an algorithm to ensure high quality measurements for any future coherent structure research.

The Institute of Meteorology and Climate Research (IMK-TRO) at the Karlsruhe Institute of Technology (KIT) operates two Doppler lidars within the KITcube monitoring system (Kalthoff et al., 2013). Using precise temporal and spatial synchronisation of both lidars, the dual-Doppler setup provides measurements of the horizontal wind field with a 12 s temporal resolution and a 60 m horizontal resolution. Within the High Definition Clouds and Precipitation for Advancing Climate Prediction (HD(CP)^2) research project, the HD(CP)^2 Observation Prototype Experiment (HOPE) field campaign was conducted in April and May 2013 in Jülich, Germany. All in all, the system was operated for 300 hours and covered

a domain of 10 km^2.

In the scope of this thesis, a dual-Doppler scan algorithm was developed for the application during the HOPE campaign. The overall objective is the understanding of how coherent structures are able to form in a turbulent boundary layer. Therefore, triggering mechanisms for the formation of coherent structures need to be identified. Because the dual-Doppler wind measurements contain coherent structures under various meteorological conditions, the manual application of a characterization method reveals buoyantly-driven turbulence and mechanically-generated turbulence as two highly relevant processes for coherent structure formation. As a counterpart to the manual analysis and to gain more information about the behaviour of coherent structures, an automated detection method is demanded for an independent analysis. The dual-Doppler measurements provide two-dimensional information regarding the horizontal wind vector. For this reason, the recordings of two additional lidar systems during HOPE are used when examining the three-dimensional appearance of coherent structures.

The outline of this study is as follows: Chapter 2 introduces boundary layer meteorology, gives a comprehensive overview of the current research on coherent structures, and introduces a conceptual model describing processes relevant for the formation of coherent structures. Chapter 3 explains the lidar measurement principle and presents the contribution of IMK-TRO at the HOPE field campaign. The development and application of a manual characterization scheme accounting for the variety of coherent structures that occur within the whole data set is presented in Chapter 4. Chapter 5 describes an automated detection method used to automatically create a coherent structure data base applicable for analysis regarding both the coherent structure appearance and the prevailing meteorological conditions. Chapter 6 presents analysis regarding the vertical shape of coherent structure in the framework of case studies. The conclusions of all studies are depicted in Chapter 7.

2 Coherent Structures in the Atmospheric Boundary Layer

Coherence, originating from the Latin expression 'cohaerere', describes a logical and orderly relation of parts. Within the atmospheric boundary layer, turbulence in general is chaotic. However, coherent structures cause organized quasi-periodic fluctuations in a turbulent time series. This chapter summarizes basic knowledge on boundary layer turbulence and explains the phenomenon of coherent structures in atmospheric measurements.

2.1 Atmospheric Boundary Layer Turbulence

In physics and fluid mechanics, the boundary layer describes an area where a fluid is bounded by a surface. The atmospheric boundary layer is affected by the presence of the earth's surface inducing mechanically-generated turbulence to the motion of the air (Prandtl et al., 1990). Stull (1988) defined the atmospheric boundary layer as the part of the troposphere that is directly influenced by the presence of the earth's surface and responds to surface forcing within a time period of about an hour or less. Above a certain distance from the ground, the atmosphere is no longer affected by it; this height defines the free atmosphere. The boundary layer height z_i can range from hundreds of meters to a few kilometers (Stull, 1988).

The boundary layer characteristics exhibit a diurnal cycle that is dependent on the radiation intake throughout the day. Figure 2.1 illustrates the diurnal evolution of the atmospheric boundary layer under fair weather conditions over a flat, homogeneous terrain. During the daytime, the turbulence in the mixed layer generally is convectively driven. Even in regions with strong winds, a well-mixed

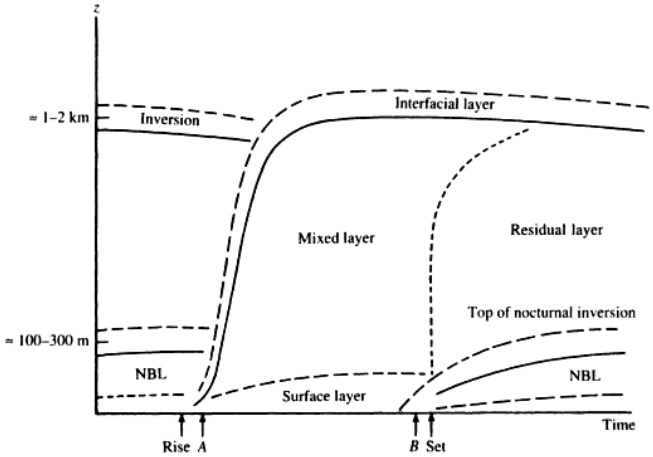

Figure 2.1: Diurnal atmospheric boundary layer evolution over horizontally homogeneous and flat terrain under fair weather conditions (Garratt, 1994).

layer is able to form. Convection is a feature of an unstable stratification, when the prevailing local temperature gradient Γ_u is high compared to the dry adiabatic lapse rate, i.e. $\Gamma_u \geq \Gamma_d = 9.8\,\mathrm{K\,km^{-1}}$ (Stull, 1988). A main source for buoyancy is heat transfer from the ground and yields an unstable stratification near the surface. Due to solar heating at the ground, shortly after sunrise, the mixed layer grows in depth and reaches its maximum in the afternoon, where it is intensively mixed by warm air thermals rising from the ground. Above the mixed layer lies the entrainment zone, which, as a stable layer, restrains air masses from reaching further. In the mixed layer the vertical profile of the horizontal wind speed is roughly constant. The surface layer normally ranges up to 100 m agl. In the surface layer, the mean wind speed increases – from zero at the ground – nearly logarithmically with height and yields a sheared wind profile.

Due to surface cooling in the evening, the thermals in the mixed layer stop rising and turbulence decays. In the former mixed layer, many state variables and concentrations stay the same; this layer is often called the residual layer. At the bot-

tom of the residual layer, the nocturnal boundary layer begins forming at sunset and continues on. The nocturnal boundary layer stabilizes, leading to a nocturnal stable stratification. A stable stratification is characterized by the temperature gradient $\Gamma_s \leq \Gamma_d$. Within the nocturnal boundary layer, a phenomenon called the nocturnal low-level jet may appear (Kottmeier, 1982; Banta et al., 2002; Damian et al., 2014). When the air masses stabilize, the mean flow is able to decouple from the ground friction, which may lead to super-geostrophic wind speeds. Nocturnal jets enhance the wind shear and generate turbulence that may occur in relatively short bursts and can lead to mixing processes within the nocturnal stable layer.

In the boundary layer, turbulence is responsible for transport processes of several quantities, i.e. heat, moisture, and momentum. Deardorff (1983) distinguished between four different turbulence formation mechanisms: (a) the wind shear at the earth's surface, (b) the wind shear at the transition from the atmospheric boundary layer to the free atmosphere, (c) convection, and (d) internal sources of turbulent kinetic energy e.g. condensation processes in clouds. In this study the mechanically-driven turbulence (a) and (b) is as important as the turbulence driven by convection (c). No internal processes (d) will be part of this study.

The Turbulent Kinetic Energy (TKE) is a key variable in boundary-layer meteorology because it gives a measure of the intensity of turbulence (Stull, 1988). All physical processes generating turbulence – i.e. momentum, heat, and moisture transport – draw up a budget in equation 2.1:

$$\underbrace{\frac{\partial \overline{e}}{\partial t}}_{\text{I}} + \underbrace{\overline{U}_j \frac{\partial \overline{e}}{\partial x_j}}_{\text{II}} = \underbrace{\delta_{i3} \frac{g}{\overline{\theta}_v} \left(\overline{u_i' \theta_v'}\right)}_{\text{III}} - \underbrace{\overline{u_i' u_j'} \frac{\partial \overline{U}_i}{\partial x_j}}_{\text{IV}} - \underbrace{\frac{\partial \left(\overline{u_j' e}\right)}{\partial x_j}}_{\text{V}} - \underbrace{\frac{1}{\overline{\rho}} \frac{\partial \left(\overline{u_i' p'}\right)}{\partial x_i}}_{\text{VI}} - \underbrace{\varepsilon}_{\text{VII}} \tag{2.1}$$

$\overline{e} = \frac{1}{2}\overline{u_i'^2}$ represents the turbulent kinetic energy, u_i is the wind speed in i-direction, g the gravitational constant, θ_v the virtual potential temperature, ρ the air's density, p the air pressure and ε the dissipation. The explanation of all

terms of the equation is as follows: (I) describes the local TKE storage, (II) is the TKE advection with the mean wind, (III) represents the buoyant TKE production, (IV) is the mechanical or shear TKE production term, (V) represents the turbulent TKE transport, (VI) is the pressure correlation term, and (VII) describes the TKE dissipation.
A velocity scale called friction velocity u_* is an estimation of wind shear near the ground on the turbulence of the boundary layers (Stull, 1988).

$$u_* = \left(\overline{u'w'_s}^2 + \overline{v'w'_s}^2\right)^{\frac{1}{2}} \tag{2.2}$$

In this formula, w_s stands for the vertical wind speed near the surface.
The Obukhov length L is a frequently used scaling parameter for meteorological purposes in the surface layer and originates from the third term of the TKE equation (Equation 2.1) divided by $-\frac{\kappa}{u_*^3}$, where the von-Karman constant κ is a dimensionless number with values between 0.35 and 0.42, frequently used as 0.4 (Stull, 1988).

$$L = \frac{-\overline{\theta}_v u_*^3}{\kappa g \left(\overline{w'\theta'_v}\right)_s} \,. \tag{2.3}$$

Using the Obukhov length a stability parameter ζ can be established:

$$\zeta = \frac{z}{L} \,, \tag{2.4}$$

where z is the measuring height above surface level. Negative values represent an unstable stratification while positive values indicate a stable stratification.
Another important measure to quantify the turbulence in the atmospheric surface layer is given by the Bulk Richardson Number Ri (Oke, 1993):

$$Ri = \frac{g}{\overline{T}} \frac{(\Delta\overline{T}/\Delta z)}{(\Delta\overline{u}/\Delta z)^2} \tag{2.5}$$

Positive and negative values of Ri represent a stably, respectively unstably stratified boundary layer. $Ri = 0.1$ point out neutral boundary layer conditions. In-

terpreting Ri according to Thom et al. (1975) allowed quantification of the atmospheric mixing. Mixed convection can be found, when $-0.01 > Ri > -1$. Richardson Numbers $Ri < -1$ correspond to free convection in the boundary layer.

The dimensionless Reynolds number is an important variable to ensure the transferability between different experiments. This value is the ratio between inertia forces and viscous forces and describes the relationship between the range of turbulence.

$$Re = \frac{VL}{\nu} = \rho \frac{VL}{\mu} , \tag{2.6}$$

with V and L representing the velocity and the length scales in the boundary layer, ν the dynamic and μ the kinematic viscosity, and ρ the fluids' density. With $\nu_{\text{air}} \approx 1.5 \cdot 10^{-5}\,\text{m}^2\,\text{s}^{-1}$, $V = 5\,\text{m}\,\text{s}^{-1}$, and $L = 100\,\text{m}$, a Reynolds number of $Re_{\text{asl}} \geq 3 \cdot 10^7$ represents the turbulence in atmospheric surface layer. Laboratory conditions work with much smaller Reynolds numbers $Re_{\text{lab}} \approx 10^3$ (Stull, 1988).

2.2 Organized Structures in a Turbulent Flow Field

The conversion of kinetic energy of the mean flow into turbulent fluctuations, as well as the dissipation into internal energy by viscous effects are continuous processes, which lead to a self-sustaining turbulent boundary layer in the absence of stabilizing effects (Robinson, 1991). This section introduces to coherent structures and summarizes the current state of research. The development of a conceptual model, based on the influence of buoyancy-driven turbulence as well as shear-generated turbulence, describes coherent structures formation processes and anticipates, how coherent structures manifest in the atmospheric boundary layer.

2.2.1 Definition

Many studies contributed to the knowledge of coherent structures and describe different theories of how these structures affect the atmospheric boundary layer.

Coherent structures are also known as organized structures or organized motions. For many decades, many studies have been conducted to gain more information on coherent structure characteristics.
Stawiarski (2014) collected seven definitions, and stated that most of these definitions are either too vague to allow comparable quantitative results, too dependent on the use of a certain detection method, or require highly resolved information on at least one variable of the fluid within a certain volume. Robinson (1991) defined a coherent structure as:

> *[...] a three-dimensional region of the flow over which at least one fundamental flow variable (velocity component, density, temperature, etc.) exhibits significant correlation with itself or with another variable over a range of space and/or time that is significantly larger than the smallest local scales of the flow.*

The definition of Adrian (2007) said that:

> *Coherent motions can be thought of as individual entities if they persist for long times, i.e., if they possess temporal coherence. By virtue of fluid continuity, all motions possess some degree of spatial coherence, so coherence in space is not sufficient to define an organized motion. Only motions that live long enough to catch our eye in a flow visualization movie and/or contribute significantly to time-averaged statistics of the flow merit the study and attention we apply to organized structures.*

The development of the following definition specifies kinematic flow properties on the purpose of recognizing coherent structures within the horizontal wind field, as used in this thesis. This definition is inspired by Robinson (1991) and Adrian (2007).

Coherent structures in the wind field manifest as quasi-periodic, distinct regions of enhanced or reduced wind speed. Coherent structures are temporally coherent, as they can be identified continuously in subsequent measurements. Spatial

coherence is given on the convective scale.

This definition allows to characterize coherent structures in terms of spatial coherence and long-liveness. Further the distinctiveness and the recurrence are important criteria in recognizing coherent structures in a horizontal wind field data set.

2.2.2 State of Research

Coherent structures were first observed in laboratory experiments with flows at low Reynolds numbers. In wall-bounded flows, the turbulent shear flow showed ordered structures in the wind component (Grant, 1958; Kline et al., 1967). According to Head and Bandyopadhyay (1981) it has been shown that organizational patterns of turbulent processes also occur in flows with high Reynolds numbers ($Re = 9000$) in the shape of hairpin structures. The model of an individual hairpin structure represents a simple coherent structure that explains many of the features observed in wall-bounded flows (Theodorsen, 1952; Adrian et al., 2000). Head and Bandyopadhyay (1981) proposed that hairpin structures occur in groups. Adrian (2007) had developed a conceptual scenario of hairpins attached to the wall that grow in an environment of overlying larger hairpin packets. However, Adrian (2007) also stated that it is still unclear whether the model of hairpin-packets is valid within a shear-driven atmospheric boundary layer. Many studies have dealt with organized motions in low-Reynolds number flows under laboratory conditions, but are not transferable to high Reynolds number flows as can be found in the atmospheric boundary layer.

Analysis of Simulation Data

Turbulent motion consists of eddies in a large range of scales, from a few millimeters up to the extent of the boundary layer. Meteorological simulations are unable to resolve all scales at once. Simulations are primarily realized using Direct Numerical Simulation (DNS) or Large Eddy Simulation (LES). DNS models

are able to resolve a huge range of different scales and therefore need enormous computational resources, whereas LES models only resolve turbulent motions down to a filter scale in the range of a few meters and parametrize all processes on smaller scales. Coherent structures are not yet considered in sub-filter-scale parametrizations used in weather forecast models (Doms et al., 2011). According to Hussain (1983) and Hellsten and Zilitinkevich (2013) a parametrization using a triple-decomposition of the flow field into the average flow, the organized turbulence, and the random turbulence could enhance the performance of mesoscale forecast models.

In the past decades, many studies using simulations based on DNS and LES have focused on coherent structure research. Moeng and Sullivan (1994) showed streaky structures using an LES model and compare shear- and buoyancy-driven boundary layer flows regarding the containing structures. A boundary layer dominated by shear forms streaks orientated along the mean wind direction with regions of alternating high- and low-speed fluid. The correlation of u' and w' is analogue to the ejections and sweeps introduced in Section 2.2.3. The structures in a buoyantly-driven boundary layer are dominated by updrafts whose sizes are in the order of the boundary layer depth z_i. The combination of turbulence by shear and buoyancy yields a series of roll-like structures, which are spaced about $3z_i$ apart. Lin et al. (1996) have also reproduced streaky structures related to the ejections and sweeps using an LES model. This study suggests that the formation of coherent structures begins in the surface layer. While the structures move upwards during their lifecycle, they stay aligned with the mean wind. By calculating isosurfaces of vorticity surrounding of conditional eddies, the streaks could be related to hairpin structures with length scales of $0.2z_i$, comparable to those from DNS simulations in a low-Reynolds number regime (Adrian, 2007). The study of Lin et al. (1997) examined the effects of surface roughness on flow structures in a neutrally stratified boundary layer. They derived an equation for the streak-spacing dependent on the boundary layer height under neutral conditions. Furthermore Lin et al. (1997) investigated the strength of eddies and found that an increase in surface roughness also increases the strength and the distribution den-

sity of all investigated structures. They also clarify that the movement of some ejections and vortical structures in the outer layer causes the internal boundary layer to grow. Khanna and Brasseur (1998) analysed an unstable boundary layer using LES methods and reveal three-dimensional structures of buoyancy-induced updrafts from a turbulent Rayleigh-Bénard (Rayleigh, 1916) cellular pattern with a lengthscale of z_i. Furthermore, this study denotes that shear-induced regions of high- and low-speed-flows are the dominant energy-containing motions in a near-neutral stratified boundary layer. The work of Feingold et al. (2010) stated that cellular patterns can be caused in two different ways. Closed-cell structures are driven by cooling at the upper boundary layer and often yield a cloud formation, whereas open-cell structures are induced by surface heating. Thereby closed cellular structures are broader buoyant updraft regions, which are surrounded by stronger negatively buoyant downdrafts, and open-cell structures are narrow updrafts surrounded by weaker downdrafts. Another related work (Hellsten and Zilitinkevich, 2013) mentions that these cellular structures exhibit a dominant contribution to the momentum flux ($\approx 90\,\%$). Drobinski and Foster (2003) investigated the dynamics of streak formations near to the surface in a neutrally stratified planetary boundary layer, aiming to associate streaks in the mean wind with non-normal optimal perturbations (LeMone and Pennell, 1976). The LES model that the work of Kim and Park (2003) is based on is strongly sheared and with a convectively-driven boundary layer; the researchers discovered that low speed and high temperature streaks are a consequence of momentum and heat transport by vortical motions.

Stawiarski et al. (2015) used an LES data set (Raasch and Schröter, 2001) to ascertain whether dual-Doppler lidar measurements can be used to detect and quantify coherent structures in the atmospheric surface layer. The implementation of virtual lidar measurements within the LES model results in another horizontal wind field, simulating the dual-Doppler lidar measurements as well as the application of a dual-Doppler retrieval method (Newsom et al., 2005; Stawiarski et al., 2015). By balancing the temporal resolution with the horizontal resolution in dependence to the mean wind speed, Stawiarski et al. (2015) created an appli-

cable method which guarantees the best possible temporal and spatial resolution (see Chapter 3.2.3). In the scope of this thesis, the spatial resolution varied in the range between 60 m and 78 m, whereas the temporal resolution is balanced between 12 s and 14 s.

Coherent Structures Observations

Observations of coherent structures are always restricted to the capabilities of the instruments used for measurements. In-situ tower measurements and eddy-covariance measurements provide data with high temporal resolution as point measurements. Taylor's hypothesis of frozen turbulence (Stull, 1988) leaves the chance to transfer point measurements into spatial signals along mean wind direction yielding one-dimensional information of coherent structures. Many studies used time series of wind speed and temperature data, in combination with detection algorithms to characterize coherent structures. The wavelet analysis method (Collineau and Brunet, 1993) is frequently used to investigate the contribution of coherent structures to turbulent fluxes and TKE. Segalini and Alfredsson (2012) compared two detection methods suitable for coherent structure detection and prove the general applicability of wavelet analysis methods. Barthlott et al. (2007) summarized the results of previous studies applying the wavelet detection methods to in-situ measurements and found that the contributions to fluxes are varying in the range between 26 % and 108 %. Barthlott et al. (2007) pointed out that structures under stable conditions appear more often than under unstable conditions, but with shorter lengths. Thomas and Foken (2005) and Barthlott et al. (2007) examined that more elongated structures correlate with more unstable situations. Zeeman et al. (2013) investigated the connection between below- and above-canopy scalar time series data in three forests with different canopy architectures.

In-situ measurements are perfectly applicable for turbulence research and commonly used for studies regarding coherent structures. Two- or even three-dimensional interpretations generally are not possible. Inagaki and Kanda (2010)

aligned 40 sonic anemometers horizontally on a flat plane and compared the velocity fluctuations to a Consortium for Small-scale Modeling (COSMO) model. They were able to detect streaky structures in the measurement data set and also in the COSMO model. Applying a spatial filtering method leads to a decomposition in active and inactive contribution to the fluctuation.

Generally, using numerous in-situ measurements is quite inapplicable. Therefore, remote sensing instruments have been used increasingly for coherent structure analysis. Drobinski et al. (1998) were using measurement data from lidar, anemometers, radiosoundings, and sodars to capture organized large eddies or rolls in the atmospheric boundary layer. This study reveals thermal stratification and wind shear as two important factors for the eddies' characteristics. Newsom et al. (2008) deployed two Doppler lidars in a dual-Doppler mode to investigate the structure and the evolution of the surface-layer flow over a suburban area. Within these measurements they detected streaky structures that were elongated in the mean wind direction. Using Finite-time Lyapunov Exponent (FTLE) (Shadden et al., 2005), Tang et al. (2011, a,b) were able to measure Lagragian coherent structures and vertical gusts. They also detect footprints of hairpin structures on an airport runway. Iwai et al. (2008) showed that surface-layer streaks are the starting point for horizontal convection rolls using a dual-Doppler lidar setup. Takimoto et al. (2013) used Particle Image Velocimetry (PIV) to analyse the horizontal cross-sections of turbulent wind tunnel flow and to retrieve the lengths and the aspect ratios of the observed structures. The work of Träumner et al. (2015) is based on the same dual-Doppler lidar data set as this thesis. By calculating the integral length scales in the mean- and cross-wind directions, they prove that a structure's appearance is dependent on both shear and buoyancy effects. For example, the aspect ratios of the structures vary considerably during calm weather situations (aspect ratio ≈ 1, round structures) and situations with wind speeds over $8\,\mathrm{m\,s^{-1}}$ (aspect ratio > 2, elongated structures). Eder et al. (2015) found evidence that mesoscale eddies, like coherent structures, affect the near-surface turbulent exchange and thus lead to nonclosure of surface energy balance measurements.

2.2.3 Driving Mechanisms for Coherent Structure Formation

The review of Young et al. (2002) suggested that there are at least five mechanisms that can cause coherent structures in the atmospheric boundary layer. (a) Shear-driven surface layer turbulence can form low-wind speed updrafts and high-wind speed downdrafts which are elongated in the streamwise direction (Khanna and Brasseur, 1998). (b) Structures with a comparable appearance can also arise regarding buoyantly driven turbulence. These structures have a distinctly different source of TKE (Moeng and Sullivan, 1994). (c) Coherent structures in the boundary layer also can be induced by gravity waves from within or above the mixed layer (LeMone and Meitin, 1984; Balaji et al., 1993). Young et al. (2002) described two more theories of how coherent structures are able to emerge: (d) streaks are generated by near-surface vortices and develop a dynamic instability and (e) an optimal initial perturbation can grow to counter-rotating vortices, which are tilted into the mean shear. Young et al. (2002), Kim and Park (2003), and Iwai et al. (2008) each referred to a relationship between the development of large-scale horizontal rolls and low-speed streak formations, so both phenomena can be linked to microfronts observed in ejection and sweep patterns or in ramp-like patterns in a time series of wind speed, temperature, and humidity (Barthlott et al., 2007; Takimoto et al., 2013). Furthermore, Müller et al. (1985) presented radiosonde data showing that inflection point instabilities in the cross-wind component during night preceding with unstable stratification playing a role in cloud-street development.

Young et al. (2002) stated that shear-generated vortices are strongly connected to the appearance of coherent structures. As the influence of shear changes during daytime, Figure 2.2 shows measurements which exemplarily illustrate the altitudes affected by wind shear at different times of day. The measurements of potential temperature in Figure 2.2(a) during daytime (08:00 UTC, 12:00 UTC, and 16:00 UTC; red curves) represent a statically unstable boundary layer, where the potential temperature near the ground is considerably higher compared to higher altitudes. The profile of the horizontal wind speed in Figure

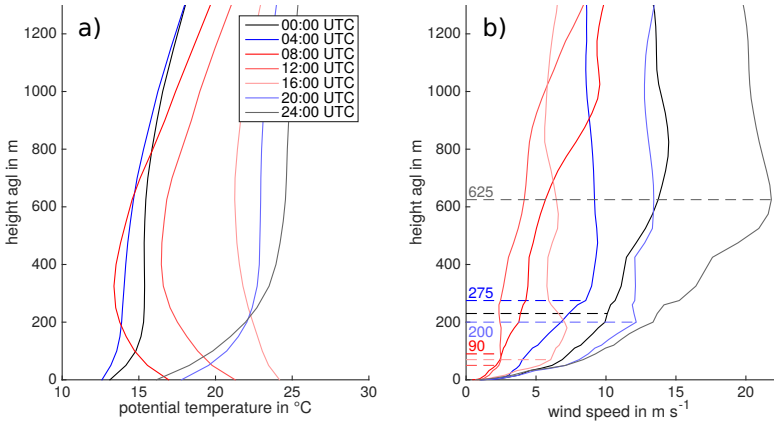

Figure 2.2: Illustration of shear height level at different times on 19 April, 2013. a) shows the vertical profile of the potential temperature measured by a microwave radiometer. b) presents measurements from different VAD-scans (lidar, see Section 3.1.3), which are combined to continuous profiles. The height levels represented by the dashed lines illustrate the shear influenced level for exemplary wind profiles.

2.2(b) shows that these times exhibit considerable shear within the lowest levels up to heights of about 100 m agl. From there on, the wind speed is constant with height (12:00 UTC) or increases inconsiderably (08:00 UTC, 16:00 UTC). After Stull (1988), the profile of the horizontal wind speed exhibits shear within the surface layer, which covers the lowest hundred meters of the atmospheric boundary layer. Measurements of the potential temperature in Figure 2.2(a) taken during nighttime or in the morning and the evening (00:00 UTC, 04:00 UTC, 20:00 UTC, and 24:00 UTC, black and blue curves) represent measurements of a stably stratified boundary layer. At 00:00 UTC and 04:00 UTC, the potential temperature increases with height and thus indicates stability; in particular, the measurements at 04:00 UTC represent a nearly neutrally stratified boundary layer. The potential temperature at 20:00 UTC and 24:00 UTC indicates strong stable stratification. The corresponding wind profiles in Figure 2.2(b) show that shear affects the boundary layer at higher altitudes. Whereas shear is a feature

of the surface layer during daytime hours, during nighttime, shear takes place in the stable nocturnal boundary layer Stull (1988) wherein shear is available at higher altitudes in those hours. At 00:00 UTC, 04:00 UTC, and 20:00 UTC, shear is highest in the lowest 200 m agl to 275 m agl. At 24:00 UTC, the wind profile exhibits especially strong shear reaching heights $\geq$ 500 m agl. Nocturnal low-level jets are able to accelerate the air masses at higher altitudes caused by a strongly stratified boundary layer during nighttime.

According to Kim and Park (2003), within a strongly sheared and convectively-

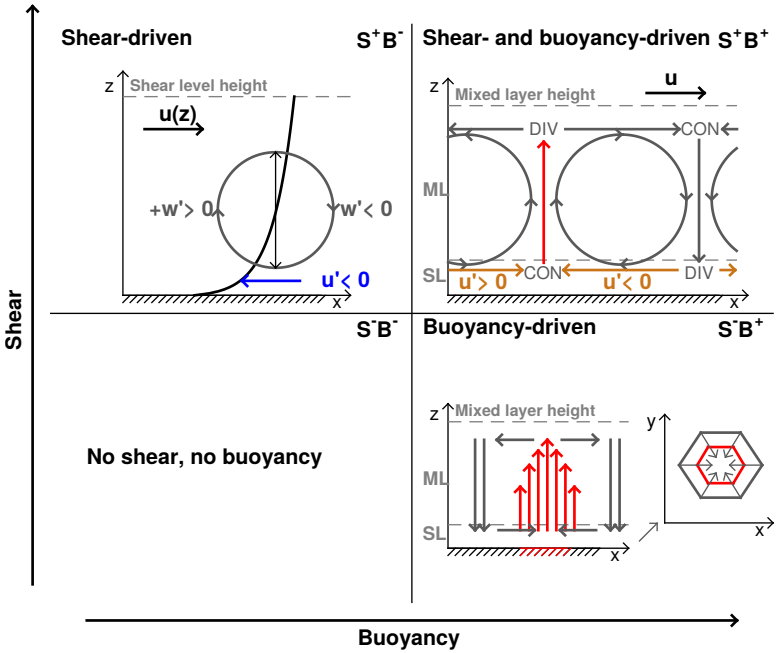

Figure 2.3: Model of shear and buoyancy as coherent structure driving mechanisms. Shear increases from bottom to top and buoyancy from left to right. In S^+B^- the orientation of shear-related eddies in the surface layer is illustrated. S^-B^+ shows the vertical motions related to closed-cell convection and transfers processes to the horizontal x-y-plane. S^+B^+ shows a shear-driven atmosphere dominated by buoyancy and locates related eddies in the boundary layer. S^-B^- represents situation with no shear and buoyancy.

driven boundary layer, low wind speed streaks – as well as high temperature streaks – are induced by momentum and heat transport due to vortical motions. Figure 2.3 illustrates situations leading to vortical motions within the boundary layer, characterized by buoyancy (increasing from left to right) and shear (increasing from bottom to top). The scenario S^-B^- represents a meteorological situation with minor turbulence production by shear (S^-) and buoyancy (B^-). S^-B^--situations have no significant source of turbulence and do not support the development of eddies. Therefore coherent structures do not tend to form.

The scenario S^+B^- is characterized by major shear and minor buoyancy. As shown in Figure 2.2, shear affects height levels differently throughout the day. However, Young et al. (2002) presented two processes explaining vortical motions within the mean shear in the surface layer (d and e). Following this theory, existing vortices are oriented as illustrated in Figure 2.3. Corresponding to the motion induced by the vortices, the horizontal wind speed near the ground varies in comparison to the mean wind speed.

Scenario S^-B^+ explains cellular structures in situations where buoyancy results in vortical motions in the absence of shear (Khanna and Brasseur, 1998). Below an updraft region and above a downdraft region, areas of converging wind speeds are prevalent. In the opposite, above updraft regions as well as below downdraft regions areas of diverging wind speeds can be observed. Feingold et al. (2010) used LES to analyse cellular patterns and state two different situations: open-cell and closed-cell convection. Figure 2.3 clearly illustrates vertical and horizontal movements regarding updraft motions and the processes related to closed-cell structures. Currently, only a few studies deal with these cellular structures and they have not yet been observed in measurement data.

The last scenario describes a situation with both buoyant and shear turbulence production (S^+B^+). An upward directed surface heat flux causes thermals to rise and results in convective mixing. As in the previous example, horizontal air movements compensate for the vertical movements and result in areas of divergence and convergence. The compensating movements cause regions of with $u' > 0\,\mathrm{m\,s^{-1}}$ and $u' < 0\,\mathrm{m\,s^{-1}}$ compared to the mean wind. The buoyancy-driven

air movements can be illustrated by vortices with a range comparable to the size of the thermals responsible for the vertical motions. Thermals are able to reach up to the mixed layer height where a temperature inversion restraints any vertical movements. This scenario describes a superstition of two driving mechanisms. During S^+B^+-situation, coherent structures show a huge ambiguity of appearances. With dominant shear-driving, the coherent structures are organizes as streaks orientated in mean wind direction. With dominant buoyantly-driven turbulence the structures are driven by thermals and exhibit an appearance comparable to cellular structures. In Chapter 4, the manual characterization results
This conceptual model is based on considerations regarding possible triggering mechanisms. Many studies (Moeng and Sullivan, 1994; Young et al., 2002; Kim and Park, 2003; Barthlott et al., 2007) point out dependencies to mechanically generated turbulence as well as to buoyancy-induced turbulence. The definition of four regimes – S^-B^-, S^+B^-, S^-B^+, and S^+B^+ – distinguishes between the driving mechanisms under different meteorological conditions.

Coherent Structures in a Horizontal Wind Field Data Set

The previous section introduced a conceptual model of how coherent structures relate to vortices within the boundary layer. This section is concerned with how coherent structures manifest in measurements of the horizontal wind field. Figure 2.4 shows results of horizontal (vertical) cross-sections within an LES model with 96 x 96 x 96 data points and dimensions of $x = 3\,\mathrm{km}$, $y = 3\,\mathrm{km}$, and $z = 1\,\mathrm{km}$. The underlying geostrophic wind is directed from left to right with $15\,\mathrm{m\,s^{-1}}$ and thus represents a wind situation with high shear $u_* = 0.59\,\mathrm{m\,s^{-1}}$. The boundary layer height is $z_i = 498\,\mathrm{m}$. The shadings depict the variation of the wind speed $u' \leq -0.5\,\mathrm{m\,s^{-1}}$ (light) and $u' \geq 0.5\,\mathrm{m\,s^{-1}}$ (dark) in a) and c), respectively the variation of the vertical wind speed $w' \leq -0.3\,\mathrm{m\,s^{-1}}$ (light) and $w' \geq 0.3\,\mathrm{m\,s^{-1}}$ (dark) in b) and d). a) shows a streaky organization pattern orientated in mean wind direction. Low-speed streaks (light shading) alternate with

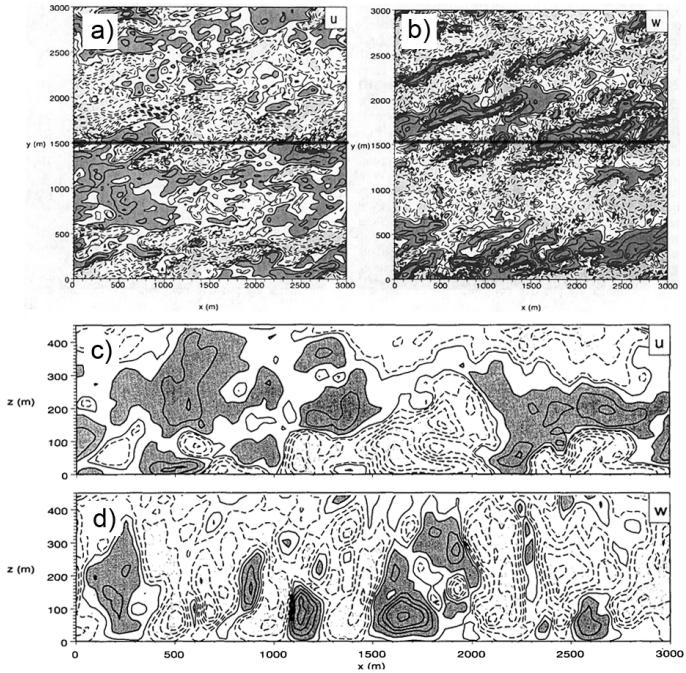

Figure 2.4: Contour of flow variables within LES. (a) x-y plane at $z/z_i = 0.2$, with dark (light) shading representing values of $u' > 0.5\,\mathrm{m\,s^{-1}}$ ($u' < -0.5\,\mathrm{m\,s^{-1}}$), black line indicates location of (c). (b) x-y plane at $z/z_i = 0.2$, dark (light) shading representing values of $w' > 0.3\,\mathrm{m\,s^{-1}}$ ($w' < -0.3\,\mathrm{m\,s^{-1}}$), black line indicates location of (d). (c) x-z plane at $z/z_i = 0.2$, dark (light) shading representing values of $u' > 0.5\,\mathrm{m\,s^{-1}}$ ($u' < -0.5\,\mathrm{m\,s^{-1}}$). (d) x-z plane, dark (light) shading representing values of $w' > 0.3\,\mathrm{m\,s^{-1}}$ ($w' < -0.3\,\mathrm{m\,s^{-1}}$) from Moeng and Sullivan (1994).

high-wind streaks (dark shading). Figure b) exhibits streaky structures and indicates that the vertical wind speed w' is anticorrelated with u', while c) represents u' within a vertical cross section aligned in mean wind direction and implies that the structures extend through the whole boundary layer. The comparison to d) shows that updrafts $w' > 0\,\mathrm{m\,s^{-1}}$ show an anticorrelation with regions of reduced wind speed $u' < 0\,\mathrm{m\,s^{-1}}$ and the other way around. Streaky patterns like these

can be found often (Moeng and Sullivan, 1994; Khanna and Brasseur, 1998; Newsom et al., 2008).

Comparable studies based on simulations and tower measurements regarding coherent structures point out, that the vertical velocity w' is anticorrelated with the wind speed fluctuation in mean wind direction u'. A quadrant analysis leads to a common definition to quantify streaky structures in a x-z-plane according to the ejection- and sweep pattern, where x is orientated in stream-wise direction and z is oriented in vertical direction (Bergström and Högström, 1989; Robinson, 1991; Adrian et al., 2000; Drobinski et al., 2004). The streamwise u' and the vertical w' component of the wind speed are anticorrelated. So-called ejections appear when $u' < 0\,\mathrm{m\,s^{-1}}$ and $w' > 0\,\mathrm{m\,s^{-1}}$. Ejections alternate in spanwise directions with sweeps, which are areas indicating $u' > 0\,\mathrm{m\,s^{-1}}$ and $w' < 0\,\mathrm{m\,s^{-1}}$. Both ejections and sweeps are elongated in the mean wind direction. However, vortices also explain a frequently analysed anticorrelation of the fluctuation of the wind component parallel to the mean wind u' and the fluctuation of the vertical wind speed w' (Robinson, 1991; Adrian, 2007; Stawiarski, 2014).

This chapter has so far explained how coherent structures look like in the atmospheric boundary layer and what processes lead to the formation of coherent structures. The following chapter concerns dual-Doppler measurements to gain a $10\,\mathrm{km^2}$ horizontal wind field data set near the ground with a horizontal resolution of about 60 m and a temporal resolution of 12 s seconds. The question arises as to how the horizontal wind field data set is influenced by coherent structures. As the dual-Doppler method is not able to retrieve the three-dimensional wind component, no information of the vertical wind component is available. The calculation of the fluctuation of the wind speed in the mean wind direction u' provides the basis for all following algorithms.

During atmospheric conditions regarding the scenario of S^-B^- no coherent structures are expected, and therefore the wind field is expected to be homogeneous. Coherent structures manifest in the horizontal wind field as areas of reduced wind speed with $u' < 0\,\mathrm{m\,s^{-1}}$, alternating with areas of enhanced wind speed with $u' > 0\,\mathrm{m\,s^{-1}}$. According to Moeng and Sullivan (1994); Newsom et al.

(2008), coherent structures in situation with S^+B^- and S^+B^+, the areas with $u' < 0\,\mathrm{m\,s^{-1}}$ and $u' > 0\,\mathrm{m\,s^{-1}}$ might appear as streaks. The length of the streaks is expected to range from a few hundred meters to a few kilometers and therefore the dual-Doppler method is feasible to disclose these structures. Under situation with minor shear-driven turbulence and dominant buoyantly generated turbulence (S^-B^+), some studies anticipate cellular structures. In fact, these structures have not yet been measured in wind field data, the following expectations might be speculative (Feingold et al., 2010). As the mean wind in these situation is around $u \approx 0\,\mathrm{m\,s^{-1}}$, the interpretation of both u' and the fluctuation of the cross-wind component v' is important. However, cellular structures are not expected to appear frequently.

3 Probing the Horizontal Wind Field Using Dual-Doppler Lidar

The standard setup for coherent structure measurements in the atmospheric boundary layer is based on tower in-situ instrumentation (Barthlott et al., 2007; Segalini and Alfredsson, 2012; Zeeman et al., 2013). In-situ point measurements can be interpreted as one-dimensional data sets using Taylor's hypothesis of frozen turbulence, and they can reveal information regarding the length and intensity of coherent structures. In the past decade, Doppler lidars have become more and more important for atmospheric investigations of the boundary layer wind field. Because these remote sensing instruments provide long range measurements with a sufficient spatial and temporal resolution, the deployment of Doppler lidars plays a major role in research regarding wind and coherent structures (Newsom et al., 2008; Iwai et al., 2008).

In this work, two Doppler lidars were used in a synchronized scan mode to provide a two-dimensional horizontal wind field data set. The HD(CP)^2 Observation Prototype Experiment (HOPE), which is part of the High Definition Clouds and Precipitation for Advancing Climate Prediction (HD(CP)^2) research project, was conducted from April to May 2013. The Institute of Meteorology and Climate Research (IMK-TRO) deployed a dual-Doppler lidar system within the KITcube mobile observation platform. This chapter explains the measuring principle of Doppler lidars and their synchronized setup during HOPE. Furthermore, this chapter describes the data processing methods applied to the dual-Doppler lidar data set and their application to further meteorological data.

3.1 Doppler Lidar Measurements

A Doppler lidar is a remote sensing instrument based on laser technologies that is capable of measuring wind speed over long distances in the range of up to 12 km. Due to the flexibility of lidar, the technology has been increasingly used in the recent decades for example for measurements of convective roll vortices (Drobinski et al., 1998), nocturnal low-level jets (Banta et al., 2002; Pichugina et al., 2004; Damian et al., 2014), or entrainment processes on the top of the mixed layer (Träumner et al., 2011). The following section describes the measuring principle of pulsed Doppler lidars.

3.1.1 Pulsed Doppler Lidar

The acronym 'lidar' (Light Detection and Ranging) describes a remote sensing method based on laser light. The general principle is comparable to a 'radar' (Radio Detection and Ranging), but uses laser light instead of electromagnetic radiation. To provide a powerful and reliable source of coherent light, the laser is the most important unit within a lidar system.

The Laser Unit

A laser (Light Amplification by Stimulated Emission of Radiation) provides a source of light which is nearly monochromatic, coherent, highly directed, and focused (Halliday et al., 2009). Lasers consist of an active medium, an energy pump, and an optical resonator (Demtröder, 2010). As a result of stimulated emission, a photon with the energy of $h\nu = E_i - E_k$ can force an atom with the energetic state E_i to emit a photon of the same direction, frequency, and phase (Tipler, 2000). When an atom emits a photon, it will change to a less energetic state E_k, whereas an atom which absorbs a photon changes to a higher state E_i. When, for example, a solid state body is stimulated by an energy pump, it emits coherent light. In thermal equilibrium, the energy states $E_k < E_i$ have a popula-

tion $N(E_k) > N(E_i)$. Using an energy pump such as a CW-diode, a population inversion is created with $N(E_k) < N(E_i)$. More photons are emitted by atoms as they are absorbed. The solid state body is positioned in between two resonating mirrors. One is highly reflecting and the other one semi-permeable. At the end of the semi-permeable mirror, the light exits the system. The main lidars (WTX, HYB, see Section 3.2.2) used in this work are equipped with a Tm:LuAG, respectively with an Er:YAG solid state laser. In contrast to a continuous wave laser, where the population inversion is perpetuated constantly, a pulsed laser stops emitting laser light regularly. The different laser pulses are defined by their width and the repetition rate.

Atmospheric measurements using a Doppler lidar

Similar to a radar, a lidar emits radiation into the atmosphere and gains information by analysing the backscatter signal. A radar uses electromagnetic radiation to measure the speed of objects with sizes comparable to droplets. It can be used for rain and cloud measurements. The laser light emitted by lidars has a much smaller wavelength and thus lidars are able to resolve comparably small particles like dust and aerosol. Due to the particle movement, the backscatter signal is affected by the Doppler effect which leads to a shift in frequency. This allows for retrievement of the velocity of particle movement in the beam line direction. Assuming that the dust particles are moving with the wind, a Doppler lidar is able to measure the one-dimensional radial velocity in the beam line direction. Using a pulsed Doppler lidar, the time differences between emission and detection lead to the measuring position along the beam line. The total frequency shift Δf is defined by:

$$\Delta f = -f_o \cdot 2\frac{v_r}{c}\,, \tag{3.1}$$

where f_0 is the frequency of the outgoing laser light, v_r is the radial velocity, and $c = 2.998 \cdot 10^8\,\mathrm{m\,s^{-1}}$ is the speed of light (Meschede, 2010). An aerosol particle moving towards the lidar leads to a negative radial velocity. Doppler lidars usu-

ally use frequencies f_0 in the infrared.

Lidar Design

All lidars used in this work are Doppler lidars. A Doppler lidars' receiver unit typically utilizes a telescope, which both sends out the light into the atmosphere and also detects the backscatter signal (Wulfmeyer et al., 2003). The setup of a receiver is shown in Figure 3.1. Through both telescopes (primary and secondary) the laser light routes from the transmitter unit into the atmosphere and from the atmosphere back to the detection unit. Grund et al. (2001) mentioned that it is not necessary to separate the two signals, since the separation is held out by a polarization beam splitter through which only polarized light is able to pass. Therefore the 1/4 waveplate is essential to polarize the outgoing laser signal. The local oscillator mixes the backscatter signal with a reference signal. This method is often referred to as heterodyne detection (Fried, 1967). On the top of the lidar, a scanning unit points the laser signal into the atmosphere. The lidars used in this work are able to cover the upper half hemisphere.

3.1.2 Signal Processing

The signal processing is held out by the lidar system itself. The radial velocity v_r and the Signal to Noise Ratio (SNR) are quantities relevant to this work. The first one describes the particle movement in the beam line direction. The second one is a measure to quantify the quality of the signal. Both values are retrieved from the frequency spectrum of the measured signal.
Using one light pulse leads to up to $2 \cdot 10^4$ single measures along the beam line, which have a spatial resolution ranging from about 0.3 m to 1.0 m. Averaging over 100 samples per gate assures a sufficient data quality and results in a spatial resolution of $\Delta p \approx 60$ m. These averaging intervals Δp are defined as range gates. This thesis uses an algorithm developed by Stawiarski et al. (2013) that balances the horizontal and the temporal resolution in dependence to the wind speed. For

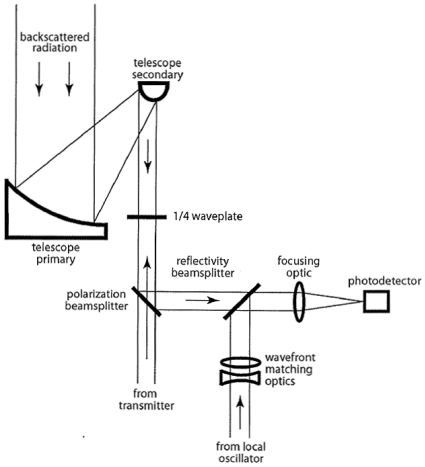

Figure 3.1: Schematic of a lidars' receiver, (Wulfmeyer et al., 2003)

that reason the length of a range gate varies between 60 m and 78 m (see Section 3.2.3). A temporal average over a certain amount of samples improves the quality and reliability of the data. The first lidar (HYB) analyzes 500 pulses per second and averages over 50 data points; the second one (WTX) measures 750 pulses per second and averages over 75 data points. This results in a temporal resolution of 10 Hz for both WindTracer systems. A system-internal Fast Fourier Transformation (FFT) converts the signal into the frequency domain. The location of the maximum of the FFT signal represents the radial velocity, whereas the SNR is determined by the ratio between the values surrounding the maximum in a 6 MHz frequency band (signal values) compared to the rest of the signal (noise values). SNR values are highly specific to each system. Maurer et al. (2015) published a set of reasonable SNR values for the lidar systems deployed during the HOPE field campaign. Regarding the WindTracer systems, SNR values ≥ -4 are referring to good data quality, whereas values < -4 indicate an insufficient data quality.

3.1.3 General Lidar Scan Modes

Many lidars use scanner devices to direct the laser light to the demanded point in space. A scanner enables the use of three basic scan modes. When the scanner points statically into one direction, the scan mode is often referred to as 'static measurements'. This method is often used for measuring the vertical wind speed where the lidar is pointing in upward direction at all times. When wind information at different points is demanded, the lidar can be deployed in a so-called 'stop-and-stare' or 'step-and-stare' mode. Here, the lidar points into one direction before the scanner moves to another destination and again stares. Many lidars are able to measure continuously while the scanner is moving. The Range Height Indicator (RHI) describes a scan mode where the azimuth angle is constant while the elevation angle varies between 0° to 180°; thus the lidar measures the radial velocity within an x-z-plane in the upper half hemisphere. Scan patterns like these allow for the interpretation of the vertical extent and structure of the boundary layer. In contrast to RHI scans the Plan Position Indicator (PPI) describes a scan mode where the azimuth angle varies at a constant elevation angle. Measurements like these lead to radial velocity information within a circular domain. The horizontal structure of the atmospheric boundary layer can be analyzed using the PPI method. The Velocity Azimuth Display (VAD)-Algorithm (Browning and Wexler, 1968) uses the information of a combination of RHI and PPI scans to estimate the vertical profile of horizontal wind speed above the lidar.

3.1.4 Dual- and Triple-Doppler Scan Applications

One lidar is able to resolve the one-dimensional projection of the three-dimensional wind vector along the beam line. Measurements of the vertical wind speed can be conducted with one single Doppler lidar. The retrieval of the horizontal wind vector demands the information of two independent radial velocities and therefore the application of two Doppler lidars. Recently, numerous studies have dealt with dual-Doppler measurements. Wind measurements along virtual towers allow interpretation of the wind profile over arbitrarily chosen terrain and thus

yield information at points that are not accessible with in-situ measurement methods. Calhoun et al. (2006) used two Doppler lidars in the „Joint Urban 2003“ experiment in Oklahoma City to determine the wind flow in street canyons. Damian et al. (2014) measured the vertical profile of the horizontal wind vector at heights up to 1.5 km agl and analysed a nocturnal low-level jet evolution in the Rhine Valley in Germany. Röhner and Träumner (2013) deployed two lidars in a so-called co-linear mode and measured the vertical wind component as well as one horizontal wind component along two intersecting tilted virtual towers. Using this pattern, they were able to conduct turbulent measurements and estimate turbulent measures such as the TKE. Iwai et al. (2008) applied two Doppler lidars at an airport in Japan to retrieve the horizontal wind vector within a horizontal plane, as well as the vertical wind vector within an x-z-plane. Newsom et al. (2005) retrieved the horizontal wind field by conducting planar scans, which was also a part of the „Joint Urban 2003“ experiment. Mann et al. (2008) even use triple-Doppler measurements for comparisons to measurements conducted by a sonic anemometer, thus showing the general applicability of triple-Doppler methods. Choukulkar et al. (2012) demonstrated the feasibility of a single-Doppler vector retrieval based on optimal interpolation techniques. This offers the possibility of retrieving the horizontal wind vector from single-Doppler measurements.

3.2 KITcube Measurments During HOPE

The IMK-TRO at the Karlsruhe Institute of Technology (KIT) deploys an advanced mobile integrated observation system, the KITcube[1] (Kalthoff et al., 2013). This system provides temporally and spatially highly resolved measurements within a volume of 10 km x 10 km x 10 km, and it combines the advantages of in-situ and remote sensing instruments. KITcube can be flexibly deployed within field campaigns and resolves many relevant processes within the atmospheric boundary layer. Detailed process studies help to gain knowledge of underlying atmospheric processes and thus help to improve model-based predic-

[1] http://www.imk-tro.kit.edu/english/4635.php

tions. The KITcube can be used flexibly for many purposes, such as atmospheric monitoring over long periods of time and field campaigns at sites all over the world. Since 2010, the KITcube system has played a major role in many campaigns – the HyMeX[2] campaign in the Mediterranean in 2012, the HOPE[3] field campaign in Germany (2013), and the DESERVE[4] research project at the Dead Sea in Israel and Jordan in 2014. In 2016, the KITcube will be deployed in West Africa in the framework of the DACCIWA[5] research project.

3.2.1 HOPE Field Campaign

The HOPE field campaign took place in April and May 2013 in Jülich, Germany. These measurements are part of the HD(CP)^2 research project where several international and German institutes contributed. HD(CP)^2 aims to improve the accuracy of the prediction of clouds and precipitation by the identification of processes which influence the quality of the simulations. The HOPE field campaign provides highly resolved measurement data, which will be compared to simulation data referring to the same domain in further studies within HD(CP)^2. Figure 3.2 shows the location of the measurements taken during the HOPE field campaign. The IMK-TRO administrated the KITcube-sites (a) and (b), where all instruments within the KITcube monitoring systems are deployed. The TERENO-site[6] is deployed by the IMK-IFU[7] and the Forschungszentrum Jülich[8]. Participating in this field campaign offered a great opportunity to study the existence and characteristics of coherent structures in the atmospheric boundary layer. The results of these dual-Doppler lidar measurements have already contributed to publications regarding HOPE measurements (Eder et al., 2015; Träumner et al., 2015). Figure 3.2 gives an overview of the measurement site.

[2] http://www.imk-tro.kit.edu/english/2571_4553.php
[3] http://hdcp2.zmaw.de/
[4] https://www.imk-tro.kit.edu/english/4520_5535.php
[5] http://www.imk-tro.kit.edu/english/2571_6135.php
[6] http://teodoor.icg.kfa-juelich.de/overview-en?set_language=en
[7] http://www.imk-ifu.kit.edu/
[8] http://www.fz-juelich.de/portal/DE/Home/home_node.html

The area is located in between two open pit mines, one near Inden (i) in the West and the other near Hambach (ii) in the East. Both pit mines are several hundred meters deep and act as inhomogeneities within the domain. In the north of Hambach (ii), there is also an artificial dump hill with forest cover. The lidar measurements took place within a primarily flat terrain where many different farmlands are located (Maurer et al., 2015). In between the farmlands, the area also includes smaller villages and buildings (iii), power poles (iv), and trees.
Table 3.1 lists the instruments' locations during HOPE. Near the Hambach

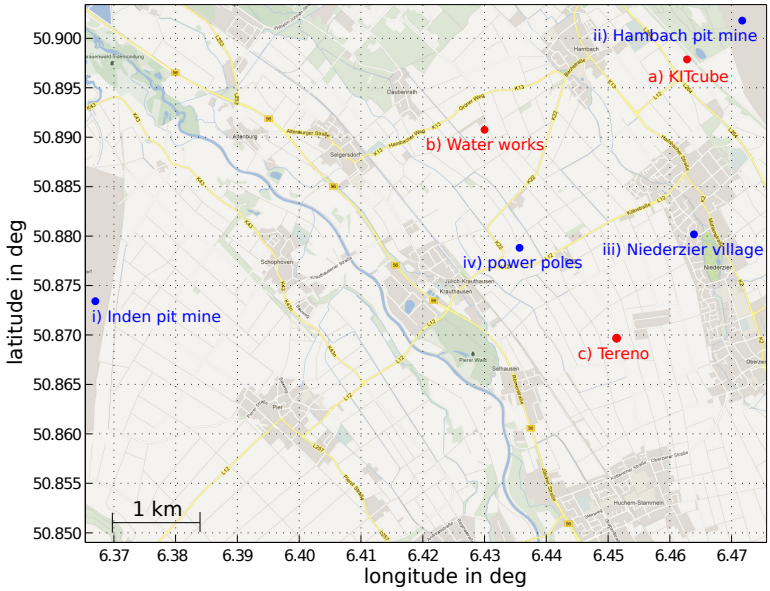

Figure 3.2: Instruments locations during HOPE. At (a) the KITcube is positioned including the WTX Doppler lidar, the Eddy-Covariance-Station 1 and the HATPRO radiometer. (b) marks the HYB Doppler lidar, the WLS200 Doppler lidar and the Eddy-Covariance-Station 2. At (c) the HALO Doppler lidar and the Eddy-Covariance-Station 3 are located. i) and ii) are marking open coal pit mines, at iii) and iv) higher buildings are located and thus act as obstacles for lidar instruments. (Source of picture: http://maps.google.com)

Table 3.1: Instrument locations and metering frequency during the HOPE field campaign.

	lat [deg]	lon [deg]	alt [m asl]	freq. [Hz]
WTX	6.4640	50.8971	113	10
ECS 1	6.4638	50.8972	113	20
HATPRO	6.4637	50.8974	113	10
30m-Tower	6.4638	50.8972	113	20
HYB	6.4299	50.8914	97	10
WLS200	6.4298	50.8913	97	1
ECS 2	6.4297	50.8913	97	20
HALO	6.4514	50.8697	106	1
ECS 3	6.4513	50.8695	106	20

site (a), the KITcube recorded data of one Doppler lidar (WTX), one Eddy-Covariance-Station (ECS 1), a microwave radiometer HATPRO, and a 30 m-meteorological-tower are used in this work. The second site near water works (b) is connected to the KITcube using long-range WiFi-antennas. At this site, two Doppler lidars (HYB, WLS200) and another Eddy-Covariance-Station (ECS 2) are deployed. The WTX and the HYB lidar are operated as a dual-Doppler system. The WLS200 measured PPI and RHI scans from 4 April to 27 April, 2013. At the TERENO site (c), another Doppler lidar (HALO) performed either vertical scans or RHI scans pointing into the dual-Doppler domain (region of interest). Furthermore, a third Eddy-Covariance-Station (ECS 3) provides turbulent fluxes.

Table 3.2: Specifications of lidar instruments deployed during HOPE field campaign.

Lidar system	HYB	WTX	WLS200	HALO
type of laser	Tm:LuAG	ER:YAG	nA[9]	nA
wave length	2023 nm	1617 nm	1543 nm	nA
pulse length	370 ns	300 ns	200 ns	nA
pulse energy	2.0 mJ	2.7 mJ	nA	nA
repetition freq.	500 Hz	750 Hz	nA	nA
sampling rate	250 MHz	250 MHz	nA	nA

3.2.2 Doppler Lidar Measurements During HOPE

The Windtracer Systems

The dual-Doppler lidar system used in this work consists of two WindTracer lidar systems produced by Lockheed Martin (Louisville, Colorado, USA). The IMKTRO implemented both lidars in the KITcube monitoring system. Both system are similar, although they have some technical differences. The older lidars' (HYB) laser works at a wavelength of 2.023 μm, while the newer one (WTX) uses a laser wavelength of 1.617 μm. Additional technical details can be found in Table 3.2. Both systems use a scanning unit which can point at every point in the upper half hemisphere. Both scanners are able to move very quickly, up to 20° per second. This thesis is based on data using a much slower scanning speed of about 6° per second depending on the background wind speed (see Section 3.2.3). The HYB as well as the WTX are installed to containers built on swap bodies for an easy transportation.

3.2.3 Development of dual-Doppler Scan Algorithm

Section 3.1.4 introduced several dual-Doppler applications. Within the scope of this work, both lidars performed a synchronized dual-Doppler scan pattern.

Therefore both lidars perform overlapping 90°-sector scans. Within the overlap, the dual-Doppler retrieval (see Section 3.2.4) allows observers to retrieve the horizontal wind vector.

Synchronisation

The application of dual-Doppler presumes a sufficient temporal synchronization. Many lidar systems are operated using a Graphical User Interface (GUI) provided by the manufacturer. Once the software is started, it finishes the tasks step by step. It is generally difficult to achieve a sufficient temporal synchronization for dual-Doppler purposes using independent GUI applications.
The KITcube dual-Doppler system is controlled by software developed by Stawiarski (2014). A Remote Operating Station (ROS) communicates with both lidars, receiving status updates every second, and managing all tasks for the lidars. The software is based on a C++-library provided by the manufacturer. Settings like range gate length, repetition frequency, and scanner movements can be controlled using control scripts. For dual-Doppler applications, it is highly advisable to implement waiting intervals, so both lidars start one measurement cycle simultaneously. Actual measurements like wind speed can be used in the software, so that the control script can be automatically adjusted to the meteorological conditions. Operational scan patterns can easily be included in all scan patterns. Every hour a combination of RHI and PPI scans was executed to calculate the vertical profile of horizontal wind speed using the previously mentioned VAD-algorithm.

Planar Scans

Figure 3.3 gives an overview over how the lidars measurements are located in the measuring domain. The markers A1 and A2 indicate the position of the WTX- and the HYB-lidars. The lidars are placed at a distance of 2.47 km. The red circles with a radius of 350 m mark the areas where measurements are not available. The gray- bordered sectors indicate 90°-sector scans of each lidar. The WTX scans were performed between the azimuth angles $155° \leq \alpha_{\mathrm{WTX}} \leq 245°$ and the

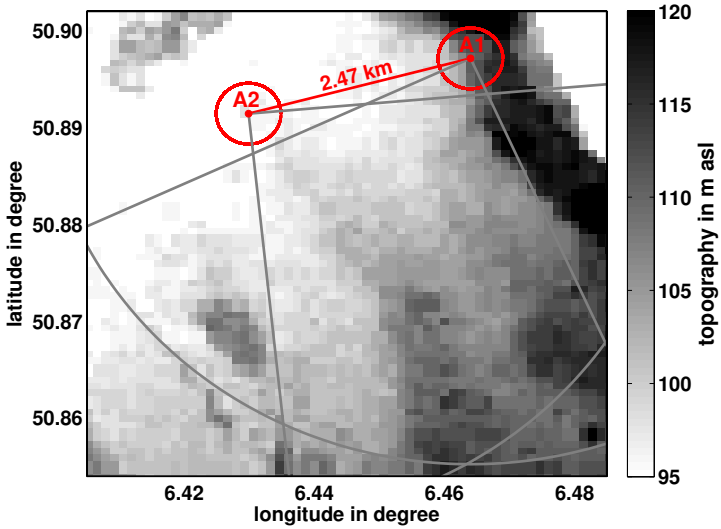

Figure 3.3: Locations of the lidar systems WTX (point A1) and HYB (point A2) in the measurement domain. Gray lines mark each lidars' 90°-sector scan. Within the red circles the lidars do not provide measurement data. The gray-scale colors show the topography in the domain.

HYB scans between $84° \leq \alpha_{\text{HYB}} \leq 174°$. The measurement range of the scans is 4.65 km and the overlap thus represents an area of about 12 km^2. The topography rises in the south-easterly direction. A nearby open pit mine in the north-easterly part is responsible for some inhomogeneities. The terrain first rises to higher values of about 120 m asl and then rapidly falls to -250 m asl. The dig mine itself does not affect the lidar's measurements technically, but the accumulation on which the WTX is placed does. lidar measurements require an undisturbed line of sight within the measuring domain. Due to obstacles in the beam line and the inhomogeneity of the terrain, the lidars are not able to perform a horizontal sector scan.

Height Optimization

Using a small elevation angle φ generally results in higher data availability by avoiding any hard targets that are in the beam line. Simultaneously, though, the vertical wind component contributes to the radial velocity when using an elevation angle. Using a constant elevation angle varying the azimuth results for PPI measurements. The measurement data of PPI scans are aligned at the wall of a concave cone with the lidar in its center. A dual-Doppler lidar setup provides measurements at neighbouring cones. The data locations intersect in two lines; at all other points the measurements are not conducted at the same measurement height. Therefore, the usage of a constant elevation angle might yield measurements with high differences in measuring height. The development of a scanning algorithm using varying elevation angles significantly reduced the height differences between both lidars' measurements and also minimizes the mean measuring height of both lidar data sets.

Figure 3.4 introduces the application of the height optimization algorithm. Figure 3.4(a) is similar to Figure 3.3. The red line between the points A1 and A2 indicates the connection line of both Lidars, 2 km further south of the red line the blue line shows the location of the *x*-*z*-cross-section illustrated in Figure 3.4(b). This graphic visualizes the height differences above the blue line, which is in the middle of the measurement domain. The background layer consists of the lidars positioned at points A1 and A2 regarding the topography (brown curve). The foreground layer contains the gray and black solid lines, representing the measurement heights of both lidars above the blue lines. Whereas the gray lines indicate the heights under the application of a constant elevation angle of $\varphi = 2°$, the black lines represent the measurement heights when a variable elevation angle between $0.25° \leq \varphi \leq 2.25°$ is used. The thin red lines depict the lidar beams while scanning.

Applying the constant elevation angle, the mean measuring height is at values around 100 m agl and the maximum difference between both measurement planes is 60 m. Using a variable elevation angle leads to significant improvements re-

garding the measuring height and height differences between both instruments. When the WTX is pointing westwards ($\alpha_{\mathrm{WTX},0} = 245°$) and the HYB ($\alpha_{\mathrm{HYB},0} = 84°$) is pointing eastwards, the corresponding elevation angle is $\varphi_0 = 0.25°$. The elevation angle increases linearly to values of $\varphi_n = 2.25°$, while the scanner moves to the destination azimuth angles ($\alpha_{\mathrm{WTX},n} = 155°$, $\alpha_{\mathrm{HYB},n} = 174°$). As Figure 3.4(b) indicates, that using a linearly varying elevation angle does not affect the time needed to complete one sector scan but reduces the mean measuring height to approximately 50 m agl and the height differences of both planes to 45 m. Figure 3.4(c) depicts the plane height differences within the whole domain. Maximum values of ≈ 80 m are located in the northwesterly part of the

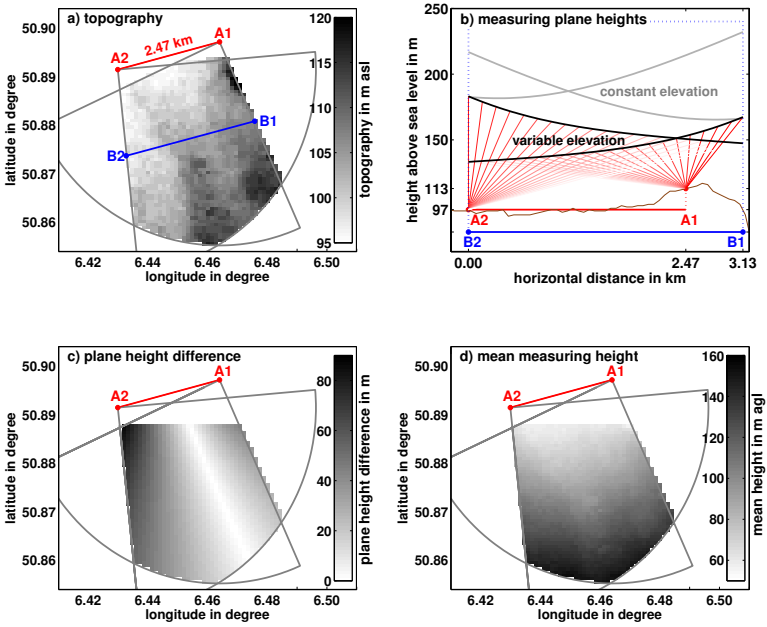

Figure 3.4: Schematic of the height optimization. (a) indicates the measurement domain and the underlying topography, (b) shows the vertical position of both lidars' measurements (description in text), (c) points out the height differences between both lidars' measurements, and (d) shows the mean measurement height in the domain.

domain, where the corresponding elevation angles differ the most. Along a line nearly perpendicular to the connection line, both lidars conduct measurements at same heights. Figure 3.4(d) specifies the horizontal distribution of the mean measuring height relative to the topography. Close to the red connection line, the mean measuring height exhibits minimum values of 55 m agl. In the southerly part, the mean measuring height is at values of 155 m agl. The differences in height increase linearly from north to south. This illustrates that using the varying elevation angles leads to measurements within a tilted plane. The tilt of this particular plane is exactly $\varphi_{\text{tilt}} = 2^{\circ}$. Since the measurements are not conducted at a constant height, wind shear does affect the measurements. A method that accounts for this is introduced in Section 3.2.4.

Range-Time Optimization

The study conducted by Stawiarski et al. (2013) introduced an optimization method that balances the temporal and spatial resolution resulting in an optimal temporal resolution Δt_{opt} and an optimal spatial resolution Δp_{opt}. In general, turbulence elements are advected with the mean wind speed, just as Taylor's hypothesis of frozen turbulence suggests. The length scale that characterizes the measurements regarding the wind speed and the temporal resolution is defined by the distance $\lambda = \Delta t \cdot \overline{u}$. The whole wind field is advected within a time period Δt, and the mean wind speed $\overline{u}$. At higher wind speeds the length scale λ is larger than the horizontal resolution Δp and thus cannot be dissolved. Resolving long turbulence elements requires a reduction of the temporal resolution and thus faster scanning. But higher scanning speeds affect the data density and lessens the data quality. Therefore Stawiarski et al. (2013) defined a second condition to ascertain a sufficient data density. Equation 3.4 defines conditions for Δp_{opt} and

Δt_{opt} and accounts for both a suitable temporal as well as a suitable horizontal resolution:

$$\begin{aligned} \text{if } \sqrt{\overline{u}C_s} \geq \Delta p_{\text{min}} : &\Delta p_{\text{opt}} = \sqrt{\overline{u}C_s} \\ &\Delta t_{\text{opt}} = \sqrt{C_s/\overline{u}} \\ \text{if } \sqrt{\overline{u}C_s} < \Delta p_{\text{min}} : &\Delta p_{\text{opt}} = \Delta p_{\text{min}} \\ &\Delta t_{\text{opt}} = C_s/\Delta p_{\text{min}} \end{aligned} \tag{3.2}$$

$C_s = \frac{2\pi\beta d}{f360^\circ}$ is a factor dependent on the measurement frequency f, the angular range of the sector scans β and the maximum distance to the lidar d.
A VAD-algorithm (see Section 3.1.3) calculates the horizontal wind speed and uses a feedback loop to the scan synchronization software at the ROS to adjust the values for Δp_{opt} and Δt_{opt}. For that reason the range gates Δp are not constant within the whole data set and vary in the range of $\Delta p_{\text{min}} = 60\,\text{m}$ and $\Delta p_{\text{max}} = 78\,\text{m}$. The temporal resolution also varies between $\Delta t_{\text{min}} = 12\,\text{s}$ and $\Delta t_{\text{max}} = 14\,\text{s}$.

3.2.4 Data Processing Methods

Both lidars measured the radial velocity in beam line directions on planes as mentioned in Section 3.2.3. The following section introduces the data processing applied to the data set.

Dual-Doppler Retrieval

Within the overlap area of a dual-Doppler scan, two independent wind components are available; therefore, the horizontal wind vector is retrievable. Stawiarski (2014) applied a retrieval algorithm developed by Newsom et al. (2005). This algorithm calculates the projection of the wind vector in the two-dimensional Lidar plane. The method developed by Stawiarski (2014) filters the data set considering both the SNR (see Section 3.1.1) and a velocity jump filter that eliminates any outliers found in the time series. Applying a Cartesian grid within

the measurement domain allows researchers to address the projection values to corresponding longitude and latitude values. The spatial grid results from the temporal resolution of the measurements and the demanded time for each scan cycle Δt. The spatial resolution of the Cartesian grid Δxy equals to the range gate length Δp. Each grid point is associated with radial velocities of both lidars within a circular cell with the radius $R = \Delta xy/\sqrt{2}$ around the center of the cell r_0. Minimizing the cost function

$$J = \sum_n g_n (r_{v,n} - u_h(r_o) \cdot \hat{r})_n)^2 \,, \tag{3.3}$$

then estimates the most probable horizontal wind vector u_h from all radial velocities $r_{v,n}$ associated with their beam direction vectors $\hat{r}_n$. The factor g_n describes a weighting function developed by Stawiarski (2014). Values close to the center of a cell are of greater importance than values near the edges of a cell. The retrieval algorithm of Newsom et al. (2005) works with a grid spacing of $\Delta xy = 100\,\mathrm{m}$ and a temporal resolution of $\Delta t = 30\,\mathrm{s}$. The three-dimensional retrieval of Iwai et al. (2008) results in a temporal resolution of 12 min and a grid spacing of $\Delta xy = 100\,\mathrm{m}$.

Data Interpolation and Mask Subtraction

Although lidar measurements were conducted very thoughtfully in an effort to avoid all kinds of measurement errors, difficulties cannot be entirely avoided during field campaigns. Within the domain, many smaller forests or single trees, as well as smaller villages with higher buildings (e.g. churches and power poles) acted as hard targets (see Figure 3.2). Each hard target can cause data gaps within the domain. Automated methods as applied in the process of this thesis fail when gaps are too significant. Therefore a two-dimensional interpolation method based on an average value of all eight neighbors is applied to the data set. A vector mask accounts for unusable data both close to and far away from the Lidars and also accounts for an identical shape for each time step. The vector mask is defined by

the overlap area of both measurements, the maximum lidar measurement range of 4.65 km, and the latitude 50.8875°at the northerly boundary. Any data outside this mask is not considered in this study's analysis. The resulting dual-Doppler area therefore is reduced from $\approx 12\,\mathrm{km}^2$ to $\approx 10\,\mathrm{km}^2$.

Subtraction of Running-Mean

The measurements are located within a tilted plane using an elevation angle of $\varphi_{\mathrm{tilt}} = 2°$. Therefore, the wind shear within the surface layer affects the measurements, especially at night under stable stratification. The calculation of a running mean accounts for spatial inhomogeneities that occur over a long time. So the subtraction of a running mean average eliminates spatial inhomogeneities – e.g. wind shear – quite well. The choice of a useful integration time requires some considerations. The time period needs to be sufficiently long so coherent structures are not extinguished by a subtraction of the running mean. Because coherent structures have a life cycle of several tens of minutes (Young et al., 2002; Träumner et al., 2015), the chosen time period should be significantly longer. Otherwise short term changes in the wind profile need to be considered. Some particular changes to take into account are in the morning hours when the stratification becomes more unstable, or in the evening when the stratification stabilizes; in each of these situations, a subtraction of the running mean can cause negative effects. Therefore the averaging period is considered not to be too long. A two-hour period does not extinguish variabilities caused by coherent structures, and it also reacts to short-term changes in the boundary layer without a huge delay.
Figure 3.5 shows how the subtraction of the running mean affects the data set. Measurements were taken on 17 April 2013 at 22:03 UTC, during nighttime hours, and show considerable wind shear effect. The left area represents the southerly (more elevated) and the right area the northerly (less elevated) parts of the measurement domain. It is significant how the wind profile considerably affects the measurements in Figure 3.5(a). Figure 3.5(b) shows the same data set after the 2h-running-mean was subtracted from each data point.

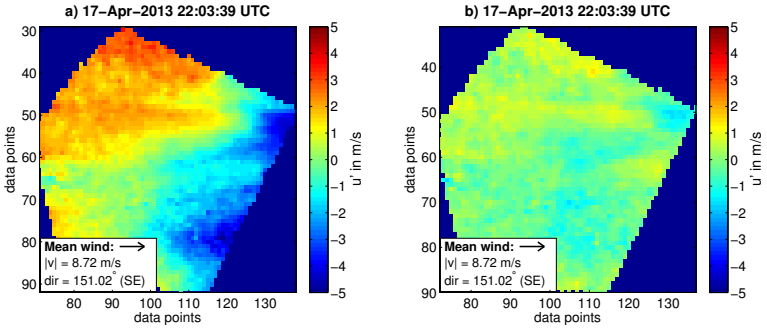

Figure 3.5: Examples for wind situation where no organization is present. (a) wind shear swapping the horizontal wind field, (b) same picture as (a) after subtraction of the two-hour running mean.

3.2.5 Additional KITcube Data

Energy Balance Station

Each Eddy-Covariance-Station measured the meteorological quantities of wind speed and direction, temperature, humidity, air pressure, precipitation, surface radiation temperature, solar and reflected radiance, and long-wave incoming and outgoing radiation (Kalthoff et al., 2013). Measurements are carried out with a 20 Hz temporal resolution and data are integrated over a time period of 10 minutes, excluding the sensible and latent heat flux, which are calculated in 30 minute intervals.

Since the dual-Doppler measurements took place within a 10 km^2 domain, it is useful when using turbulent measurements of many different Eddy-Covariance-Stations. The 20 Hz measurement data are first processed using the software Turbulenzknecht[10]. The quantities of the friction velocity u_* , the horizontal wind components u and v, as well as the sensible heat flux H_0, all show a significant correlation between the mean value and the single stations. For that reason, the average values are used for all purposes in this work. The Monin-Obukhov

[10] provided by UNI Bayreuth: https://epub.uni-bayreuth.de/1051/

length $\frac{z}{L}$ is not well correlated with the corresponding mean values, so for these quantities the ECS1 measurements at the KITcube site are considered.

4 Coherent Structure Classification

Integration of two Doppler lidars into a synchronized scan mode (see Chapter 3) creates a two-dimensional horizontal wind field data set that allows valuable insights into atmospheric boundary layer processes. Section 2.2.3 clarifies the way coherent structures manifest in two-dimensional horizontal wind field data sets. The ejection- and sweep-pattern explains the existence of enclosed regions with reduced and enhanced wind speed compared to the mean flow. Section 4.1.1 presents many examples of horizontal cross sections and reveals a variety of ejection-sweep patterns. This raises the question if there is a way to concentrate the different organization patterns in a remunerative way.
Section 4.1 describes the development of a classification scheme, explains the applicability, and thus helps to generalize the structures measured in the measurement domain. Section 4.2 compares the classified structures with meteorological data sets and introduces dependencies on important boundary layer characteristics. The first part of this section focuses on case studies, while the second part statistically analyses the resulting relations. Section 4.4 concludes the results of this study.

4.1 Description of Methods

Section 2.2.3 applies a model of the atmospheric mechanisms that trigger the formation of coherent structures. Buoyancy and shear are two processes that are proven to have a significant influence on coherent structures. As already discussed, this thesis is based on a two-dimensional horizontal wind field data set and includes the fluctuation of the wind speed u' in mean wind direction. A classification scheme describing the coherent structures as introduced in Figure

2.3 offers the ability to determine under which conditions coherent structures tend to form.

4.1.1 Classification Scheme

Due to the variety of coherent structure showing up in the horizontal wind field, it is inevitable to define classes that account for different appearances. An important requirement for a classification scheme is the general applicability to other data sets, which assures comparability to results in related studies. This part of the study is held out manually and the individual snapshots are evaluated by visual inspection.

As discussed in Section 2.2.3, coherent structures that are dominated by shear exhibit a streak-like appearance. These streaks manifest in enclosed areas of reduced or enhanced wind speed, where $u' > 0\,\mathrm{m\,s^{-1}}$ (ejections) and $u' < 0\,\mathrm{m\,s^{-1}}$ (sweeps). The structures are expected to be aligned in mean wind direction. In situations where buoyancy is clearly subordinate, the horizontal extent of the structures is likely to be in the range of a few hundred meters. In a situation with both buoyancy and shear turbulence production, the horizontal extent of the coherent structures is expected to be considerably larger.

Figure 4.1 exemplarily shows the variety of organizational patterns in the wind field. This figure contains four panels (a) - (d) and every subfigure shows a snapshot taken within one single scan cycle, as mentioned in Section 3.2.3. The pictures are orientated into the mean wind direction, flowing from left to right as indicated by the wind vector. The axis-scaling is a measure of data points, where the x-axis is pointing in the mean wind direction and the y-axis in the cross wind direction. According to the scan-algorithm used, each data point scales differently for most snapshots in the range from 60 m to 75 m. The color-scale indicates the fluctuation of the wind speed in mean wind direction u' in $\mathrm{m\,s^{-1}}$.

Figure 4.1(a) depicts a strong south-westerly wind situation on 10 May 2013, 11:03 UTC, which exhibits clearly defined areas of $u' < 1\,\mathrm{m\,s^{-1}}$ and $u' > 1\,\mathrm{m\,s^{-1}}$ organized in streaks. The alignment of the streaks is mainly in the mean wind

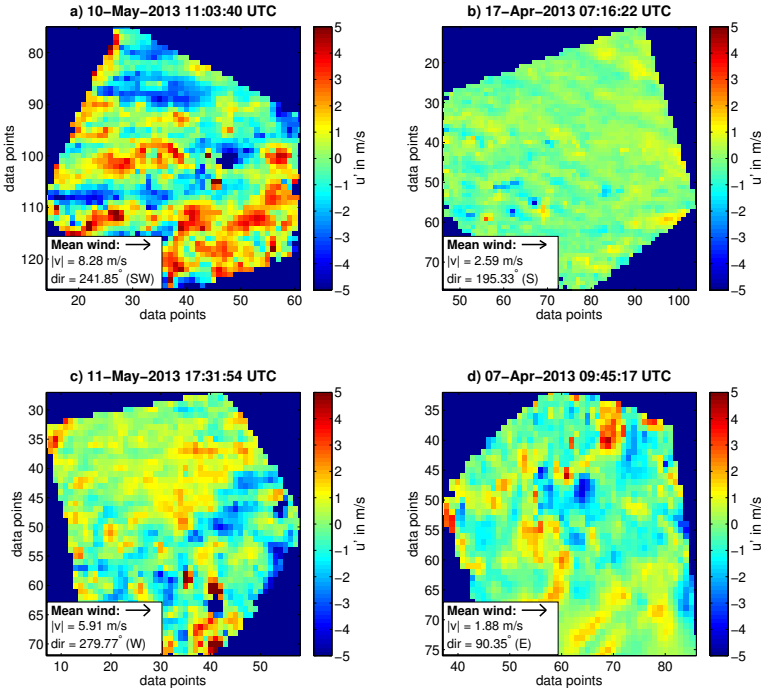

Figure 4.1: Examples for different types of organization patterns. (a) shows a streaky pattern, (b) an organized pattern but no structures with higher intensity, (c) presents a patchy pattern and, (d) a mixture of patches and lines.

direction. The scales of the dominant streaks in this image are in the range $2\,\mathrm{m} \leq l < 4\,\mathrm{km}$. Figure 4.1(b) presents a completely different situation. With medium southerly winds of $2.6\,\mathrm{m\,s^{-1}}$ in the morning of 17 April 2013, 16:22 UTC, the wind field is organized in thin linear structures, with a width of about hundred meters. The intensity of the structures during this time period is weak compared to the previous time period. In Figure 4.1(c) the wind is heading from the west, with wind speeds measuring around $6\,\mathrm{m\,s^{-1}}$. The regions with $u' < -1\,\mathrm{m\,s^{-1}}$ and $u' > 1\,\mathrm{m\,s^{-1}}$ are distinct but somehow patchy and not as streaky as in Figure 4.1(a). The structure length l of the dominant features ranges

from $500\,\mathrm{m} \leq l < 1200\,\mathrm{m}$. Figure 4.1(d) is taken within an easterly low-wind situation and exhibits patches with $u' < -1\,\mathrm{m\,s^{-1}}$, as well as linear structures, with $u' > 1\,\mathrm{m\,s^{-1}}$. The length of scales of the most significant structures ranges from $500\,\mathrm{m} \leq l < 1000\,\mathrm{m}$.

Section 2.2.3 introduced a conceptual model assuming that coherent structures depend on eddies in the boundary layer. Different meteorological conditions create eddies of different sizes. If the size of eddies corresponds to the spatial extent of the coherent structures in the horizontal wind field, the appearances of coherent structures might relate to the prevailing meteorological conditions. Applying a classification scheme to a data set requires the definition of criteria distinguishing different classes of coherent structures.

The amount of fluctuation in wind speed is a measure of the intensities of the structures. The intensity, as the first criterion, helps to decide whether coherent structures are recognizable or not. The second criterion, the structures' extent in the mean wind direction, separates large coherent structures from smaller ones. Using both criteria, the classification scheme is able to separate between A) large coherent structures, B) small coherent structures, C) low-intensity turbulence, and D) no coherent structures. If not specifically mentioned, in this thesis the term "coherent structures" implies regions with $u' < 0\,\mathrm{m\,s^{-1}}$, which is consistent with other studies such as Robinson (1991); Kim and Park (2003); Adrian (2007). Section 2.2.3 also introduced to cellular coherent structures with a hexagonal shape. These structures are not expected to appear frequently and the identification of them is challenging. Therefore, these structures are not included in the classification scheme.

Class A: Large Coherent Structures

One criterion for the characterization of coherent structures is the intensity of the structure. By using the span of the wind speed fluctuation $\max(u') - \min(u')$ and applying a subjectively set threshold, $\Delta u' > \Delta u'_{\mathrm{crit}}$ with $\Delta u'_{\mathrm{crit}} = 2\,\mathrm{m\,s^{-1}}$ accounts for a sufficient intensity for a classification of coherent structures. Based on the

fact that the grid-scaling of the data set is limited to the horizontal measuring resolution of 60 mto 75 m, sub-grid turbulence can not be displayed. By definition, all patterns with $\Delta u' > \Delta u'_{\text{crit}}$ will represent coherent structures. In order to distinguish between large-scale coherent structures and small-scale coherent structures, a second measure is used. Structures with lengths ≥ 1000 m in the direction of their longest extent will be treated as large coherent structures, whereas structures with lengths ≤ 1000 m will be denoted as small coherent structures (B). Figure 4.2 shows four representative examples of large coherent structures. Fig-

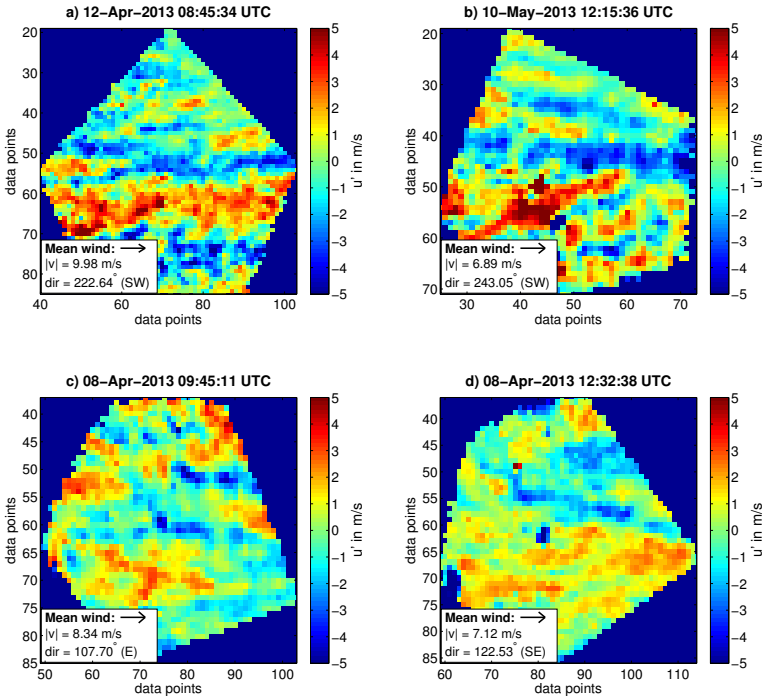

Figure 4.2: Representative Measurements of large coherent structures. (a) and (b) present large-scale streaks under strong wind regimes; (c) and (d) visualize patchy structures.

ures 4.2(a) and (b) show snapshots taken during strong winds in the measurement

domain on 12 April 2013, 08:45 UTC and 10 May 2013, 12:15 UTC. The dominant structures are streaky and orientated parallel to the mean wind direction. The intensity of the structures exceeds values of $\Delta u'_{\mathrm{crit}} = 10\,\mathrm{m\,s^{-1}}$. The largest features even exceed the range of the measuring domain, which in this case is about $l_{\max} \approx 4\,\mathrm{km}$ long. The width of the structures reaches values between about 700 mand 1000 m. Figures 4.2(c) and (d) also represent situations with high background winds. The intensities of these structures – about $\Delta u' \approx 6\,\mathrm{m\,s^{-1}}$ – are not as high as in Figures 4.2(a) and (b). The largest dimensions of the structures are in the range between $1.5\,\mathrm{km} \leq l < 2.0\,\mathrm{km}$ and approximately orientated in the mean wind direction. The width of the structures is around 400 m. In Figure 4.2(d), an area with an enhanced u' is prominent; upon closer examination, this area is subdivided into three thin bands on different length scales. All in all, Figures 4.2(a) and (b) seem to represent clearly defined streaks in contrast to the more patchy organization pattern in Figures 4.2(c) and (d).

Class B: Small Coherent Structures

The intensity of small coherent structures also exceeds $\Delta u' > \Delta u'_{\mathrm{crit}}$, the critical threshold value. Figure 4.3 reveals some impressions of how coherent structures, classified as small, can appear. The snapshot depicted in Figure 4.3(a)

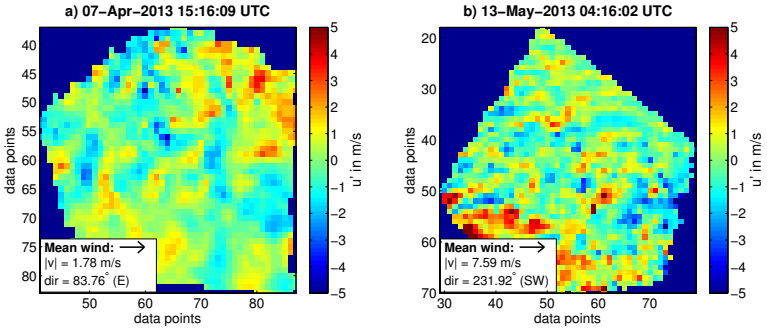

Figure 4.3: Snapshots of wind situations containing small coherent structures. (a) accounts for a less-intense patchy structure pattern; (b) represents a streaky pattern.

shows a structure pattern taken with a corresponding easterly wind speed of $|v| = 1.8\,\mathrm{m\,s^{-1}}$ on 7 April 2013, 15:16 UTC, where the largest structures in the domain exhibit lengths of $l \approx 700\,\mathrm{m}$ and $\Delta w \approx 300\,\mathrm{m}$. The structures are not aligned in a uniform direction and exhibit different shapes, such as patchy patterns or thin lines. Figure 4.3(b) was taken during a strong south-easterly wind situation on 13 May 2013, 04:16 UTC. The dominant length scales are approximately $l \approx 700\,\mathrm{m}$ and $\Delta w \approx 200\,\mathrm{m}$. In contrast to Figure 4.3(a) these structures are orientated parallel to the mean wind direction. This is an example snapshot that contains coherent structures during a nocturnal situation. All previous examples were assembled during daytime. Furthermore, (b) discloses a behavior similar to Figures 4.2(a) and (b) in regards to the streaky organization patterns aligned parallel to the mean wind, although the structures are smaller and less intense here.

Class C: Low-Intensity Organization

Classes A) and B) describe coherent structures with intensities of $\Delta u' > \Delta u'_{\mathrm{crit}}$. $\Delta u'$ often does not fulfil this criterion, but nevertheless the wind field reveals significant organization patterns. In this thesis these cases are summarized as low-intensity organization. Figure 4.4 specifies this kind of organization. Figures

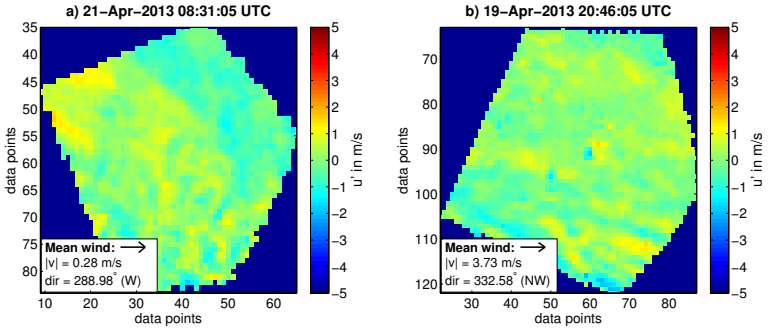

Figure 4.4: Snapshots showing low-intensity organization. (a) represents a calm wind situation and (b) a medium wind situation.

4.4(a) and (b) present situations on 21 April 2013, 08:31 UTC and 19 April 2013, 20:46 UTC, respectively, where all structures are weak in intensity with manifold appearances, i.e. with thread- or spot-patterns. $\Delta u' < 2\,\mathrm{m\,s^{-1}}$ refers to less intense structures, so these structures are not defined as coherent structures. Comparable organization patterns often occur in the early morning hours when turbulence production – and therefore organized structures – occur in the wind field. In between the wind fields some low-intensity structures are revealed. Normally, in the evening, the intensity of coherent structures diminishes and low-intensity structures manifest in the transition to homogeneity. Often in the morning, homogeneous wind fields develop low-intensity turbulence, and then transform to either small or large coherent structures.

Class D: No Coherent Structures

In the description of Class C), the existence of homogeneous wind fields is mentioned frequently. The last class of this classification scheme concentrates on homogeneous events. The presentation of pictures showing uniformity over the whole domain are comparably easy to classify and normally would not attract someone's attention, but in this case the presented snapshots not only point out what homogeneous wind fields look like regarding this thesis. In the lack of any organization they perfectly illustrate some features of the background conditions visible in many scans. In Figure 4.5(a), from 8 April 2013, 22:30 UTC, some shadings are visible in the range of $\Delta u' < 1\,\mathrm{m\,s^{-1}}$, but there seems to be no organization. In the middle of the wind field, some spotted areas occur, particularly one discrete spot with $u' \leq -5\,\mathrm{m\,s^{-1}}$. This can be related to hard target effects of the lidar system, which are visible during many times throughout the whole measuring campaign and have to be ignored. Figure 4.5(b) represents a situation observed on 17 April 2013, 22:03 UTC. As the measurements do not cover a horizontal area but a plane with an elevation of 2°, under stable conditions with an accompanying low boundary layer height, wind shear swaps the measure. Here the reduction of a 2h running-mean, as explained in Section 3.2.4, accounts for

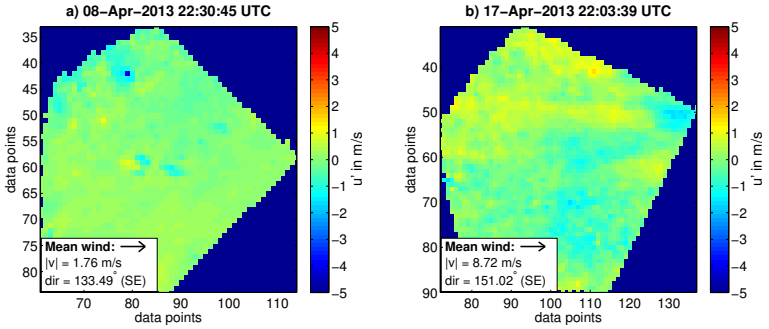

Figure 4.5: Examples for different wind situation where no organization is present. (a) and (b): homogeneous wind fields.

shear affecting the measurements. So while Figure 3.5 is a clear example of a nocturnal situation affected by wind shear, Figure 4.5(b) shows a homogeneous wind field after the subtraction of the 2h running-mean, thus pointing out a situation where neither coherent structure nor low-intensity turbulence is present.

4.1.2 Analyzing Technique

During the HOPE campaign around 90.000 single snapshots were taken for the purpose of this study. As a consequence of time, not every single picture can be analysed on its own. Visualizing all scan results in sequences does not only offer the chance to handle this remarkable data set, it also allows researchers to assess the temporal evolution of coherent structures. Adrian (2007) warns that spatial coherence is not a mandatory criterion for coherent structure existence on its own, but when combined with temporal coherence it is. This study furthermore suggests, that only structures that are significant in sequences should be counted for analysis. The classification scheme is applied to the data set with a temporal resolution of ten minutes, and it does not account for the number of coherent structures in the field. A 10-minute interval with at least one coherent structure that is larger than 1 km over a significant time fulfils all criteria for

an event with large coherent structures. Otherwise, when no coherent structure exceeds the length of 1 km within the 10-minute time interval, this interval is defined as an event with small coherent structures.

A previous subjective analysis on the same data set conducted by four independent observers (Träumner et al., 2015) uses a different classification method with an hourly temporal resolution. A more descriptive approach attempts to categorize the different structures by their appearance. Some examples of structure types used in the study of Träumner et al. (2015) are ”small patchy structures,” ”large-scale structures,” and ”streaky structures.” Since the definitions of these structure types were too specific, a large number of classes were needed to cover the entire wind data set. The characterization scheme used in this thesis was not intended to categorize the structures by their underlying conditions, but only according to the apparent parameters of intensity and scale. A comparison of both classifications is possible by summing up the classes which represent coherent structures. Figure 4.6 shows that most of the events related to coherent structures

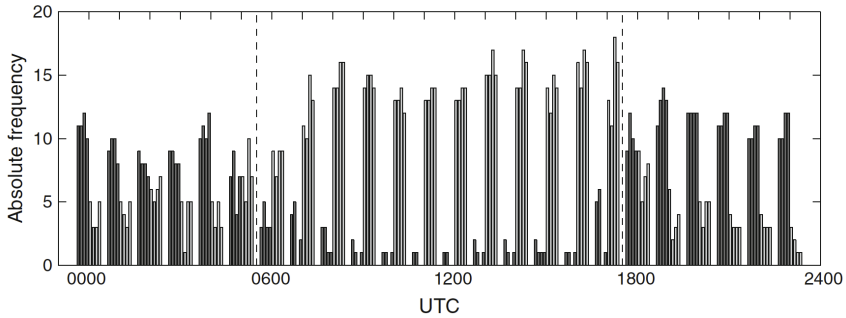

Figure 4.6: Diurnal cycle of frequency regarding wind fields with visually classified coherent structures (light grey) and homogeneous wind fields (dark grey). This figure consideres data from 4 April 2013 to 23 May 2013. Figure from Träumner et al. (2015).

occur during daytime hours (06:00 - 18:00 UTC), whereas homogeneous wind fields are uncommon throughout the day. During the nighttime, homogeneous wind fields dominate while coherent structures play a subordinate role. Using

this information and adjusting the scale to the different temporal resolution allows to compare to Figure 4.7, which is based on the exact same data set as Figure 4.6 but uses a different approach. Both results of Figure 4.6 and Figure

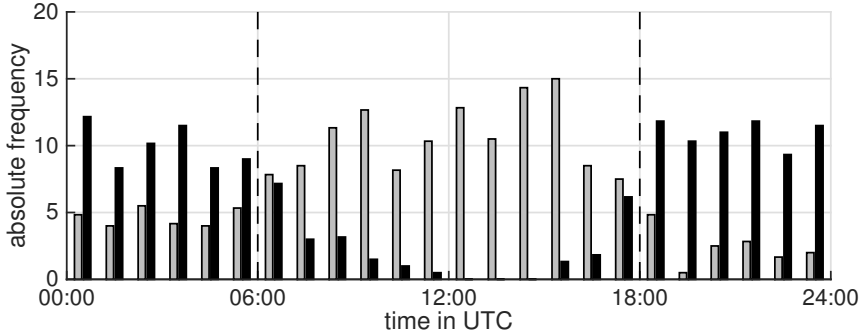

Figure 4.7: Diurnal cycle of frequency regarding wind fields with visually classified coherent structures (light grey) and homogeneous wind fields (dark grey). This figure consideres data from 4 April 2013 to 23 May 2013.

4.7 generally show accordance. During daytime, most of the coherent structures occur and homogeneous wind fields are very rarely present. During nighttime some differences are noticeable. In particular, this study denotes a greater number of homogenous events in the late afternoon around 17:00 UTC to 18:00 UTC compared to the study of Träumner et al. (2015). The low-intensity organization patterns observed in the morning and evening hours might especially be interpreted in a different way. However, in the end, both classification schemes seem to perform similarly.

4.2 Meteorological Evaluation

The following section raises the question of whether turbulent measurements from high frequency energy balance stations can be qualitatively correlated with the development of coherent structures in the atmospheric boundary layer. The first part concentrates on exemplary case studies within different meteorological

situations. The second part analyses the classification statistically in order to find a more general relation between coherent structures and atmospheric parameters.

4.2.1 Case Studies

Within the case studies, the classification data set will be compared to four different quantities. The wind speed $\mathbf{v}_h$ and the friction velocity u_* indicates the force induced by the friction of the earth's surface and therefore represents the shear of the surface layer. The sensible heat flux H_0 refers to buoyancy and the Monin-Obukhov-length $\frac{z}{L}$ is a commonly used measure to analyse the stability of the boundary layer.
Figures 4.8 - 4.10 show data recorded on 1 May 2013, 19 April 2013, and 7 April 2013. At the bottom line of each panel, colored stars represent whether large structures (green), small structures (red), low-intensity organization (blue), and homogeneous wind fields (black) occurred.

The Diurnal Development of Coherent Structures

Figure 4.8 shows measurements under moderate wind conditions with $1\,\mathrm{m\,s^{-1}} \leq \mathbf{v}_h \leq 5\,\mathrm{m\,s^{-1}}$. The application of the classification reveals that the first hours of the day between 00:00 UTC and 3:30 UTC are homogeneous. Within this time frame, the friction velocity is at a level of $u_* = 0.1\,\mathrm{m\,s^{-1}}$. The corresponding sensible heat flux H_0 depicts slightly negative values from $-20\,\mathrm{W\,m^{-2}}$ to $0\,\mathrm{W\,m^{-2}}$ and denotes a stable stratification. The Monin-Obukhov-length is in a positive range between $0 \leq \frac{z}{L} \leq 0.2$. In the early morning, from 03:40 UTC to 05:40 UTC, the friction velocity increases up to values from $u_* = 0.16\,\mathrm{m\,s^{-1}}$ to $u_* = 0.32\,\mathrm{m\,s^{-1}}$ and the wind speed rises to $\mathbf{v}_h \approx 3.5\,\mathrm{m\,s^{-1}}$. From there on, low-intensity structures appear. The corresponding sensible heat flux still represents the stable stratification with values between $-20\,\mathrm{W\,m^{-2}} \leq H_0 \leq 10\,\mathrm{W\,m^{-2}}$, but continuously rises from sunrise on at 04:08 UTC. Responding to the increase of u_* and H_0, respectively (Equation 2.1), the Monin-Obukhov-length $\frac{z}{L}$ exhibits negative values around 05:00 UTC. Between 05:50 UTC and 08:10 UTC the wind

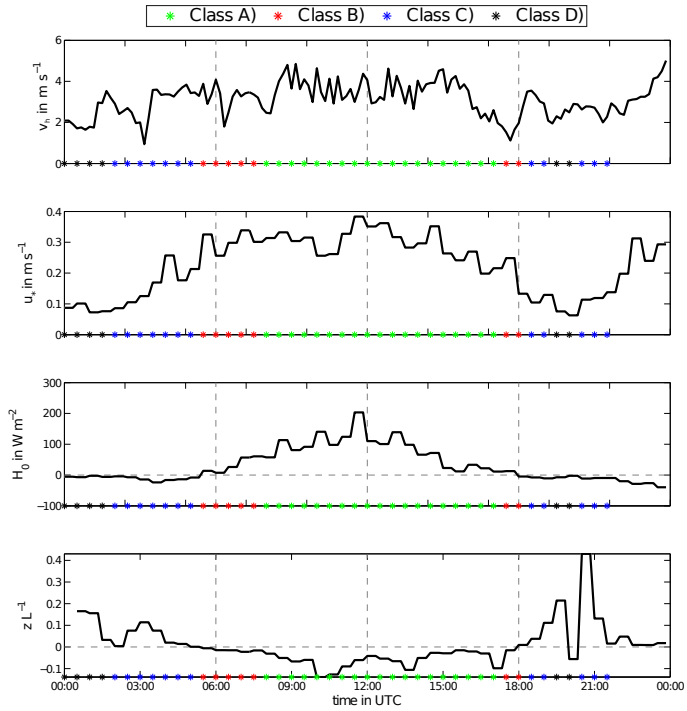

Figure 4.8: Atmospheric turbulent measurements of wind speed $\mathbf{v}_h$ in $\mathrm{m\,s^{-1}}$, friction velocity u_*in $\mathrm{m\,s^{-1}}$, sensible heat flux H_0 in $\mathrm{W\,m^{-2}}$, and Monin-Obukhov-length $\frac{z}{L}$ compared to the classification data. Green stars point out large coherent structures (Class A), red stars small coherent structures (Class B), blue stars low-intensity organization patterns (Class C), and black homogeneous wind fields (Class D). Measurements took place on 1 May 2013.

speed slightly decreases, while the sensible heat flux and also the friction velocity begins to increase. With the stronger turbulence, the intensity of the structures increases. From about 08:00 UTC on, the higher values of H_0 and u_*, respective to the negative values of the Monin-Obukhov-length $\frac{z}{L}$ point out a significant atmospheric turbulence. At this time, the observed coherent structures increase in length. Until 16:30 UTC, the wind speed $\mathbf{v}_h \approx 4\,\mathrm{m\,s^{-1}}$ and the friction ve-

locity $u_* \approx 0.3\,\mathrm{m\,s^{-1}}$ stays more or less constant. The sensible heat flux decreases from 12:00 UTC on. The increasing Monin-Obukhov-length discloses that the turbulence production reduced. Due to less atmospheric turbulence, the length of the structures continually decreases, and between 16:30 UTC and 16:40 UTC large coherent structures were no longer present. From 16:50 UTC to 17:30 UTC, the length of the structures increased momentarily again, possibly connected to a simultaneous decrease of $\frac{z}{L}$ and increase of u_*. From 17:40 UTC on, the atmospheric turbulence diminished rapidly responding to the stabilizing stratification. Until sunset at 18:54 UTC, the sensible heat flux dropped to values below zero. The friction velocity depicts values around $u_* = 0.1\,\mathrm{m\,s^{-1}}$ and the Monin-Obukhov-length represents positive values. The organization in the wind field reacted to the decrease of turbulence production. From 17:40 UTC to 18:00 UTC, the observed small coherent structures lessened their intensity and after 19:00 UTC a homogeneous wind field remained.
The diurnal cycle of wind field classification as seen in these examples is indicative of various other days. With an increase of turbulence production, the intensity of organization first increases and then the structures gain in length. In the afternoon and in the evening when the turbulence reduces, the structures first scale down and then diminish, respectively. Furthermore, this example shows a correlation between a considerably high friction velocity above $u_* \approx 0.2\,\mathrm{m\,s^{-1}}$ and the existence of coherent structures.

Shear-forced Coherent Structures

Is it possible that the formation of coherent structures is exclusively held out by shear? The examination requires a nocturnal situation where strong winds – and thus a strong wind shear – occur. When the boundary layer is stably, respectively neutrally stratified, the buoyancy turbulence production is subordinate. Coherent structures in a nocturnal situation might originate from mechanically-driven turbulence. In Figure 4.9, the stable stratification between 00:00 UTC and sunrise at 4:31 UTC on 19 April 2013 is represented by the significantly negative values of

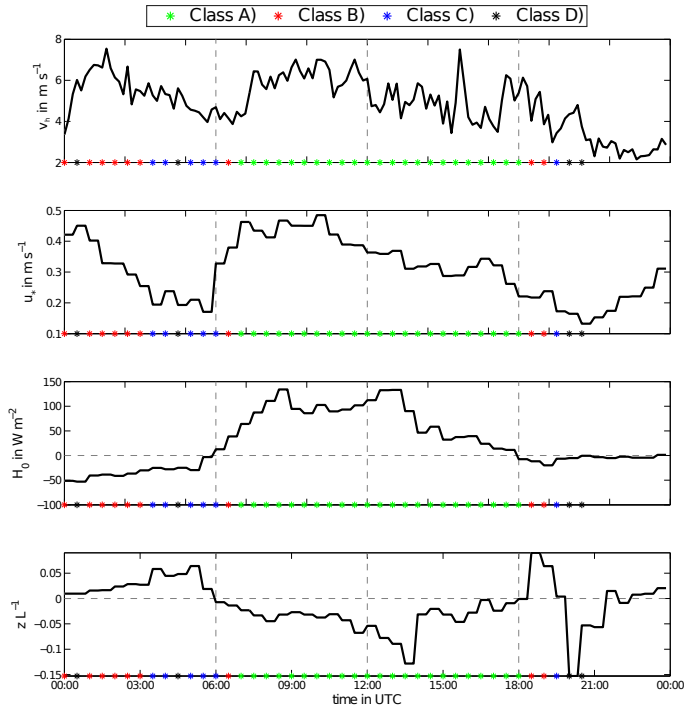

Figure 4.9: Atmospheric turbulent measurements compared to the classification data similar to Figure 4.8. Measurements took place on 19 April 2013.

$-50\,\mathrm{W\,m^{-2}} \leq H_0 \leq -25\,\mathrm{W\,m^{-2}}$. Higher wind speeds of $\mathbf{v}_h \geq 5\,\mathrm{m\,s^{-1}}$ occurring between 00:30 UTC and 03:00 UTC yield enhanced friction velocities between $0.25\,\mathrm{m\,s^{-1}} \leq u_* \leq 0.45\,\mathrm{m\,s^{-1}}$. The Monin-Obukhov length around 00:00 UTC depicts values slightly above zero. Coupled with the decrease in wind speed and friction velocity after 03:00 UTC, the Monin-Obukhov length rises to more positive values. During the whole morning hours, the classification data exhibits small coherent structures; around 03:00 UTC they also reach the critical length of 1 km for a short time frame. Even though the friction velocity drops to values of $u_* = 0.2\,\mathrm{m\,s^{-1}}$ from 03:30 UTC to 06:00 UTC, the intensity of the organization

patterns is still considerably high. The analysis of Figure 4.8 shows that coherent structures were present at all times when the friction velocity reached values of $u_* \geq 0.2\,\mathrm{m\,s^{-1}}$. In Figure 4.9, the friction velocity rarely dropped below this value. The organizations' further evolution of coherent structures is comparable to the previous example in Figure 4.8. Especially during daytime, large coherent structures develop when shear and buoyancy rise above a certain level. In the evening, around 18:40 UTC, small coherent structures are present in the absence of buoyancy-driven turbulence. At this time, the moderate wind speeds of $\mathbf{v}_h \geq 5\,\mathrm{m\,s^{-1}}$ and also the friction velocity of $u_* \geq 0.2\,\mathrm{m\,s^{-1}}$ are considerably high. The turbulence by shear might be sufficient at this time for coherent structure formation. Thus, this example points out that high mechanically-induced turbulence caused by high wind speeds is able to trigger coherent structures in the wind field in the absence of buoyancy effects.

Shear as an Important Driving Mechanism

The example displayed in Figure 4.10 shows how the existence of coherent structures depends on shear-driven turbulence production, when the atmospheric boundary layer is unstably stratified.

Before sunrise on 7 April 2013 at 04:57 UTC, the sensible heat flux was levelled at $H_0 = 0\,\mathrm{W\,m^{-2}}$. Due to the low wind speeds around $\mathbf{v}_h \approx 1\,\mathrm{m\,s^{-1}}$, the corresponding friction velocity is recorded at $u_* = 0.05\,\mathrm{m\,s^{-1}}$. The previous examples have shown that the existences of coherent structures coincides with enhanced friction velocities higher than $0.2\,\mathrm{m\,s^{-1}}$. The Monin-Obukhov-length reveals stable condition with positive values. After sunrise until 09:00 UTC the sensible heat flux rises to values of $H_0 = 100\,\mathrm{W\,m^{-2}}$. The friction velocities also increase about $0.1\,\mathrm{m\,s^{-1}}$, indicating a significant amount of mechanically-generated turbulence. During that time, the wind speed is low at $\mathbf{v}_h \approx 1\,\mathrm{m\,s^{-1}}$. The Monin-Obukhov-length decreases significantly due to the buoyancy-induced turbulence. During the whole morning, there are no coherent structures present in the wind field. Low-intensity organization is only developed between 05:00 UTC

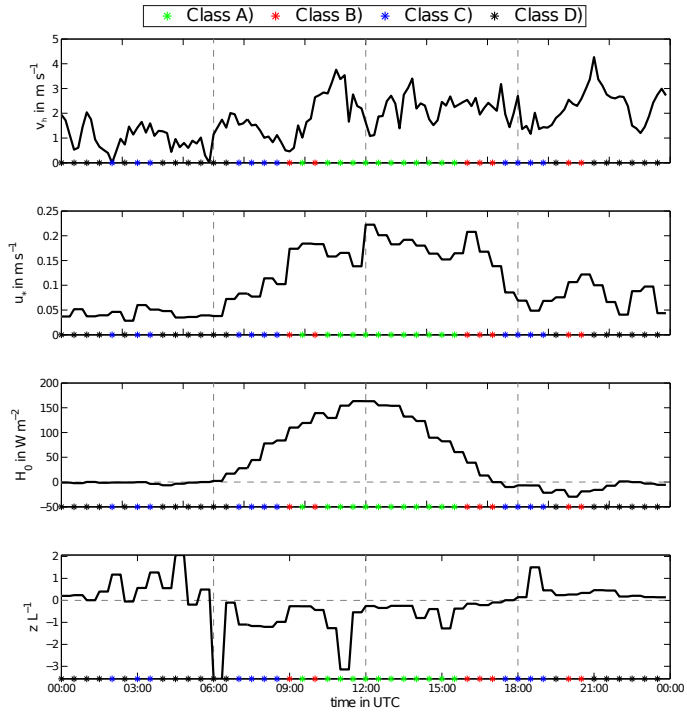

Figure 4.10: Atmospheric turbulent measurements compared to the classification data similar to Figure 4.8. Measurements took place on 7 April 2013.

to 06:00 UTC and from 07:30 UTC to 08:40 UTC. It seems that in the absence of considerable shear-generated turbulence production, coherent structures do not tend to develop. The first coherent structures on this day appeared around three hours after sunrise. The first example in Figure 4.9 has shown that the first coherent structures develop significantly earlier, when the boundary layer is unstably stratified. From 08:50 UTC onward, the wind speeds increases up to $3.8\,\mathrm{m\,s^{-1}}$; the friction velocity also rise to values around $0.2\,\mathrm{m\,s^{-1}}$. Corresponding to the abrupt rise of the friction velocity, the formation of large coherent structures begins and from then on occur till 16:20 UTC. Afterwards, the decreasing sensible

heat flux and friction velocity indicate in less turbulent boundary layer, which is also indicated by positive values of the Monin-Obukhov-length after sunset. The low turbulence production leads to the retrogression of coherent structures back to a homogeneous wind field. When during 20:00 UTC and 20:40 UTC the friction velocity increased, small coherent structures developed in the wind field.

Summary

The case studies presented in Figures 4.8 - 4.10 illustrate how the existence of coherent structures correlates with high values of friction velocity and sensible heat flux. The development of coherent structures in the measurement domain seems to begin when the turbulent production in the atmospheric boundary layer increases, whether this is buoyancy-induced or mechanically-generated. Normally, during daytime when the sensible heat flux is significantly high, coherent structures are present. When the friction velocity is negligible and the buoyantly-generated turbulence is also low, the wind field is able to maintain homogeneity during nighttime. However, coherent structures are not only a feature of the atmospheric boundary layer during daytime hours. In the absence of buoyantly-driven turbulence, though, coherent structures are able to develop. Due to higher wind speeds resulting in higher friction velocity, the turbulence production by shear can be sufficient enough to cause the development of coherent structures. Nocturnal coherent structures appear very frequently, but generally do not exceed a length of 1 km. Mostly, large coherent structures appear during daytime hours. This correlates with higher values of sensible heat flux, indicating higher buoyantly-driven turbulence.

4.2.2 Statistical Examination

The examination of Figures 4.8 to 4.10 has shown that coherent structures appear when whether the shear- or buoyancy-driven turbulence is sufficient. Because the case studies are rather qualitative than quantitative, this section analyses the clas-

Table 4.1: Statistics of classification data set over the duration of the measurement campaign from 4 April 2013 to 23 May 2013.

	Total		Day		Night	
Class	CNT	Perc.	CNT	Perc.	CNT	Perc.
A)	476	24.7 %	454	48.6 %	22	2.2 %
B)	542	28.2 %	317	34.0 %	225	22.7 %
C)	349	18.1 %	120	12.9 %	229	23.1 %
D)	557	29.0 %	43	4.6 %	514	51.9 %
$\sum$	1924		934		990	

sification data statistically. All in all, 1.924 10-minute-intervals were classified based on the described classification method (see Section 4.1.1). This accounts for over 320 hours of measurement data. Table 4.1 indicates the distribution of the classes regarding daytime events (06:00 UTC to 18:00 UTC), nighttime events (18:00 UTC - 06:00 UTC), and the whole data set. The analysis of data taken during daytime considers 934 intervals; during nighttime, 990 intervals are included in the analysis and thus represents a more or less evenly distributed data set. In total, the share of Classes A), B), and D) comprise between 24.7 % and 29.0 % of the intervals. Class C) represents the fewest intervals with 18.1 %. During daytime, the dominant share of Class A) with 48.6 % indicates that large coherent structures appear most frequently between 06:00 UTC and 18:00 UTC. Small coherent structures cover more than a third of daytime events. Very few Class D) intervals appear during the daytime (4.6 %). Obviously, within this time frame a distinct tendency for the development of coherent structures exists. The nocturnal intervals reveal a different behavior. With only 2.2 % of the data, Class A) events are underrepresented, and with 51.9 %, Class D) is the dominant class within the nocturnal boundary layer. Class C) gained in importance on account of Class B). Thus, during nighttime, the low-intensity organization and especially

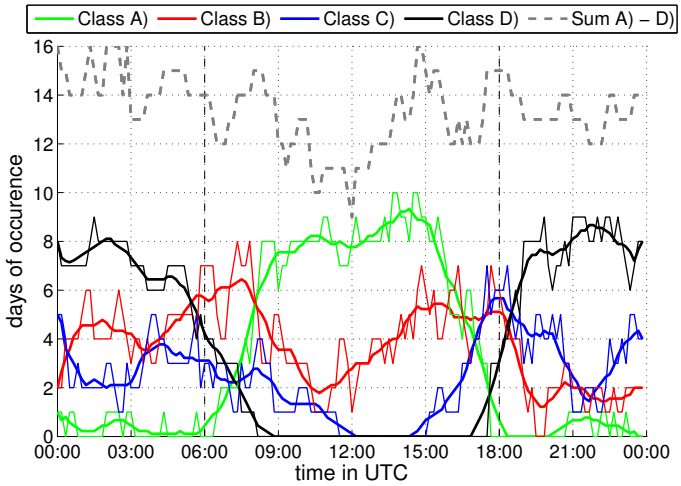

Figure 4.11: Diurnal distribution of classification data: thin (original data) and thick (smoothed data) colored lines represent large coherent structures (Class A, green), small coherent structures (Class B, red), low-intensity organization (Class C, blue), and homogeneous wind fields (Class D, black) and grey dashed line points out the sum of all Classes A) - D) over the duration of the measurement campaign from 4 April 2013 to 23 May 2013.

homogeneous wind fields appear very frequently (75.1 %) and most of the existent coherent structures in the nocturnal boundary layer are classified as small structures.

Figure 4.11 visualizes the distribution of the classification data in dependence of the daytime. Classes B) and C) are distributed in a more homogeneous way than Classes A) and D). Whereas during daytime hours, large coherent structures (Class A) appear most frequently, Class D) is dominant during nighttime. On the other hand, the importance of large coherent structures in the nocturnal boundary layer is negligible; within the turbulent boundary layer by day, homogeneous wind fields cannot be identified.

The case studies in Figures 4.8 - 4.10 suggested that large coherent structures appear mainly within daytime hours, whereas wind fields not containing any struc-

tures are a feature of the nocturnal boundary layer. Figure 4.11 confirms these findings, as large coherent structures almost exclusively (95.4 %) show up during daytime and 92.3 % of all events related to Class D) take place during nighttime. In contrast to that, Classes B) and C) are more evenly distributed over the whole day. Small coherent structures appear most frequently in the early morning between 05:00 UTC and 08:00 UTC and in the afternoon from 15:00 UTC to 18:00 UTC, occurring less frequently during daytime and in the last hours of the day between 21:00 UTC and 00:00 UTC. Low-intensity structures are a common feature of the early evening between 18:00 UTC and 21:00 UTC and in the morning from 04:00 UTC to 08:00 UTC, but in contrast to small coherent structures they do not appear in the afternoon. Figure 4.12(a) links Classes A) - D) to

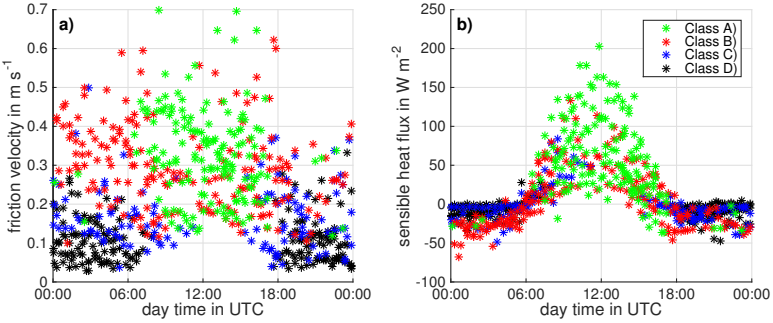

Figure 4.12: Diurnal distribution of classification data regarding the meteorological measurements of friction velocity in (a) and sensible heat flux in (b). Colored stars account for the classification data similar to Figure 4.8. Data set covers the measurements from 4 April 2013 to 23 May 2013.

the friction velocity. Homogeneous wind fields (black) appear nearly exclusively when $u_* \leq 0.20\,\mathrm{m\,s^{-1}}$. Only 9.2 % of all data referring to homogeneity occur when $u_* \geq u_{*,\mathrm{med}}$, where $u_{*,\mathrm{med}}$ is the median of all relevant friction velocity data with $u_{*,\mathrm{med}} = 0.20\,\mathrm{m\,s^{-1}}$. The mean friction velocity of all events related to Class D) is $\overline{u_{*,\mathrm{D}}} = 0.10\,\mathrm{m\,s^{-1}}$. Low-intensity organization takes place at a mean friction velocity of $\overline{u_{*,\mathrm{C}}} = 0.17\,\mathrm{m\,s^{-1}}$. Only 29.5 % of all events related to Class C) refer to $u_* \geq u_{*,\mathrm{med}}$. With a higher friction velocity, the intensity of the structure rises.

Table 4.2: Statistics regarding the dependencies to the friction velocity and the sensible heat flux over the duration of the measurement campaign from 4 April 2013 to 23 May 2013.

	Class A)	Class B)	Class C)	Class D)
$\overline{u_*}$	$0.33\,\mathrm{m\,s^{-1}}$	$0.30\,\mathrm{m\,s^{-1}}$	$0.17\,\mathrm{m\,s^{-1}}$	$0.10\,\mathrm{m\,s^{-1}}$
$\overline{H_0}$	$56.8\,\mathrm{W\,m^{-2}}$	$5.4\,\mathrm{W\,m^{-2}}$	$-3.9\,\mathrm{W\,m^{-2}}$	$-7.6\,\mathrm{W\,m^{-2}}$
$u_* \geq u_{*,\mathrm{med}}$	83.6 %	77.3 %	29.5 %	9.2 %
$u_* \leq u_{*,\mathrm{med}}$	16.4 %	22.7 %	70.5 %	90.8 %
$H_0 \geq H_{0,\mathrm{med}}$	89.1 %	49.5 %	32.4 %	30.9 %
$H_0 \leq H_{0,\mathrm{med}}$	10.9 %	50.6 %	67.6 %	69.1 %

This yields a mean friction velocity of $\overline{u_{*,\mathrm{B}}} = 0.30\,\mathrm{m\,s^{-1}}$ for small coherent structure events compared to $\overline{u_{*,\mathrm{A}}} = 0.33\,\mathrm{m\,s^{-1}}$ for large coherent structure events. 77.3 % of all small structure events and 83.6 % of all large structure events take place when $u_* \geq u_{*,\mathrm{med}}$. As the Class C) appears at higher friction velocity compared Class D), and coherent structures develop at even higher friction velocities, it seems that increasing friction velocity correlates with higher organization intensities. This behavior manifests in the visual clustering of all classes. When the friction velocity $u_* \geq 0.20\,\mathrm{m\,s^{-1}}$ the wind fields are neither homogeneous nor do they exhibit low-intensity structures. Homogeneity in the wind field occurs at a low friction velocity $u_* \approx 0.10\,\mathrm{m\,s^{-1}}$ and is located in the lowest part of the figure, whereas low-intensity events exhibit slightly higher values $\approx 0.15\,\mathrm{m\,s^{-1}}$. Events referring to friction velocities $u_* \geq 0.20\,\mathrm{m\,s^{-1}}$ mainly pertain to Classes A) and B). Large coherent structures occur primary during daytime and small coherent structures are spread over the whole day.

The sensible heat flux in Figure 4.12(b) shows that nearly all events accounting for homogeneity and for low-intensity organization take place when $H_0 \leq 0\,\mathrm{W\,m^{-2}}$. 69.1 % of all Class D) events, compared to 67.6 % of all Class C) events, occur when the sensible heat flux $H_0 < H_{0,\mathrm{med}} = -3\,\mathrm{W\,m^{-2}}$. The mean

values related to Class C) and D) are $\overline{H_{0,\mathrm{C}}} = -4\,\mathrm{W\,m^{-2}}$ and $\overline{H_{0,\mathrm{D}}} = -8\,\mathrm{W\,m^{-2}}$. Small coherent structures appear at a mean value of $\overline{H_{0\mathrm{B}}} = 5\,\mathrm{W\,m^{-2}}$ and 50.6 % of the small structure events take place when $H_0 > H_{0,\mathrm{med}}$. Large coherent structures develop under considerably higher values of $\overline{H_{0,\mathrm{A}}} = 57\,\mathrm{W\,m^{-2}}$ and 89.1 % of the large coherent structures refer to $H_0 > H_{0,\mathrm{med}}$. The existence of large coherent structures during the daytime is significantly correlated to higher sensible heat fluxes, whereas small coherent structures do not seem to be affected in the same way. The difference of $\overline{H_{0,\mathrm{A}}} - \overline{H_{0,\mathbf{B}}} = 51\,\mathrm{W\,m^{-2}}$ points out that both classes are perceptibly separated by H_0. The results regarding the sensible heat flux thus exhibits different relations compared to the friction velocity. The friction velocity seems to be an important driver for the intensity of the organization but does not primarily affect the extent of the coherent structures. In contrast to that, large coherent structures appear to be very likely when the sensible heat flux increases to values considerably higher than zero.

Figure 4.13 opposes the sensible heat flux on the abscissa to the friction velocity on the ordinate and thus combines both sets of information into one figure. Large coherent structures are presented in Figure 4.13(a). The colorbar indicates the number of detected events occurring under the conditions specified by H_0 and u_*. The error ellipses represent the two-dimensional histogram with a confidence interval of 50 % and 75 %, respectively. The center of the ellipses is specified by the mean values $\overline{H_0}$ and $\overline{u_*}$ from Table 4.2. As the histogram shows a large spread in both directions, the ellipses have a circular shape and cover a considerable area. The ellipsis representing a 50 % confidence interval shows a spread of about $\Delta H_0 \approx 120\,\mathrm{W\,m^{-2}}$ and $\Delta u_* \approx 0.27\,\mathrm{m\,s^{-1}}$ whereas the 75 %-ellipsis spreads about $\Delta H_0 \approx 170\,\mathrm{W\,m^{-2}}$ and $\Delta u_* \approx 0.39\,\mathrm{m\,s^{-1}}$. The center of both ellipses is placed at $\overline{H_{0,\mathrm{A}}} = 57\,\mathrm{W\,m^{-2}}$ and $\overline{u_{*,\mathrm{A}}} = 0.33\,\mathrm{m\,s^{-1}}$. The longest diameter of both ellipses is orientated in the direction of u_*. Most Class A) events occur when $u_* >= 0.2\,\mathrm{m\,s^{-1}}$ and $H_0 > 0\,\mathrm{W\,m^{-2}}$, which indicates a shear-driven and statically unstable atmospheric boundary layer. Events with small coherent structures (Class B) are displayed in 4.13(b); both ellipses exhibit differences compared to Class A). The mean sensible heat flux $\overline{H_{0,\mathrm{B}}} = 5\,\mathrm{W\,m^{-2}}$ is considerably

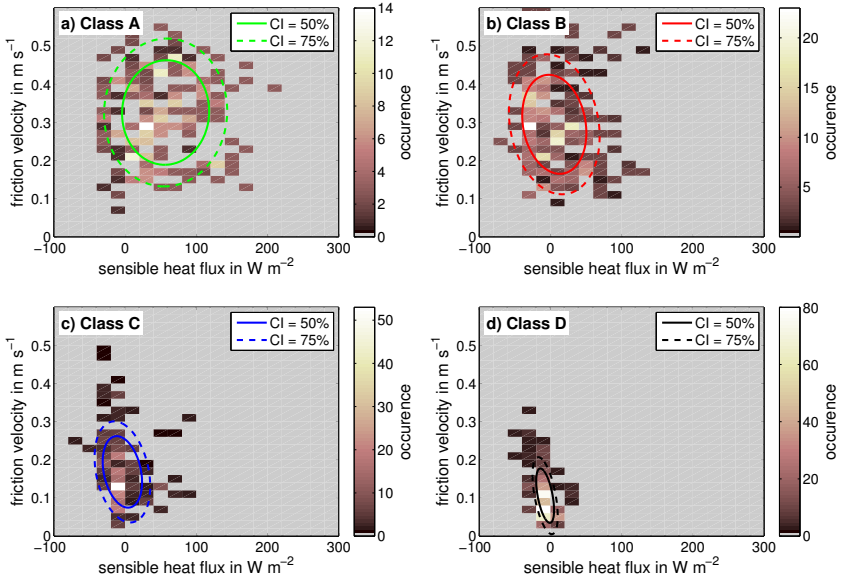

Figure 4.13: Combined visualization of the sensible heat flux and the friction velocity separated by Classes A) - D). Solid and dashed lines indicate error ellipses with a confidence interval of either 50 % or 75 %, respectively.

low compared to $\overline{H_{0,\mathrm{A}}}$ whereas the friction velocity $\overline{u_{*,\mathrm{B}}} = 0.30\,\mathrm{m\,s^{-1}}$ decreases insignificantly in comparison to $\overline{u_{*,\mathrm{A}}}$. A comparison of the results of Classes A) and B) points to the idea that the presence of large coherent structures strongly depends on buoyant turbulence production. Furthermore, the spread in the H_0-direction is around 30 % lower but stays constant in the u_*-direction; the ellipses exhibit a skewness, so higher values of u_* point out lower values of H_0 and vice versa. Small coherent structures are able to grow in size when the buoyant turbulence production increases. For this transition, under weakly sheared conditions, the buoyant turbulence production needs to exceed higher values compared to strongly sheared surface layer conditions. Within the 75 % confidence interval, no small coherent structures were present when the sensible heat flux was higher

than $H_0 \approx 70\,\mathrm{W\,m^{-2}}$. This shows that even moderate buoyant turbulence production is able to cause the existence of large coherent structures.

Events indicating low-intensity organization (Class C) are displayed in Figure 4.13(c). The mean values $\overline{H_{0,\mathrm{C}}} = -4\,\mathrm{W\,m^{-2}}$ and $\overline{u_{*,\mathrm{C}}} = 0.17\,\mathrm{m\,s^{-1}}$ indicate a primary shift in the u_*-direction compared to Class B) events. Whereas the sensible heat flux represents inconsiderably smaller values, the friction velocity dropped significantly. The ellipses in Figure 4.13(c) also exhibit a skewness. This explains that within a strongly stratified boundary layer, the friction velocity needs to exceed higher values in order to evolve coherent structures, whereas under neutral or weakly unstable conditions a smaller amount of mechanically driven turbulence suffices. The spread of both ellipses is reduced by another 30 % in both dimensions compared to the ellipses displayed in Figure 4.13(b). Figure 4.13(d) shows the events representing the homogeneous wind fields defined as Class D). The mean values $\overline{H_{0,\mathrm{D}}} = -8\,\mathrm{W\,m^{-2}}$ and $\overline{u_{*,\mathrm{D}}} = 0.10\,\mathrm{m\,s^{-1}}$ point out that the ellipses' center is also mainly shifted in u_*-direction compared to Class C) events. This shows that the main difference between Classes C) and D) is again based on shear-driven turbulence production. The spread in both dimensions reduces to $\Delta H_0 \approx 25\,\mathrm{W\,m^{-2}}$ and $\Delta u_* \approx 0.20\,\mathrm{m\,s^{-1}}$ and both ellipses exhibit a similar size. This shows that a very large amount of data referring to Class D) occurred under similar meteorological conditions. The skewness describes a co-dependence that compares Figures 4.13(b) and (c) and indicates that values of enhanced friction velocity, as well as increased sensible heat flux values, suffice to evolve low-intensity turbulence and coherent structures, respectively.

Figure 4.13 shows some characteristics regarding the development of coherent structures. In Figure 4.13(d), the ellipses represent a very distinct region referring to $H_0 \leq 0\,\mathrm{W\,m^{-2}}$ and $u_* \leq 0.2\,\mathrm{m\,s^{-1}}$. This is not surprising, as the development of turbulent structures is dependent on a certain amount of turbulence production, unavailable during these situations. With an increase in shear, low-intensity structures develop. As the analyses of Figures 4.11 and 4.12 have shown, low-intensity organization mainly develops during nighttime with an enhanced corresponding friction velocity in the morning, or during evening hours where the

sensible heat flux points out a higher buoyant-driven turbulence. Small coherent structures in Figure 4.13(b) refer to higher values of both u_* and H_0. As by definition, the main difference between Classes B) and C) is the intensity of the organization. It seems as though the turbulence production by shear is important for the step-wise development of coherent structures. This can be seen, for example, in the case study presented in Figure 4.8, where during the morning hours the classification first points out homogeneous events followed by low-intense structures and then evolves to developing small coherent structures. Large coherent structures occur when the sensible heat flux increases significantly. Under the influence of buoyantly-driven turbulence, large coherent structures tend to develop whether the friction velocity is high or not.

4.3 Formation Processes

The classification of coherent structures presented in this Chapter revealed that the length of the coherent structures strongly depends on the prevailing meteorological conditions. For example, Figure 4.11 has shown, that large coherent structures mostly appear during daytime and that small coherent structures – as well as low-intensity organization patterns – occur mostly in the morning and evening hours and during nighttime. The case studies in Figures 4.8 to 4.10 illustrate a typical evolution of the coherent structures. Nocturnal events – referring to a stably stratified boundary layer – with no containing coherent structures appear when whether shear-generated nor buoyancy-driven turbulence production is prevalent. Figure 4.13(d) shows, that events with no coherent structures occur when $\overline{H_{0,\mathrm{D}}} = -8\,\mathrm{W\,m^{-2}}$, as well as $\overline{u_{*,\mathrm{D}}} = 0.10\,\mathrm{m\,s^{-1}}$ are considerably low and point out an S^-B^--situation. Figure 4.11 shows, that during nighttime small coherent structures are able to form and Figure 4.13(d) points out that shear-induced turbulence production is responsible for nocturnal coherent structures. Referring to Table 4.1 small coherent structures occur in 22.8 % cases of all nocturnal events.

Other than events with no coherent structures, low-intensity organization seems

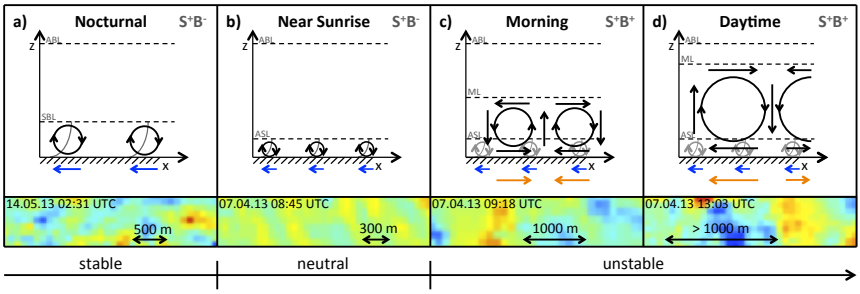

Figure 4.14: Processes of coherent structure formation under different atmospheric conditions (S^+B^- and S^+B^+ are introduced in Figure 2.3), (a) in the nocturnal stable boundary layer, (b) near sunrise under neutral conditions, (c) in the morning under unstable conditions, and (d) during daytime hours under unstable conditions. Blue (orange) arrows illustrate how shear-driven (buoyancy-induced) eddies influence the horizontal wind field. The measurements on (a) 14 May 2013, 02:31 UTC, (b) 7 April 2013, 08:45 UTC, (c) 7 April 2013, 09:18 UTC, and (d) 7 April 2013, 13:03 UTC present examples of structures of different sizes.

to be a common feature of the morning and evening boundary layer which is neutrally stratified. Figure 4.13(c) confirms an increase of the sensible heat flux $\overline{H_{0,\mathrm{C}}} = -4\,\mathrm{W\,m^{-2}}$ compared to $\overline{H_{0,\mathrm{D}}}$, as well as an increase in friction velocity $\overline{u_{*,\mathrm{C}}} = 0.17\,\mathrm{m\,s^{-1}}$ in comparison to $\overline{u_{*,\mathrm{C}}}$. With no buoyantly-driven turbulence available, shear-generated turbulence is responsible for coherent structures formation in the nocturnal boundary layer, as well as in the morning and evening hours.

Figure 4.14 is based on the description of Figure 2.3 but is more detailed regarding the evolution of the boundary layer in the morning, respectively evening hours, and furthermore suggests an explanation for the superstition of turbulent driving mechanisms. Figure 4.14(a) shows a nocturnal situation where shear is available in the lowest part of the atmospheric boundary layer and reaches up to heights comparable to the stable boundary layer (SBL). Shear-induced eddies cause coherent structures in the horizontal wind field near the ground, which manifest as regions of reduced wind speeds (blue arrow). The snapshot below

illustrates a nocturnal situation with small coherent structures taken at 14 May 2013 02:31 UTC. Coherent structures in this picture exhibit lengths of $\approx 500\,\mathrm{m}$. When the boundary layer is neutrally stratified, shear is available within the surface layer (ASL) which in general is less heigh than the stable boundary layer. Figure 4.14(b) shows that eddies within a neutrally stratified boundary layer are smaller and cause less intense coherent structures near the ground (blue arrows). The snapshot taken at 7 April 2013, 08:45 UTC confirms, that the organization pattern is less intense and the containing structures have a smaller horizontal extent. Within the analyses in this Chapter, patterns like these were defined as low-intensity turbulence. Situations like these not only occur in the morning hours, but are also a common feature of the boundary layer in the evening hours, when the buoyantly-driven turbulence decays.

When the buoyancy-driven turbulence production increases and the sensible heat flux exhibits slightly positive values $\overline{H_{0,\mathrm{B}}} = 5\,\mathrm{W\,m^{-2}}$, turbulence is available within the mixed layer ($S^{+}B^{+}$). Figure 4.14(c) illustrates up- and downward air motions allowing the formation of eddies with the size of the mixed layer, which cause significant areas of enhanced and reduced wind speed near the ground (orange arrows). The availability of shear ($\overline{u_{*,\mathrm{B}}} = 0.30\,\mathrm{m\,s^{-1}}$) within the surface layer causes the formation of smaller eddies near the ground. Shear-induced eddies (grey eddies within the surface layer) during daytime play a subordinate role compared to large buoyantly-driven eddies (black). The snapshot taken at 7 April 2013, 09:18 UTC shows the situation at the same day as shown in Figure 4.14(b) but exhibits considerably larger structures with the length of $\approx 1\,\mathrm{km}$.

The $S^{+}B^{+}$-situation in Figure 4.14(d) is comparable to Figure 4.14(c), but refers to a higher mixed layer caused by an increase in buoyantly-driven turbulence ($\overline{H_{0,\mathrm{A}}} = 57\,\mathrm{W\,m^{-2}}$). As the eddies have a larger vertical extent, also the horizontal coherent structures near the ground gained in size. On 7 April 2013, 13:03 UTC the structures are considerably larger than one kilometer and yield large coherent structures. Same as in Figure 4.14(c), shear with $\overline{u_{*,\mathrm{A}}} = 0.33\,\mathrm{m\,s^{-1}}$also induces eddies near the ground, but plays a subordinate role. But in strong wind situation, where the shear is considerable high, small eddies might gain in intensity and thus

the interaction between shear-generated and buoyantly-induced turbulence production might account for coherent structures of different sizes and appearances within an S^+B^+-situation.

Figure 4.14 provides an explanation of how different driving mechanisms of turbulence influence the formation of coherent structures in a boundary layer, whether it is stably, neutrally, or unstably stratified. This behaviour is in accordance to the findings of Barthlott et al. (2007) who state that structures occurring under stable conditions are generally shorter. It specifies the role of the height level which is influenced by shear and thus distinguishes between small coherent structures occurring at nighttime and low-intensity turbulence which occurs when the boundary layer conditions are less stable. In Section 5.2 it will be discussed whether shear influences the appearance of coherent structures or not.

4.4 Summary and Conclusion

The introduction of a manual characterization scheme allows to classify time intervals regarding the structures which occur within them. The definition of two relevant criteria, namely the intensity of the wind field and the horizontal extent of the organization patterns, clearly specifies four different classes. Class D) describes homogeneous wind fields where no organization pattern is present. Organization patterns with a low intensity ($\Delta u' < 2\,\mathrm{m\,s^{-1}}$) are defined as low-intensity events (Class C). When the intensity is sufficiently high, the events are defined as small coherent structure events (Class B) when the horizontal extent of the containing structures in mean wind direction is < 1 km, and as large coherent structures (Class A), when the horizontal extent of the structures in the mean wind direction exceeds 1 km.

Classifying the whole data set regarding the containing structure raises the ability to assess which meteorological parameters correlate with different classes and thus helps to understand how coherent structures develop in the atmospheric boundary layer. The case studies in Figures 4.8 to 4.10 have shown that the presence of coherent structures exhibit a diurnal cycle. A statistical examination

(Figure 4.11) enables a discussion of the occurrence accounting for the whole data set. Fifty-two percent of all nocturnal events represent homogeneous wind fields (Class D). In contrast to that, large coherent structures are the most dominant feature during daytime (Class A: 49 %). Low-intensity turbulence (Class C) is the dominant feature within the morning and evening hours. Small coherent structures (Class B) occur over the whole day.

As the friction velocity u_* represents the mechanically-generated turbulence production and the sensible heat flux refers to the buoyantly-driven turbulence, both indicate the source of turbulence necessary for the formation of coherent structures. Figure 4.13 shows that homogeneous wind fields (Class D) only occur when $H_0 \leq 0\,\mathrm{W\,m^{-2}}$ and $u_* \leq 0.2\,\mathrm{m\,s^{-1}}$. An increase of mechanical turbulence leads to low-intensity organization patterns in the wind field (Class C). A further increase in shear-generated turbulence yields the formation of small coherent structures (Class B). Large coherent structures (Class A) require buoyancy. When $H_0 \geq 70\,\mathrm{W\,m^{-2}}$, only a few events are not classified as a large coherent structure event. In contrast to large coherent structures, small coherent structures can occur any time, e.g. at night time, when the mechanically-generated turbulence is sufficiently high.

The conceptual model introduced in Section 2.2.3 suggests, that in the absence of buoyancy, shear- driven structures are generated near to the ground, where shear is dominant. These structures are caused by eddies orientated in the mean shear. Therefore the height of the shear level limits the diameter of the eddies. Figure 4.14 uses the suggestions of the conceptual model in Figure 2.3 and provides an explanation of how structures develop during the diurnal cycle under different meteorological conditions. The role of the height, which is affected by shear explains, why organization patterns in the morning and evening hours are less intense than coherent structures during nighttime. Figure 4.11 now shows that large coherent structures are the most dominant feature of the boundary layer during daytime, and that large coherent structures rarely occur during nighttime hours. Further, Figure 4.12 indicates that the presence of buoyancy is a highly important factor for the development of large coherent structures. This substantiates

the assumption that the coherent structures gain in size similar to the increase in the size of the eddies in the boundary layer. Events with no coherent structures almost exclusively took place during the nighttime (Figure 4.11) in the absence of buoyancy (Figure 4.12). This shows that even a slight increase of buoyantly-driven turbulence supports the formation of both small coherent structures and large coherent structures.

5 Automatic Detection of Coherent Structures

Chapter 4 uses a classification scheme to characterize coherent structures regarding their visual appearance. Comparing the characterization to meteorological parameters allows researchers to draw a conclusion as to which driving mechanisms are relevant for the formation of coherent structures. These prior analyses are based on subjective interpretations and contribute to a qualitative characterization of coherent structures. Employing an automated detection algorithm for coherent structures within a horizontal wind field data set yields quantitative results that expand the conception of coherent structures. Furthermore, statistical analysis regarding the characteristics of the coherent structures in comparison to the underlying meteorological situation enhance the understanding of the formation processes of coherent structures.

5.1 Method Description

An automatic detection can be realized in several ways. Stawiarski (2014) applie a one-dimensional wavelet analysis as well as a clustering algorithm to LES model results and compare the results. The clustering algorithm lacks in performance due to the resolution of the data set showing a significant overestimation of the detected structure lengths. The wavelet analysis works reliably for structures significantly longer than the horizontal resolution $\Delta xy \approx 60\,\mathrm{m}$. Structures with a length $L > 5 \cdot \Delta xy$ are generally detectable and the algorithm shows solid results when the structures are longer than $L > 9 \cdot \Delta xy$. The results of Stawiarski (2014) show that the performance of the one-dimensional wavelet approach is promising. However, the application to measurement instead of simulation data has led to major performance problems, and therefore the wavelet analysis was

not applicable within the scope of this thesis (Section 5.1.3).
The threshold detection method (Section 5.1.1) uses a two-dimensional approach, which, in comparison to the wavelet analysis, shows a significantly better performance (Section 5.1.2) not only regarding general structure detection but also in the determination of parameters such as structure width and length. For this reason, the threshold detection method is the fundamental method that this chapter is based on. Results pointing out the disadvantages of the wavelet analysis method are presented in Section 5.1.3.

5.1.1 Threshold Detection Algorithm

The threshold detection algorithm is based on basic considerations. An automated coherent structure detection should be able to provide data to quantify coherent structures within the whole data set. A correct allocation of the structure leads to highly reliable values regarding the length and the width of the coherent structure. Reliability is an important requirement for the purpose of all subsequent analysis.
The threshold detection algorithm works in three steps: a) firstly, a filtering method similar to a two-dimensional binomial filter smooths out the edges of the structures within the measurement data set. b) A threshold separates coherent structures from the background turbulence. c) A linkage- and clustering-algorithm interprets the area of detection as ellipses which represent coherent structures and provide all required information regarding coherent structures like the length, the width, the aspect ratio, their energy, and the intensity.

Two-dimensional Filtering Method

On the one hand, applying a two-dimensional filter to the data set smooths the edges, which in the end leads to better detection results. On the other hand, small structures that are only the size of a few pixels or ramifications of greater coherent structures are smoothed out and therefore will not end up in the data set. Similar to the limitations of the wavelet analysis, this method does not detect very

1 0.05 %	2 0.09 %	4 0.19 %	8 0.38 %	16 0.76 %	8 0.38 %	4 0.19 %	2 0.09 %	1 0.05 %
2 0.09 %	4 0.19 %	8 0.38 %	16 0.76 %	32 1.51 %	16 0.76 %	8 0.38 %	4 0.19 %	2 0.09 %
4 0.19 %	8 0.38 %	16 0.76 %	32 1.51 %	64 3.02 %	32 1.51 %	16 0.76 %	8 0.38 %	4 0.19 %
8 0.38 %	16 0.76 %	32 1.51 %	64 3.02 %	128 6.05 %	64 3.02 %	32 1.51 %	16 0.76 %	8 0.38 %
16 0.76 %	32 1.51 %	64 3.02 %	128 6.05 %	256 12.10 %	128 6.05 %	64 3.02 %	32 1.51 %	16 0.76 %
8 0.38 %	16 0.76 %	32 1.51 %	64 3.02 %	128 6.05 %	64 3.02 %	32 1.51 %	16 0.76 %	8 0.38 %
4 0.19 %	8 0.38 %	16 0.76 %	32 1.51 %	64 3.02 %	32 1.51 %	16 0.76 %	8 0.38 %	4 0.19 %
2 0.09 %	4 0.19 %	8 0.38 %	16 0.76 %	32 1.51 %	16 0.76 %	8 0.38 %	4 0.19 %	2 0.09 %
1 0.05 %	2 0.09 %	4 0.19 %	8 0.38 %	16 0.76 %	8 0.38 %	4 0.19 %	2 0.09 %	1 0.05 %

Figure 5.1: Applied 9x9 filter matrix. The yellow element in the middle represents the element of analysis. All neighboring elements add up by the weighting factor, which is represented by the upper number in each cell. The percentages below show how neighboring elements influence the smoothing. The area covered by the filter varies regarding the horizontal resolution between 0.3 km^2 and 0.5 km^2.

small structures reliably. The elimination of very small structures using a stronger filter therefore is reasonable. Figure 5.1 introduces the two-dimensional filter that is applied to the data set. The filter matrix compares to a two-dimensional binomial filter, but instead of coefficients deduced from Pascal's triangle, the coefficients show a two-dimensional quadratic relation and thus emphasizes the center element. If the center element is strongly accentuated, the filtering is less intense. For the purposes of this thesis, different filters (binomial: 3x3, 5x5, 7x7, 9x9; quadratic: 3x3, 5x5, 7x7, 9x9) were tested. In the end the 7x7 and the 9x9 quadratic filter performed well. As measurement errors, for example, are treated more effectively using a greater averaging area, the 9x9 quadratic filter was the filter of choice.

Threshold Detection

In the study of Stawiarski (2014), two different wavelets are applied to the data set. The first one provides information about the most energetic scale and be-

haves like a filter, smoothing the data set. The second wavelet then detects the edges of coherent structures. Even if the application of the wavelet analysis did not show the demanded detection quality (see Section 5.1.3), the general process for an automated detection is held out similarly. After smoothing the data with a two-dimensional filter, a threshold criterion serves to detect the edges of coherent structures. As coherent structures are defined as enclosed regions of reduced or enhanced wind speeds (see Chapter 2), an appropriate threshold is able to discriminate coherent structures from the background signal. Choosing a threshold should be able to distinguish the locations of i) regions with enhanced wind speed, ii) regions with reduced wind speed, and iii) the background wind field.

The classification scheme in Chapter 4 was already based on the application of a threshold, to differentiate between coherent structures and low-intensity turbulence using the measure of intensity. If the difference between the lowest wind speeds within the areas of reduced wind speed and the highest wind speeds in the area of enhanced wind speed is greater than $2.0\,\mathrm{m\,s^{-1}}$, then the structure is defined as a coherent structure. Testing different thresholds led to the result that a threshold of $\pm 1.1\,\mathrm{m\,s^{-1}}$ worked best for the purposes of the automatic detection. If, within an area, the wind speed anomaly drops to a value below $-1.1\,\mathrm{m\,s^{-1}}$, the region is defined as the negative part of coherent structures and when the wind speed exceeds $+1.1\,\mathrm{m\,s^{-1}}$, the corresponding region is defined as the positive part of a coherent structure. Therefore, the threshold-detection yields a matrix $x_{i,j}$ representing three different states. $x_{i,j} = -1$ marks coherent structures with reduced wind speeds $u' < -1.1\,\mathrm{m\,s^{-1}}$, whereas $x_{i,j} = 1$ represents coherent structures with enhanced wind speeds $u' > 1.1\,\mathrm{m\,s^{-1}}$. $x_{i,j} = 0$ shows areas with no coherent structures and therefore $-1.1\,\mathrm{m\,s^{-1}} \leq u' \leq 1.1\,\mathrm{m\,s^{-1}}$. Both parts (the positive as well as the negative) exhibit similar characteristics and therefore the results compare. As most studies concentrate on the interpretation of the areas with reduced wind speed, this analysis also focuses on the characteristics of the negative parts.

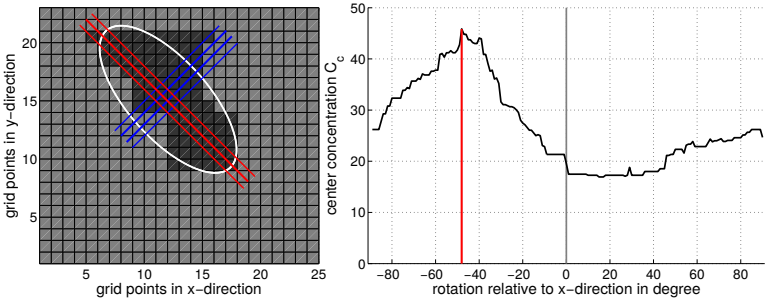

Figure 5.2: Illustration of the working principle of the clustering algorithm. The left picture shows an arbitrary cluster. Red lines mark the center lines in direction of the structures' main axis, blue lines in the direction of the structures' secondary axis. The white curve shows the algorithms interpretation of the cluster as an ellipse. The right picture represents the compactness factor on the y-axis along a rotation angle of the cluster on the x-axis to determine the most compact orientation. The red line indicates the maximum of the compactness factor and thus represents the structures' main axis.

Linkage- and Clustering-algorithm

The detection algorithm results in clusters of detection. The interpretation of these clusters within the three-state matrices is held out using a linkage and clustering algorithm. Johnson (1967) describes a technique which can be used to divide the detections within the matrix $x_{i,j}$ into separate connected areas. In this case, the algorithm rests upon the indices of neighbouring elements $x_{i,j} = -1$, respectively $x_{i,j} = 1$. Knowing the length, the width, and the location of a structure, allows researchers to interpret all linkages as ellipses. At first the determination of the main axis of the coherent structure is crucial. A self-developed algorithm rotates the linkages from -89° to 90° compared to the mean wind direction and checks in which direction the extent of the linkage is maximum. Figure 5.2 shows a cluster corresponding to an arbitrary coherent structure. Apparently, the main axis of the corresponding cluster is not orientated in the mean wind direction. The rotation of the cluster is determined using an algorithm which turns the linkage-cluster by one-degree angle γ step-wise and calculates a compactness parameter

$C_c(\gamma)$ of the cluster. The compactness parameter is a function that considers how compact the cluster is in its center. A weighted summation over the center rows along the main axis of the coherent structures (illustrated by red lines), results in significantly higher values like summing up the pixels in cross direction (illustrated by blue lines). The compactness factor in Equation 5.1 acts as a weighted summation that strongly accounts for the center rows and disregards the exterior ones.

$$C_c(\gamma) = \sum_{j=1}^{n} \left(\min(n-j, j-1) \cdot \sum_{i=1}^{m} x_{i,j}(\gamma) \right) , \tag{5.1}$$

where x is pointing in the assumed major axis, while y points in the assumed minor axis, m is the length of the cluster in x-direction and n the length in y-direction. i and j represent the control parameter in the x- and y-direction, respectively. Accumulating all members $x_{i,j}$ within a column, j represents the length of the structure. The pyramid-weighting factor $w(j) = \min(n-j, j-1)$ ensures a concentration of the members to the center of the structure which improves the behaviour regarding outlying detections. The calculation of $C_c(\gamma)$ is executed for degree-wise rotated matrices $x_{i,j}(\gamma)$ using rotation angles between $-89 \leq \gamma \leq 90$. The maximum of $C_c(\gamma)$ represents the longest major axis which directly yields in the orientation regarding the mean wind direction.

The right picture of Figure 5.2 shows the compactness parameter C_c in dependence to the relative rotation to the mean wind direction. The maximum indicates the rotation where the cluster is most compact. An ellipse representing the cluster is drawn in the left picture of Figure 5.2. The standard deviation of the distance of all elements to the major axis results in the width of the cluster (Equation 5.2):

$$C_w = \sigma_y(j(x_{i,j} = 1) - n/2) . \tag{5.2}$$

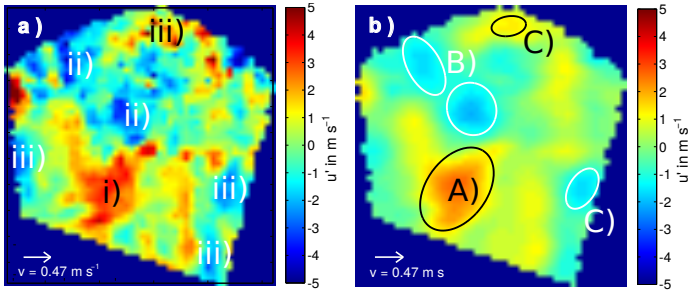

Figure 5.3: Presentation of a working example of the automated detection algorithm. Figure (a) represents the original image with markers i) to iii) for peculiar structures. (b) shows a filtered image of (a) where the ellipses A) to C) point to ellipses representing the detected structures. Measurements conducted on 17th April, 2013 at 13:03 UTC.

To ensure the area covered by the cluster equals the area covered by the corresponding ellipse, the length of the structure is calculated by the ratio between the covered area C_a and the width of the cluster C_w:

$$C_\mathrm{l} = \frac{C_\mathrm{a}}{C_\mathrm{w}} = \frac{\sum_{i=1}^{m}\sum_{j=1}^{n} x_{i,j}}{C_\mathrm{w}} \,. \tag{5.3}$$

Another possibility to establish an ellipse-based interpretation of a cluster is given by error ellipses. But error ellipses do not represent equal areas as the clusters evaluated by the linkage algorithm. In contrast to that, the clustering algorithm – as introduced in Equations 5.1 to 5.3 – is normalized by the area of the cluster and therefore offers a reliable representation of coherent structures.

Figure 5.3 shows the performance of the two-dimensional smoothing and the elliptical interpretation of structures on 17th April, 2013 at 13:03 UTC in the afternoon. Figure 5.3(a) illustrates the original wind field. The algorithm is designed to focus on the greater structures. The main features within this figure are a huge area of enhanced wind speed (i) in the lower left part of the picture and a huge part of reduced wind speed (ii) in the middle of the picture. At the edges of the figure, there are several smaller parts (iii) with enhanced and also reduced wind speeds.

The filter algorithm now considerably smooths the wind field and small objects vanish. After the application of the threshold detection method and the clustering algorithm, the main features are interpreted as one huge ellipse of enhanced wind speed (A) and as two ellipses (B), representing the region of reduced wind speed in the middle of the image. At the edges the two most intense features (C) are also interpreted as small ellipses. As this wind field shows a situation where various sizes of structures are mixed, it can be discussed whether the large region of reduced wind (ii) should be interpreted as one large ellipse or as two smaller ones. The original wind field shows a separation, where small areas of enhanced wind speed divide the structures at (ii) into two ellipses (B). From this point of view, the interpretation as two ellipses is reasonable. Within the manual characterization this event was classified as resulting in large coherent structures (Class A, see Chapter 4) with a length of ≥ 1 km. Within the corresponding 10-minute time interval, the automatic detection algorithm represents 34 detected coherent structures with a median length of 1005 m at an aspect ratio of 1.5. The detection therefore agrees with the manual characterization.

5.1.2 Performance of Automatic Detection Method

Figure 5.3 already illustrated the working process at one example and shows the general performance. Figures 5.4(a) to (d) present four other examples where the algorithm works properly. Otherwise, Figures 5.4(e) and (f) show examples where the algorithm is also sensitive for structures that are not related to turbulence in the horizontal wind field. All images combine the information of the filtered wind field with the resulting ellipses. Figure 5.4(a) shows a wind situation on 8$^{\text{th}}$ April, 2013 at 11:03 UTC. Under wind speeds of 6.5 m s^{-1}, structures with maximum lengths of about 2000 m were located all over the wind field. The regions of enhanced wind speed are perfectly represented by black ellipses, whereas the regions of reduced wind speed are represented by white ellipses. Dashed ellipses accounting for areas located outside the image (in the upper part of the image) point out structures which might continue. These structures will

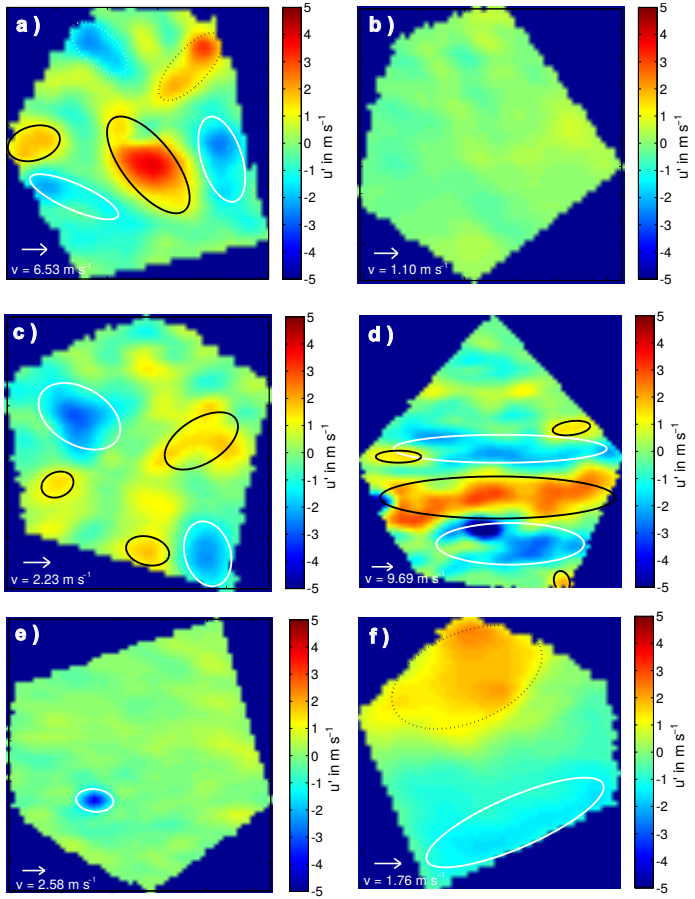

Figure 5.4: Six working examples representing the performance of the automated detection algorithm. (a) captured on 8th April, 2013 at 11:03 UTC, (b) on 7th April, 2013 at 08:45 UTC, (c) on 7th April, 2013 at 14:31 UTC, (d) on 12th April, 2013 at 08:45 UTC, (e) on 17th April, 2013 at 07:15 UTC, and (f) on 7th April, 2013 at 02:18 UTC.

be ignored in the subsequent analysis, as the real dimension might be misinterpreted. The manual characterization refers to large coherent structures and agrees with the automatic detection method. Thirty-five detected coherent struc-

tures with a median length of 1760 m and a corresponding aspect ratio of 2.8 are representing large and strongly elongated structures. Figure 5.4(b) gives on overview of a wind situation in the morning of 8th April, 2013 at 08:45 UTC. Some low-intensity structures with small horizontal extent spread all over the image, as the algorithm is not designed to detect these structures. As the manual characterization refers to a low-intensity event, the detection algorithm agrees in this case. Within the 10-minute time interval, one structure with a length of 435 m and an aspect ratio of 1.4 was detected. Another situation where the detection algorithm was intended to detect small coherent structures within the domain is shown in Figure 5.4(c). Weak winds of 2.2 m s^{-1} on 7th April, 2013 at 14:31 UTC caused a mid-sized area of enhanced wind speed in the left part of the picture and a mid-sized area of enhanced wind speed in the right part. Both areas are well-represented by ellipses. At the edges, some smaller structures also result in detections of coherent structures that might continue in the outer part of the image. Unfortunately, the detection algorithm did not rule them out. So this example is also a clue as to the small structures that remain in the data set. Nevertheless, the working performance within the 10-minute time interval satisfies. The 46 detected structures refer to a median length of 1545 m and an aspect ratio of 2.2, which agrees with the manual characterization accounting for large coherent structures. Figure 5.4(d) represents a strong wind situation, where winds of 9.7 m s^{-1} caused highly elongated structures that are perfectly aligned in the mean wind direction. The three dominant streaks were perfectly interpreted as structures that were parallel to each other. Just as in the previous example, the algorithm did detect three small coherent structures at the edge of the figure, which were definitely part of the bigger structures, therefore raising the amount of very small coherent structures in the data set. Obviously, the manual characterization method accounts for large coherent structures in this case. The automated detection method represents 18 coherent structures with a median length of 2028 m and an aspect ratio of 2.6. The situation in Figure 5.4(e) is comparable to the low-intensity situation in Figure 5.4(b). Here, a hard target measurement error causes a false detection. These false detections can be easily handled, as they ex-

hibit unreasonably high or low velocities $\approx \pm 40\,\mathrm{m\,s^{-1}}$. As the highest velocities measured within the whole campaign did not exceed values of $\pm 15\,\mathrm{m\,s^{-1}}$, a filter of $\pm 25\,\mathrm{m\,s^{-1}}$ rules out the hard target effects. All in all, twelve structures were observed by the automated detection method. These structures were comparably round (aspect ratio: 1.4) and just 523 m long.
Another problem that will be referred to later on presented in Figure 5.4(f). Wind shear occurring on 7$^{\mathrm{th}}$ April, 2013 at 02:18 UTC is not covered by the application of the 2-h running-mean (see Section 3.2.4). In the wind field, the shear remains as two areas with enhanced and reduced wind speed, respectively. Both covering about a third of the whole measurement domain. The area of reduced wind speed refers to measurements near the ground, whereas the area of enhanced wind speed is located at higher altitudes. Therefore the gradient is not a cause of horizontal inhomogeneity but rather refers to vertical shear. Unfortunately, these structures remain in the data set. Within the manual characterization, the shear could easily be disregarded. So this interval was classified as an event with no coherent structures. The automated detection method observed 37 very large coherent structures with a median length of 2709 m instead.
All in all, the performance of the automatic detection algorithm as applied within this thesis suffices the objectives. Some weaknesses like the detection of wind shear in the nocturnal boundary layer or smaller structures at the edges of the domain could hardly be dealt with. But a high number of structures are detected as desired.

5.1.3 Alternative Detection Methods

An alternative approach, which was analysed thoroughly in the scope of this research, is the coherent structure detection using a one-dimensional wavelet analysis. Such an analysis was applied and tested in the study of Stawiarski (2014). All analyses were conducted using an LES model that contains coherent structures. The wavelet analysis worked reliably for structures significantly longer than the horizontal resolution $\Delta xy \approx 60\,\mathrm{m}$ of the dual-Doppler measurements.

The WAVE wavelet has a similar shape to coherent structures in wind speed signals. Using the WAVE wavelet helps to determine on which scale the wind signal is most energetic and gives a clue as to which scale the most important structures have to be expected. In the second step, the MEXICAN HAT wavelet is used to detect the edges of the structures at the most energetic scale, often referred to as dominant scale. The combination of all one-dimensional detections can be transferred to a two-dimensional detection matrix. The application of the linkage- and clustering algorithm results in elliptical interpretations for detections of coherent structure, analogue to the threshold detection method (Section 5.1.1). But as each one-dimensional data signal is interpreted independently from each other, the results often differ drastically. This leads to at least two commonly appearing false detection. Firstly, two small independent structures can be combined to one large one, if the algorithm also detects structures in between. Secondly, when the algorithm fails to interpret a structure within a one-dimensional signal, a large coherent structure can be separated. Especially when the measurement quality drops, the detection algorithm regularly fails. From this point of view, the wavelet analysis was hardly applicable to this measurement data set.

5.2 Results

The following section introduces the results of the automated detection algorithm of coherent structures. Section 5.2.1 is occupied with characteristics of coherent structures, e.g. the length, the width, and the aspect ratio. A statistical comparison to meteorological parameters to determine the driving mechanisms for the formation of coherent structures is shown in Section 5.2.2. Also in Section 5.2.2, an estimation of the energy of coherent structure determines which coherent structures contribute considerably to the energy budget.

5.2.1 Characteristics of Coherent Structures

Figure 5.5 shows the two-dimensional distribution of coherent structure detections in dependence of the daytime on the x-axis and the length of the structures in

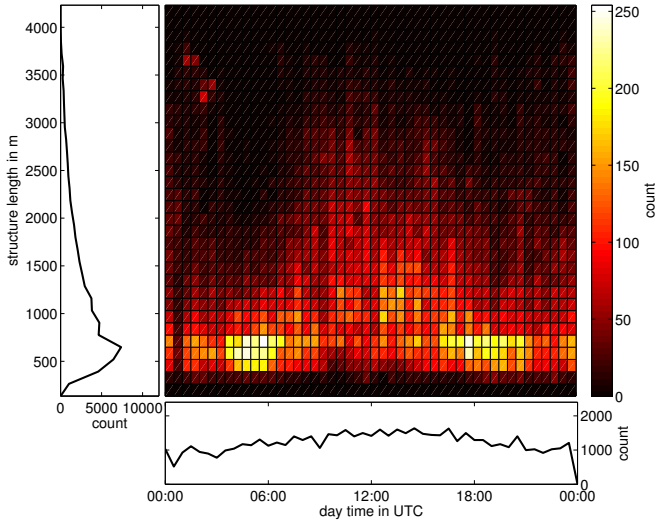

Figure 5.5: Two-dimensional histogram of the diurnal distribution of the length of coherent structures. The data set is based on measurements from 7th April, 2013 at 00:00 UTC to 23rd May, 2013 at 23:59 UTC.

meters on the *y*-axis. The colors indicate the total frequency of occurrence for the whole data set. The curves in the panels below and left of the two-dimensional histogram feature the one-dimensional distributions regarding the variable displayed on the corresponding axis.

The two-dimensional histogram features information on the diurnal distribution of the coherent structures, but also on the automatically detected specific length-scales. Two results in this figure are striking. At first, coherent structures with lengths over 1500 m show up mainly during daytime, as indicated by the reddish colors in the middle of the histogram. There is a significant increase in occurrence between 08:00 UTC and 16:00 UTC. Secondly, in the morning around 06:00 UTC and also in the evening around 18:00 UTC, two clusters at small length scales between 500 m and 700 m show a very high number of occur-

rences. Generally, small structures seem to appear more frequently compared to long structures. The one-dimensional distribution of coherent structures regarding their lengths reveals that structures with a length of about 600 m have a high number of occurrences.

Do small coherent structures really appear more often than large coherent structures? Given a certain domain of observation – e.g. this dual-Doppler lidar setup – it is obvious that several small coherent structures can be observed within this domain. Large coherent structures cover a larger area; therefore within the same domain, only a few large coherent structures can be observed. From that point of view, the distribution regarding the lengths is strongly biased. The development of a correction method that accounts for this bias shows that coherent structures of all length scales are detected by a similar frequency. Assuming that the area covered by the coherent structures is directly dependent on the length of the structures leads to a measure of coverage in dependence to the length. The ratio between the size of the measurement domain and the structure coverage yields a ratio defined as the maximum observability $Obs_{\max}$. This correction algorithm strongly reduces the frequency regarding small coherent structures and thus emphasizes the importance of large coherent structures. The ratio between the length of a structure and the width of a structure is often referred to as aspect ratio r_{asp}. Figure 5.6 shows the distribution of the aspect ratio in dependence to the length of the coherent structures. Small coherent structures often belong to aspect ratios inconsiderably higher then 1 and represent nearly round coherent structures. With an increase of the length-scales, the maximum aspect ratios also increase. This of course is also determined by the measurement principle, as the measurements are limited to the horizontal resolution of the underlying measurement principle, which in this case is between 60 m and 78 m. As artifacts with a width of one data point generally are smoothed out by filtering, the first percentile of all detected widths is $w_{1\text{perc}} = 201$ m, and the absolute minimum is $w_{\min} = 107$ m. Large coherent structures often can reach multiple values of the minimal width, whereas small coherent structures do not. Over the whole distribution the maximum aspect ratios are between 8 and 11, but the majority of

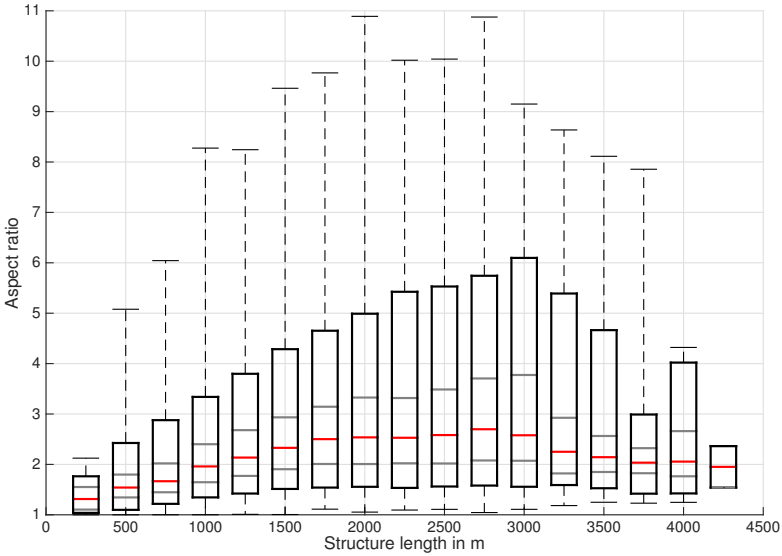

Figure 5.6: Distribution of the coherent structures aspect ratio in regards to the coherent structure lengths. Boxes represent the values between the 5$^{\text{th}}$ - and the 95$^{\text{th}}$ -percentile, markers represent the median (red), the 25$^{\text{th}}$ - and 75$^{\text{th}}$ -percentile (grey), and the minimum and maximum (black, outside the box).

the values are in the range between 1 and 3, as indicated by the median. The median also leads to a generalized dependence of the covered area to the structure lengths. Assuming that all coherent structures have the shape of an ellipse with the length a and the width $b = a \cdot r_{\text{asp}}(a)^{-1}$, one coherent structure covers an area of $A_{\text{CS}}(a) = \frac{\pi \cdot a^2}{4 \cdot r_{\text{asp}}(a)}$. The maximum observability (Equation 5.4) is therefore the ratio between total area of measurement domain $A_0 = 10\,\text{km}^2$ and the area covered by coherent structures $A_{\text{CS}}(a)$ dependent on a specific length a.

$$Obs_{\text{max}}(a) = \frac{A_0}{A_{\text{CS}}(a)} = \frac{A_0 \cdot 4 \cdot r_{\text{asp}}(a)}{\pi \cdot a^2} \tag{5.4}$$

Figure 5.7 compares to Figure 5.5, but shows differences in the distribution re-

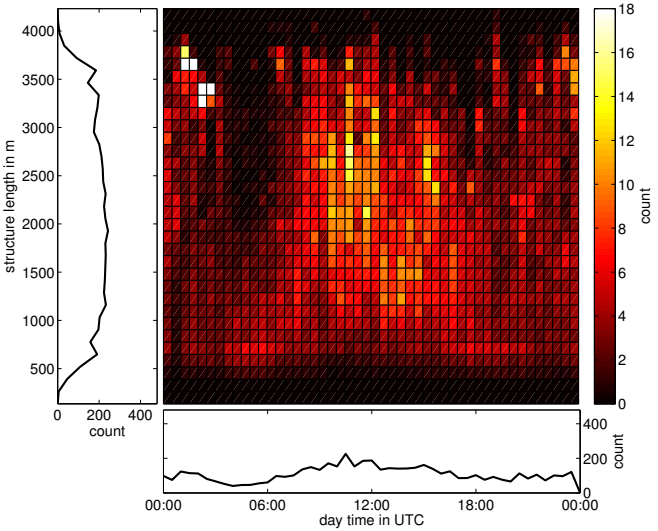

Figure 5.7: Two-dimensional histogram of the diurnal distribution of the length of coherent structures after the application of a weighting function, as explained in the text.

garding the lengths of the coherent structures due to the division by the correspondent values of the maximum observability function:

$$N_{\mathrm{W}}(a) = N(a)/Obs_{\max}(a)\ , \tag{5.5}$$

where $N(a)$ is the unweighted occurrence and $N_{\mathrm{W}}(a)$ the weighted number of occurrences, both dependent on the ellipses' length a. This leads to results where the high frequencies of small coherent structure detections is strongly reduced. The frequency of occurrence is roughly evenly distributed over all length scales between 600 m and 3500 m, which shows that the automated detection is capable of detecting structures with different lengths. Figure 5.5 brought up the idea that large coherent structures show a high number of occurrence during daytime. As the occurrence of large coherent structures is more accentuated in Figure 5.7, the

significance of the diurnal cycle is raised. During daytime, the coherent structure occurrence shows a maximum between lengths of 2000 m and 3000 m. The period of highest occurrences is located between 10:00 UTC and 14:00 UTC. In the evening and especially in the morning hours, the occurrence of large coherent structures is significantly reduced. In contrast to that, during nighttime coherent structures also reach high lengths and even show the absolute maximum occurrences around 02:00 UTC.

Are large coherent structures a dominant feature of the nocturnal boundary layer? As the measurements ware not conducted at a constant altitude, as illustrated in Chapter 3.2.3, especially nocturnal measurements, are affected by shear; large areas with different wind speeds are interpreted as very large coherent structures. Figure 5.4(f) presents an example of very large structure detections in a stably stratified environment within the nocturnal boundary layer.

Chapter 4 has shown that coherent structures exclusively driven by shear reach lengths up to 1000 m and appear mainly in the nocturnal boundary layer. Coherent structures also affected by buoyancy reach lengths significantly larger then 1000 m. These structures occur mainly during daytime. Figure 4.11 revealed the importance of low-intense structures in the morning and evening hours, when the boundary layer is neutrally stratified. The automated detection algorithm is designed only to detect intense coherent structures, but low-intensity structures were detected quite frequently and cause a high count of very small structures in the morning and evening hours. Separate investigations regarding different times of day allow researchers to draw conclusions about corresponding driving mechanisms. As stated before, coherent structures exclusively driven by shear generally appear during nighttime NOC. In Chapter 2.2.3, the definition S^+B^- accounts for these events. Low-intensity turbulence in the morning and the evening MOR, and large coherent structures driven by shear and buoyancy (S^+B^+) during daytime DAY. The definition of the three periods distinguishes between the different structures and accounts for different meteorological situations.

The nighttime is defined from 20:00 UTC to 04:00 UTC and daytime from

Table 5.1: Length, width, and aspect ratio of coherent structures gained from automated detection method. DAY refers to all measurements from 08:00 UTC to 16:00 UTC, NOC to nocturnal measurements from 20:00 UTC to 04:00 UTC, and MOR to measurements within the morning and evening hours from 04:00 UTC to 08:00 UTC and from 16:00 UTC to 20:00 UTC.

Length	**25th perc.**	**Median**	**75th perc.**
DAY	874 m	1312 m	1955 m
NOC	648 m	959 m	1643 m
MOR	635 m	883 m	1353 m
Width	**25th perc.**	**Median**	**75th perc.**
DAY	412 m	573 m	798 m
NOC	365 m	495 m	703 m
MOR	358 m	471 m	617 m
Aspect Ratio	**25th perc.**	**Median**	**75th perc.**
DAY	1.7	2.1	2.7
NOC	1.5	1.9	2.4
MOR	1.5	1.8	2.4

08:00 UTC to 16:00 UTC. The time periods between 04:00 UTC to 08:00 UTC in the morning and from 16:00 UTC to 20:00 UTC in the evening are combined in all following analysis. During daytime, 65.5 % of all detections show lengths larger than 1000 m; during nighttime the number is significantly smaller at 46.2 %. The morning and evening hours exhibit the smallest values of 39.4 %. Table 5.1 gives an overview of the characteristics of length, width, and aspect ratio calculated for the different regimes. It seems as structures appearing throughout daytime hours have a median length of 1312 m. The 75^{th} percentile of 1955 m and the 25^{th} percentile of 874 m show the spread of the detected lengths. The structures during daytime are considerably larger compared to the nocturnal events (959 m) with a similar spread. The lengths in the morning and evening

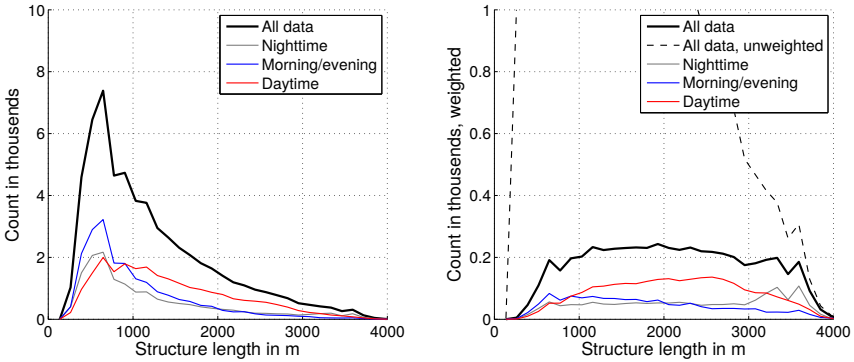

Figure 5.8: Distributions of coherent structures in regards to their lengths. In the left picture, the thick black curve represents the whole data set, the gray curve all nocturnal measurements, the blue curve measurements within the morning and evening hours, and the red curve measurements during daytime. The left picture is based on the weighted data set, the colors of the curves compare to the the left ones, but the black dashed line represents the unweighted curve of whole data set to illustrate the reduction of data.

hours are even smaller (883 m), but the spread is smaller. This shows that during daytime very large coherent structures are present and many different scales could be detected. There is a similar number of occurrence during night, but the lengths are smaller. In the morning and evening there are a lot of detections at similar and smaller scales. The analysis of the width shows similar results. At daytime, the median width is 573 m, whereas in the morning hours the structures exhibit a thickness of 471 m. The spread is similar for all time periods. The median aspect ratio during nighttime (1.9) is larger than in the morning and evening (1.8) but smaller than during daytime (2.1). The spread is nearly the same within all three periods. Keeping in mind that, the analysis of nocturnal detections is especially affected by detections due to wind shear, the lengths might be overestimated and in reality might compare to the values in the morning and evening hours.

Figure 5.8 illustrates one-dimensional histograms regarding the structure length. The left picture shows the data without the application of the weighting function,

whereas the right picture is based on the weighted data set. This figure confirms the results of the previous pictures. Both pictures show an increase of large coherent structures – larger than 1000 m– during daytime hours. Particularly in the morning hours, very small structures with lengths ≈ 700 m appear most frequently. The application of the maximum observability function in the right picture also reveals that nocturnal detections of large coherent structures significantly influence the data set. In all further analysis, these detections should be handled with care, as they represent the effect of wind shear instead of horizontal coherent structures. The weighting function is applied to this data set and only accounts for analysis regarding the structure length. Therefore in all following figures in Section 5.2.2, the data set is used as seen in the left picture. As the different time periods are assessed separately, using the unweighted data set does not aggravate the interpretation.

5.2.2 Meteorological Interpretation

The following analyses show dependencies of coherent structures regarding the length and the aspect ratio on meteorological conditions. The length of the coherent structure represents a meaningful measure for the horizontal extent of coherent structures, the aspect ratio directly illustrates the elongation of the structures.

Wind Speed Dependence

Figure 5.9 shows the two-dimensional distribution of coherent structures regarding the wind speed and the structure length. Panel (a) represents the whole data set, (b) data during daytime, (c) data during nighttime, and (d) data within the morning and evening hours. Figure 5.9(a) shows a cluster of counts (i), which is mainly concentrated at wind speeds from $0.7\,\mathrm{m\,s^{-1}}$ to $2.7\,\mathrm{m\,s^{-1}}$, where structures with lengths between 300 m and 700 m evolve. In these cases, the lengths

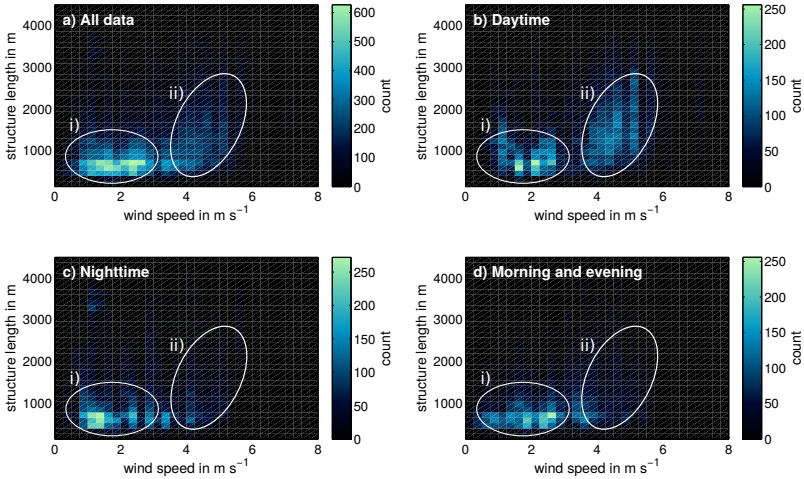

Figure 5.9: Two-dimensional distribution of coherent structures in regards to the structure length and the underlying wind speed. Ellipses i) and ii) represent areas of interest. (a) is based on the whole data set, (b) on measurements within daytime, (c) within nighttime, and (d) within the morning and evening hours.

of the structures are independent from the underlying wind speed. At moderate wind speeds between 3.2 m s^{-1} and 5.2 m s^{-1} another cluster (ii) of structure detection exhibits a dependence, where higher wind speeds coincides with longer structures. Figures 5.9(c) and (d) show that the cluster (i) with the small coherent structure mainly occurs during nighttime. Figure 5.5 has shown that many detections of small coherent structures occurred during nighttime and especially in the morning and evening hours. Figure 5.9 now states that many of these detections take place at low wind speeds. The same cluster is less pronounced in Figure 5.9(b). The cluster (ii) is only present during daytime. This leads to the result that in the presence of buoyancy, the wind speed correlates with the length of the coherent structure.

The dependence of the structures' elongation on the wind speed is examined in Figure 5.10. Same as in Figure 5.9, the diagrams are organized according to the

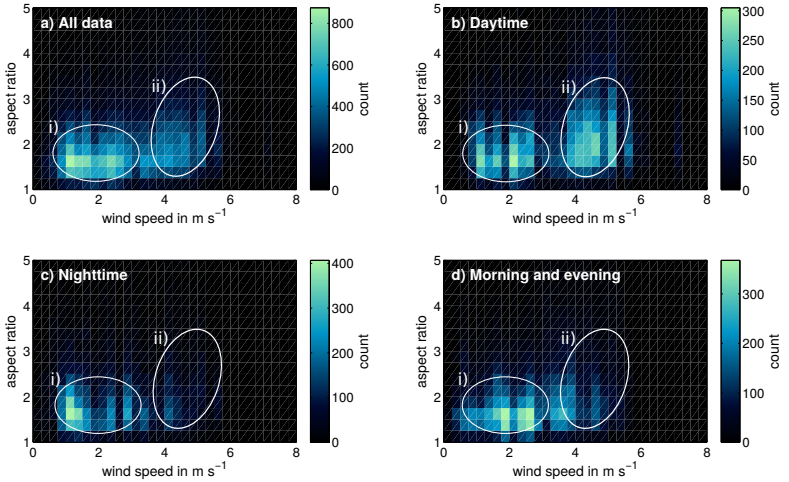

Figure 5.10: Two-dimensional distribution of coherent structures in regards to the aspect ratio and the underlying wind speed. Ellipses i) and ii) represent areas of interest. a) is based on the whole data set, b) on measurements within daytime, c) within nighttime, and d) within the morning and evening hours.

time of appearance. Figure 5.10(a) shows a graphic representing the whole data set, while Figures 5.10(b), (c), and (d) are restricted to specific periods. At lower wind speeds between 0.7 m s^{-1} and 2.7 m s^{-1} in Figure 5.10(a), the cluster (i) represents structures with elongations between 1.2 and 2.0. The degree of elongation is not dependent on the wind speed within this cluster. Many of these detections can be traced back to nocturnal detection or detection in the morning and evening (Figures 5.10(c) and (d)). Coherent structures with aspect ratios ≥ 3 are mainly a feature of the boundary layer at daytime. The cluster (ii) in Figure 5.10(a) is also displayed in Figure 5.10(b), but not in Figures 5.10(c) and (d). This cluster exhibits a similar shape in regards to the aspect ratio and in dependence to the wind speed in the range between 3.2 m s^{-1} and 5.2 m s^{-1}.

In summary, the wind speed influences the appearance of coherent structures. At wind speeds ≥ 3 m s^{-1}, the length of the coherent structures coincides with

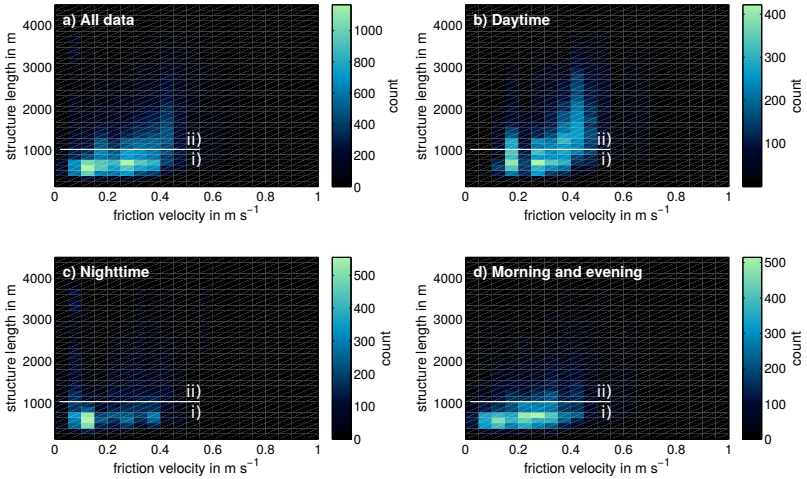

Figure 5.11: Two-dimensional distribution of coherent structures in regards to the structure length and the underlying friction velocity. The white line separates structure i) shorter than 1000 m and ii) longer than 1000 m. (a) is based on the whole data set, (b) on measurements within daytime, (c) within nighttime, and (d) within the morning and evening hours.

the wind speed in a buoyancy-driven boundary layer. Moreover, the elongation of coherent structures shows comparable results, as the coherent structures get longer and thinner under the influence of higher wind speeds.

Other than the wind speed, the friction velocity accounts for the ground's force to reduce the wind speed. Figure 5.11 shows the two-dimensional distribution of structures depending on the structure's length and the underlying friction velocity. The evaluation, whether the length of the coherent structures is dependent on the friction velocity, is held out by following the same argumentation as used within the methods in Chapter 4. The separation of large coherent structures with a length ≥ 1000 m and small coherent structures (< 1000 m), quantitatively shows that the growth of coherent structures depends on the friction velocity. This finding seems to be in contradiction to the assumption made in Chapter 4,

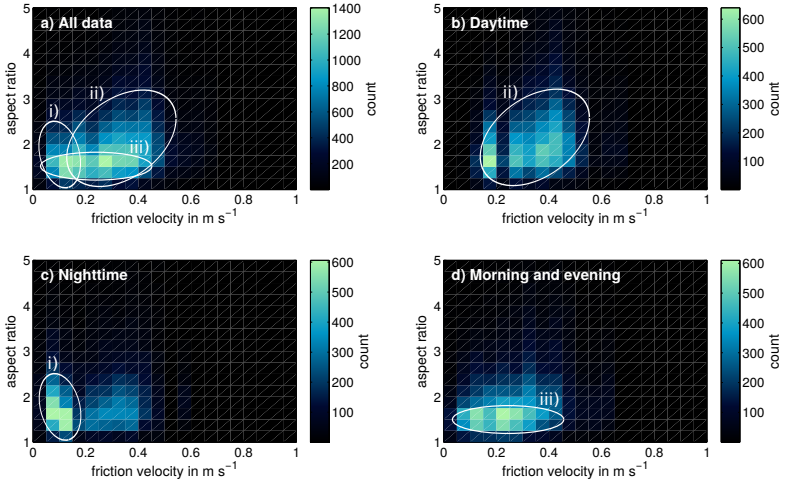

Figure 5.12: Two-dimensional distribution of coherent structures in regards to the aspect ratio and the underlying friction velocity. Ellipses i), ii), and iii) represent areas of interest. a) is based on the whole data set, b) on measurements within daytime, c) within nighttime, and d) within the morning and evening hours.

where large coherent structures strongly depend on buoyancy-driven turbulence instead of shear-induced turbulence. But as the classification in Chapter 4 only qualitatively distinguished between large coherent structures ($\geq$ 1000 m) and small coherent structures ($<$ 1000 m), the quantitative results of Figure 5.11(b) – where the length of the structures seems to be dependent on the friction velocity – shows further characteristics. Within a buoyantly-driven environment, where large coherent structures are able to form, the friction velocity and therefore the prevailing wind conditions seem to be important for the lengths of the structures. This explanation also accounts for the correlation of wind speed and structure length in Figure 5.9(b).

As the length of the coherent structures seems to be affected by the friction velocity, the question arises if the width, respective to the aspect ratio, also shows dependencies. Figure 5.12 shows the two-dimensional distribution of coherent

structure detections regarding the aspect ratio and the underlying friction velocity. Because the distribution in Figure 5.12(a) does not exhibit clear clusters, there might be a chance to find significant ones in the subfigures 5.12(b), (c), and (d). During daytime (Figure 5.12(b)) the majority of the structures are located at moderate friction velocities between $0.2\,\mathrm{m\,s^{-1}}$ and $0.5\,\mathrm{m\,s^{-1}}$ (cluster ii). At higher friction velocities, the structures also exhibit higher aspect ratios ≈ 3; at lower friction velocities, the aspect ratio is lower around values ≈ 2. In Figure 5.12(c), the nocturnal coherent structure detections are mainly clustered at low friction velocities around $0.1\,\mathrm{m\,s^{-1}}$ (cluster i), and are less elongated with aspect ratios between 1.2 and 2.2. Within the morning and evening hours in Figure 5.12(d), the structures show small aspect ratios between 1.2 and 1.7, but over a wider range regarding the friction velocity (cluster iii). The separation of the clusters shows that the aspect ratio behaves differently under different atmospheric conditions. Whereas the lowest aspect ratios occur in the morning and evening hours (cluster iii) – when the boundary layer is often neutrally stratified – during nighttime and during daytime, the aspect ratio exhibits higher values. Especially during daytime, the aspect ratio correlates with the friction velocity, so higher shear corresponds to more elongated coherent structures (cluster ii). The effect of the friction velocity to the elongation in an unstably stratified environment compares to the finding in Figure 5.10(b), where the elongation depends on the wind speed. The friction velocity and the wind speed, respectively, rather affect the length of the structures than their width.

Importance of Buoyant Turbulence

As the results of Figure 5.11 have shown, coherent structures grow in size under the influence of higher friction velocities. Figure 5.12 also exhibits an effect on the elongation. But the friction velocity only seems to be important during daytime in the presence of buoyancy. Therefore it is necessary to collect additional information regarding the presence of buoyancy.
Figure 5.13(a) shows a high number of detections concentrated at negative sen-

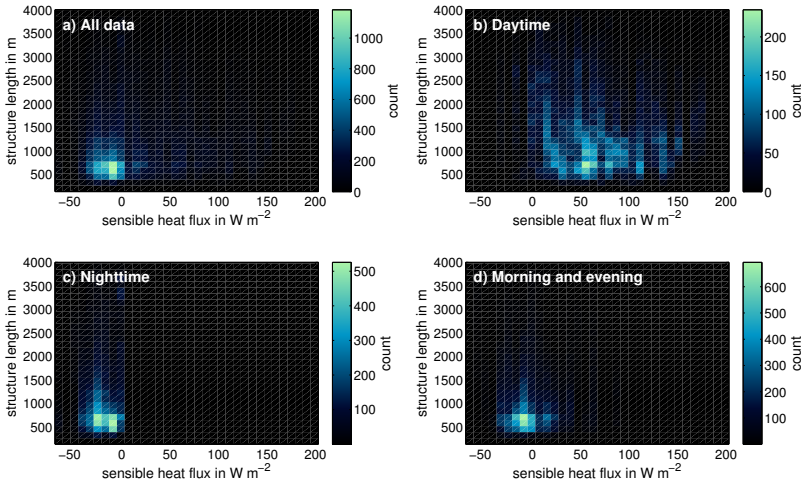

Figure 5.13: Two-dimensional distribution of coherent structures in regards to the structure length and the underlying sensible heat flux. (a) is based on the whole data set, (b) on measurements within daytime, (c) within nighttime, and (d) within the morning and evening hours.

sible heat fluxes between $-40\,\mathrm{W\,m^{-2}}$ and $0\,\mathrm{W\,m^{-2}}$, and with lengths between 300 m and 1000 m. This strong apportionment suppresses the presentability of further clusters. Because during daytime, the sensible heat flux generally exhibits positive values, this distinct cluster only shows up in Figures 5.13(c) and (d), where the buoyant forcing is non-existent or negative, respectively. In the morning and evening (Figures 5.13, d) as well as during nighttime (Figures 5.13, c), coherent structures with lengths $\geq 1000\,\mathrm{m}$ are very rare. During daytime, under the influence of buoyancy the distribution appears to be completely different. With a sensible heat flux between $0\,\mathrm{W\,m^{-2}}$ and $150\,\mathrm{W\,m^{-2}}$, the coherent structures show a wide spread in structure length. Very large coherent structures with lengths $\geq 2000\,\mathrm{m}$ mainly occur under moderate sensible heat fluxes around $50\,\mathrm{W\,m^{-2}}$. At higher sensible heat fluxes, the coherent structures happen to be smaller than 2000 m. The presence of buoyancy on the one hand is necessary for

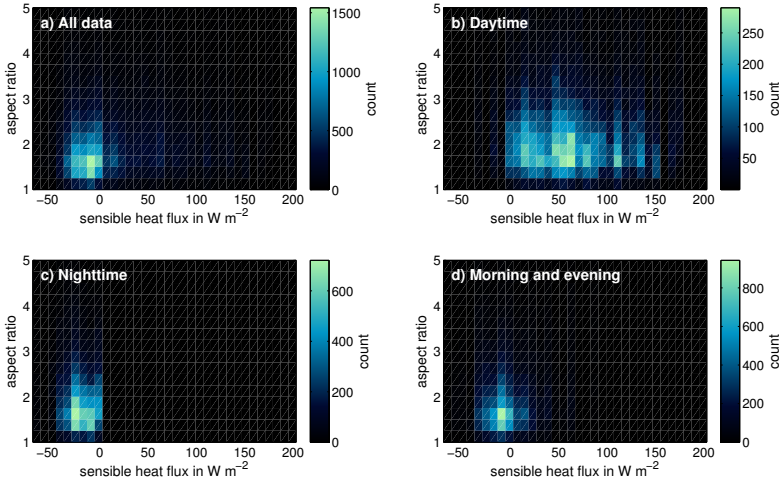

Figure 5.14: Two-dimensional distribution of coherent structures in regards to the aspect ratio and the underlying sensible heat flux. (a) is based on the whole data set, (b) on measurements within daytime, (c) within nighttime, and (d) within the morning and evening hours.

the existence of large coherent structures, but on the other hand, high sensible heat fluxes seem to reduce the length of the structures.

Figure 5.14 represents the two-dimensional histogram in respect to the aspect ratio and the sensible heat flux. The results of this figure show similar results to Figure 5.13. The majority of all detections in Figure 5.14(a) are located at small sensible heat fluxes and at low aspect ratios. This peak refers to detections conducted during nighttime (Figure 5.14, c) and in the morning and evening hours, respectively (Figure 5.14, d). The aspect ratios regarding this cluster vary between 1.2 and 2.5. During daytime (Figure 5.14, d), in the presence of buoyancy, the resulting cluster is less distinct and reveals its highest values (≥ 2.5) at moderate sensible heat fluxes between $0\,\mathrm{W\,m^{-2}}$ and $100\,\mathrm{W\,m^{-2}}$. The aspect ratio decreases at higher sensible heat fluxes to values between 1.5 and 2.5. This figure adds the information that the aspect ratio of coherent structure is affected

by buoyancy in the same way as the length of the coherent structure is, so the elongation of the structure decreases under the effect of strong buoyantly-driven turbulence.

Assessment of Driving Mechanisms

All parameters relevant for the appearance of coherent structures are referred directly to the length and the aspect ratio of the structure. In Chapter 4, especially in Figure 4.13, the dependence of coherent structure shows two relevant driving processes, namely shear and buoyancy. The results of this graphic originates the conclusion displayed in Figure 4.14, where shear is able to generate coherent structures up to a size limited to the size of eddies, which can evolve within the surface layer and the stable boundary layer at nighttime, respectively. In the presence of buoyancy, eddies can gain in size and so do the correspondent coherent structures (Figure 4.13). From this point of view, small coherent structures with a limited size are a feature of a boundary layer with less buoyant influences, e.g. in the nocturnal boundary layer. Under buoyant conditions, coherent structures are able to grow to lengths $\geq 1000\,\mathrm{m}$. The automatic detection method not only provides information on the existence of coherent structures but is also able to quantify their lengths. This raises the ability to look at the length distribution regarding the sensible heat flux and the friction velocity.

Figure 5.15 displays the two-dimensional distribution of detections regarding the friction velocity on the y-axis and the sensible heat flux on the x-axis. In contrast to all prior graphics, this figure displays the median of the structure length on the color scale. The nocturnal detections in Figure 5.15(c) show coherent structures regarding negative sensible heat fluxes distributed from values of $0.0\,\mathrm{m\,s^{-1}}$ to $0.5\,\mathrm{m\,s^{-1}}$ regarding the friction velocity. The median length of all detections in this time period is 959 m (see Table 5.1). In the morning and evening hours (Figure 5.15(d)), clearly the sensible heat flux shows higher values, which influences the distribution regarding the sensible heat flux. The maximum friction velocity increases to $0.6\,\mathrm{m\,s^{-1}}$ and the median structure length decreases to

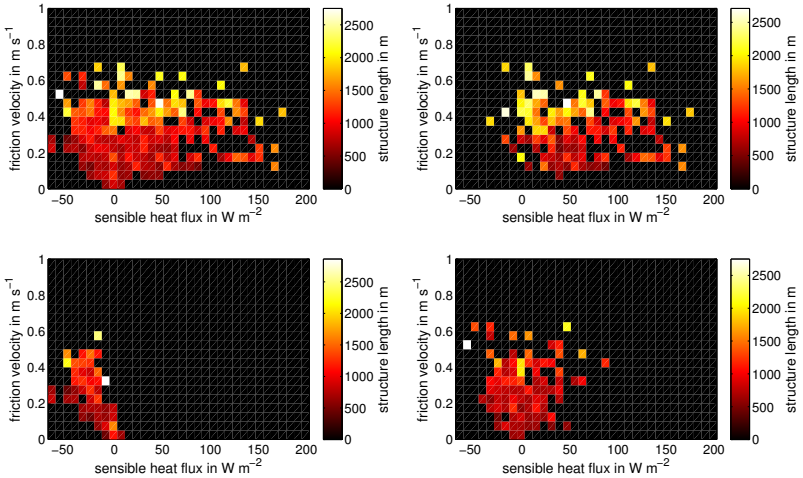

Figure 5.15: Median coherent structure lengths in regards to the sensible heat flux and the friction velocity. (a) is based on the whole data set, (b) on measurements within daytime, (c) within nighttime, and (d) within the morning and evening hours.

883 m. All in all, the structure length distributions compare in both pictures with an increase in structure length from smaller to higher friction velocities. Figure 5.15(b) represents all detections occurring within daytime. The detections are distributed between slightly negative sensible heat fluxes, to maximum sensible heat fluxes of 170 W m^{-2} and between friction velocities from 0.1 m s^{-1} to 0.7 m s^{-1}. The maximum lengths are located at moderate sensible heat fluxes between 0 W m^{-2} and 100 W m^{-2} and at high friction velocities between 0.3 m s^{-1} and 0.7 m s^{-1}. This figure exhibits a connection between structure length and the friction velocity. The same connection emerges in Figure 5.11(b). In accordance to Figure 5.13(b), Figure 5.15(b) indicates that under the influence of a certain friction velocity, the structures at lower sensible heat fluxes between 0 W m^{-2} and 100 W m^{-2} are longer compared to the structures occurring at higher sensible heat fluxes.

Figure 2.3 introduced a conceptual model of how coherent structures are able to form in the atmospheric boundary layer in respect to buoyancy-driven and mechanically-generated turbulence. Figure 4.14 used the results of the classification in Chapter 4 to refine this conception. The length of the structures in a stable and neutrally stratified boundary layer (S^+B^-) depends on the height, affected by shear. As the shear in a stably stratified boundary layer is able to affect higher altitudes compared to a neutrally stratified environment, structures occuring during nighttime often are larger than during the morning and evening hours. Figures 5.5, 5.11, and 5.13 confirm this observation. Furthermore, Figure 4.14 states, that in an unstably stratified boundary layer (S^+B^+) the mechanically-generated, as well as the buoyantly-driven turbulence, affects the appearance of

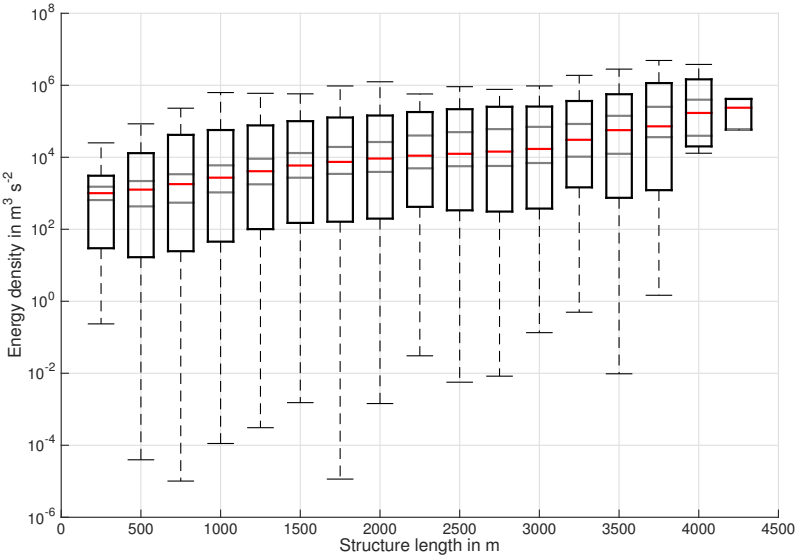

Figure 5.16: Distribution of the energy in regards the coherent structure length. Boxes represent the values between the 5th - and the 95th -percentile, markers represent the median (red), the 25th - and 75th -percentile (grey), and the minimum and maximum (black, outside the box).

coherent structures. Because no quantitative results regarding the length of the structures were available, the exact interaction between both driving mechanisms remained unknown. The automated detection method enables a discussion of quantitative results regarding the length and the elongation of the structures and adds a notion of how the appearance of coherent structures is influenced during $S^{+}B^{+}$-situations.

Figures 5.9(b) and 5.11(b) have shown that under unstable conditions, the wind speed and the friction velocity, correlate with the length of the coherent structures, whereas Figures 5.10(b) and 5.12(b) state that also corresponding to higher wind speeds and higher shear, the structures are more elongated. In contrast to that, Figures 5.13(b) and 5.14(b) show that the length, and also the elongation of the structures decrease when the sensible heat flux increases. On the one hand, when due to high wind speeds, the surface layer during daytime is strongly sheared, the containing eddies have higher intensities than during low wind speed situations. On the other hand, a strongly buoyantly-driven boundary layer produces more intense eddies with the extent of the mixed layer. The buoyantly-induced eddies induce areas of enhanced and reduced wind speeds near the ground. Under medium wind situations, due to a highly sheared boundary layer, shear-induced eddies might be very intense. In a buoyantly-driven boundary layer, coherent structures referring to strong winds appear to be larger compared to coherent structures within low wind situations (Moeng and Sullivan, 1994). Intense eddies transport larger energies and therefore the dissipation lasts longer yielding large coherent structures with higher elongations.

Situations where the buoyantly-driven turbulence is dominant ($B^{++}S^{+}$) refer to structures which are considerably larger than 1 km, but there is no connection between structure length and the buoyant turbulence. In situations with a dominant shear-driven turbulence production ($B^{+}S^{++}$) coherent structures gain in size corresponding to the shear available.

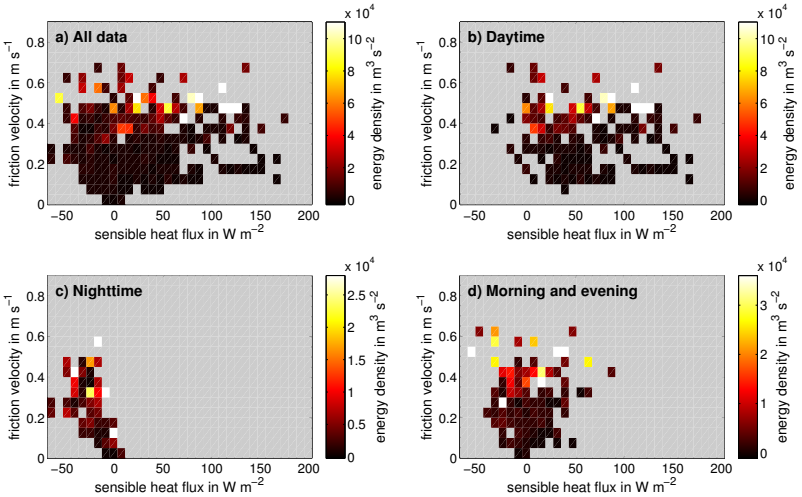

Figure 5.17: Median coherent structure energy in regards to the sensible heat flux and the friction velocity. (a) is based on the whole data set, (b) on measurements within daytime, (c) within nighttime, and (d) within the morning and evening hours.

Energetic Distribution

An estimation of the energy contained in a coherent structure is achievable by using Equation 5.6:

$$E_{\mathrm{CS}} = \overline{v}^2 \cdot L \text{ in } \mathrm{m^3\,s^{-2}}\,, \tag{5.6}$$

where $\overline{v}$ is the mean velocity within the coherent structure and L is the length of the coherent structure. Figure 5.16 presents the distribution of the energy calculated by Equation 5.6, regarding the coherent structure's length. The median shows an increase of energy from about $10^3\,\mathrm{m^3\,s^{-2}}$ at lengths about 500 m to values higher than $10^5\,\mathrm{m^3\,s^{-2}}$ at lengths about 4000 m. As the y-axis is on a logarithmic scale, the energy increases quadratically with the length. This confirms that large coherent structures – which occur under strongly sheared conditions – transport a considerable amount of energy. Figure 5.17 points out the connection

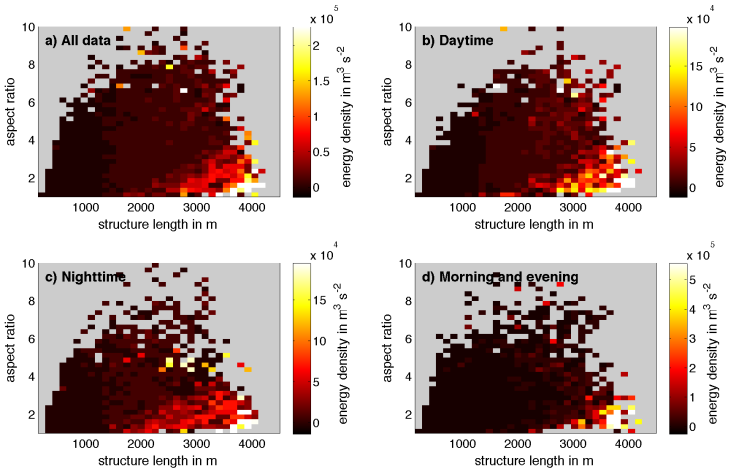

Figure 5.18: Median coherent structure energy in regards to the structure length and the aspect ratio. (a) is based on the whole data set, (b) on measurements within daytime, (c) within nighttime, and (d) within the morning and evening hours.

between the atmospheric driving mechanisms and the energy. The colors denote the median of the energy. All maximum values are located in the upper part of the picture coinciding with high values of friction velocity. Whereas the energy seems to be strongly dependent on the friction velocity, the effect of the sensible heat flux is negligible. As high friction velocities are able to occur throughout the day, high energetic coherent structures are not a feature that only occurs during daytime.

Figure 5.18 shows the energy in dependence to the length of the structures on the x-axis and to the aspect ratio on the y-axis. Figure 5.16 already analysed the influence of the structure length on the energy and stated that the longer the structures are, the higher the energy is. The mean energy increases from left to right, but it decreases in respect to the aspect ratio. This points out that the structures that are also thick with corresponding small aspect ratios contain more energy.

5.3 Summary and Discussion

This chapter showed the implementation of an algorithm able to detect coherent structures within a data set of the horizontal wind field. The methodology is based on three basic algorithms. There is first a) a two-dimensional filtering algorithm, which smooths the edges of the structures and enables b) the application of a threshold detection algorithm. This algorithm assesses in which areas values reach a certain threshold and defines these areas as coherent structures. A two-dimensional three-state matrix is then interpreted by c) a linkage- and clustering algorithm, which processes the matrices and returns parameters of ellipses, which represent the separate coherent structures.

Parameters like the length, the aspect ratio, as well as the energy are analysed in dependence of meteorological parameters, e.g., the sensible heat flux and the friction velocity, which represent the turbulence generated by buoyancy and by shear, respectively. In contrast to Chapter 4, the results of the automated detection algorithm are based on the statistical analysis of coherent structures. For example, the manual characterization method in Chapter 4 only revealed information on whether coherent structures exist within a certain time interval and if they exceed a length of 1 km in mean wind direction. The application of an automated detection method now yields quantitative results. The quantification of these results significantly helps to understand the behaviour of coherent structures in an unstable boundary layer.

Figures 5.5, 5.8, and 5.9 have shown that long coherent structures mainly occur during daytime hours with underlying unstable conditions. This is in perfect accordance to all previous results. The manual characterization (Chapter 4) has revealed that large coherent structures strongly depend on the existence of buoyancy. From what Figure 5.13 reveals, buoyancy is necessary for the existence of large coherent structures, but high buoyancy also suppresses the existence of very large coherent structures. Under neutral and stable conditions, coherent structures are exclusively generated by shear. This is pointed out by all prior analysis. Eddies in a sheared layer are able to grow to a size comparable to the

sheared layer. The length of shear-generated coherent structures is dependent on the size of the eddies, which scale with the height of the shear layer. For this reason, the corresponding coherent structures are relatively restricted regarding the maximum lengths. In contrast to that, up- and downdrafts are able to add a vertical motion to existing shear- generated eddies under unstable conditions. The interaction of both driving mechanisms leads to eddies considerably larger than the surface layer height resulting in larger coherent structures near the ground. Figures 5.9 and 5.11 illustrate how higher wind speeds and therefore higher values of friction velocity significantly correlate with long coherent structures. So maximum lengths are achieved under slightly unstable conditions and high shear-driven turbulence. All this information is combined in Figure 5.15. The median of the structure length increases in dependence to the friction velocity.

The findings of Moeng and Sullivan (1994) have shown, that coherent structures under strong wind situation appear to be larger compared to calm situations. Shear-driven turbulence causes eddies with high intensities, which contain a large energies (Figure 5.17). The dissipation of the energy in the lee of the eddies cause a large area of reduced wind speeds. Therefore large and strongly elongated coherent structures results in the horizontal wind field. In contrast to that, buoyantly-driven eddies, scaling with the mixed layer height, form coherent structures below them. These structures do not contain a large amount of energy (Figure 5.17) and also are considerably smaller, compared to shear-driven coherent structures.

By now the discussion has been restricted to the length of the structures. Calculating the ratio between the length and the width of coherent structures results in the aspect ratio. This ratio not only represents the width, it also stands for the elongation of the structures. The longer and thinner they are, the higher the aspect ratio is. Similar to the length, the aspect ratio increases with respect to the friction velocity, but decreases in dependence to the sensible heat flux. This points out that shear generates streaks that are long compared to their width. In contrast to that, buoyancy leads to coherent structures that are less elongated.

Finally, the estimation of the energy transported by coherent structures is held

out by the calculation of the energy. Figures 5.16 and 5.18 show that an increase in structure length coincides with higher energy densities, whereas higher aspect ratios refer to structures containing less energy. This looks surprising at first, as Figure 5.17 states that high energetic structures refer to shear rather than buoyancy. A possible explanation lies in the calculation of the mean wind velocity of the coherent structures. A one-dimensional wind signal of coherent structures always compares to a ramp-like or sine-signal. In the center of the coherent structures, the values are at a maximum level, whereas they decrease near the edges. A long and thin coherent structure has more values at the edges than in the center, whereas a broader long structure reveals significantly more center values. Therefore, the mean wind speed corresponding to coherent structures with low aspect ratios might show higher values. The quadratic relation between wind speed and energy thus explains why the aspect ratio behaves counter-intuitively.

6 Three-Dimensional Coherent Structures

The application of dual-Doppler lidar methods provides a horizontal wind field data set near to the ground. Chapter 4 and Chapter 5 used the two-dimensional wind field to gather information about the driving mechanisms for the formation of coherent structures and to reveal information on their horizontal appearance. As stated before, it is not feasible to determine the precise vertical extent and the specific vertical characteristics of coherent structures. During the HOPE field campaign, two additional lidar systems recorded information about the vertical extent of coherent structures.

6.1 Method Description

Various studies using in-situ and remote sensing instruments, reveal information about the vertical structure of the atmospheric boundary layer. Some processes within the surface layer and the mixed layer are well-understood, but a complete understanding of turbulent process are not yet achieved. Current information about the three-dimensional shape of coherent structures mostly originates from simulations, but not from measurements. The two- dimensional coherent structure measurements in a huge domain demand a powerful dual-Doppler lidar system. A horizontal dual-Doppler setup does not provide vertical wind information. A triple-Doppler system is able to measure the three-dimensional wind vector, and it is theoretically possible to gain information at several grid points within a three-dimensional space. But the movement of the lidars' scanner is time consuming, which leads to restrictions regarding the temporal and horizontal resolution of the measurements. There is currently no measurement system available that provides three-dimensional measurements within a three- dimensional space

at a horizontal and temporal resolution suitable for coherent structure research. The application of additional lidar systems that support the dual-Doppler measurements is a legitimate compromise for turbulent wind field studies. During the HOPE field campaign, additional Doppler lidars were deployed, as was mentioned in Section 3.2.2. The HALO lidar continuously provides a profile of vertical wind speed near the center of the dual-Doppler data set. The WLS200 lidar was positioned at the northwesterly edge of the horizontal wind field and operated in a regular scan mode, which combines RHI and PPI scans. These one-dimensional measurements provide insights into the three-dimensional wind field surrounding the site.

6.1.1 Vertical Wind Speed Measurements

The measurements of the HALO depict the vertical wind speed above the lidar. Assuming Taylor's hypothesis of frozen turbulence allows researchers to interpret the one- dimensional measurements of vertical wind speed that is advected with the mean wind speed $\overline{u}$ as a two-dimensional data set (Maurer et al., 2015). Therefore, the time spacing Δt of the measurements can be transferred into distances $\Delta x = \overline{u} \cdot \Delta t$. Figure 6.1(a) shows the horizontal wind field obtained from the dual-Doppler retrieval. The red dot numbered 0 indicates the location of the HALO lidar within the domain. Using the mean wind vector of the dual-Doppler retrieval, displayed in the right bottom part of the picture, allows researchers to visualize a cross-section of the vertical wind. Figure 6.1(c) represents the HALO vertical wind measurements for the range of -3 km to 3 km, relative to the HALO lidar at the abscissa, and from 0 km agl to 2 km agl on the ordinate. Negative values indicate downward motions and positive values upward motions. Due to low aerosol concentrations, no measurements above the atmospheric boundary layer were available. Comparing the up- and downdrafts above the structures in the dual-Doppler retrieval indicates anti-correlations between the wind speed fluctuation in mean wind direction u' and the vertical wind speed w'. Chapter

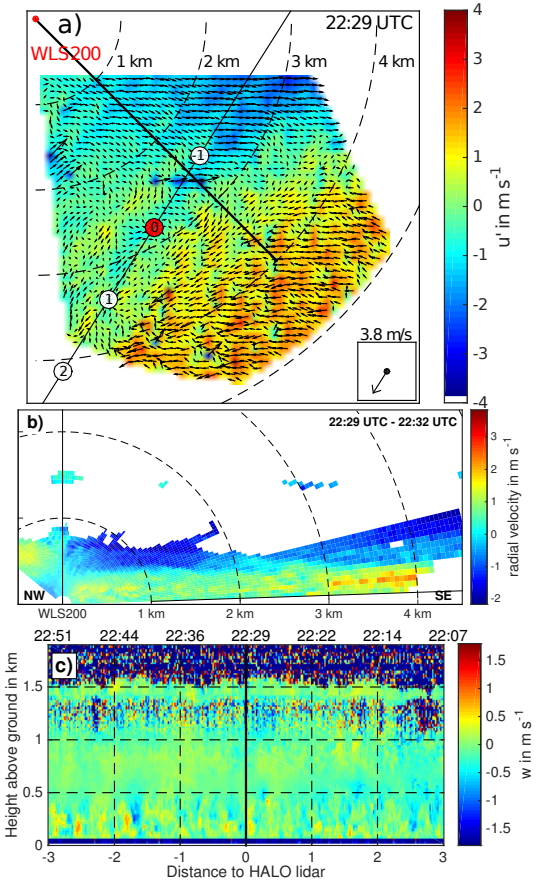

Figure 6.1: Different lidar scans on 5 April 2013. (a) dual-Doppler retrieval measurements at 22:29 UTC. Wind arrows display the two-dimensional flow field. The wind vector in the lower right corner indicates the mean wind speed and direction. (b) RHI scan at the azimuth angle of 135° of WLS200 between 22:29 UTC and 22:32 UTC. The black line in (a) indicates the location of the RHI scan, whereas the black line along the 2° elevation scan in (b) represents the location of the dual-Doppler measurements. (c) vertical HALO measurements between 22:07 UTC and 22:51 UTC, where the abscissa is transformed into distances using Taylor's hypothesis of frozen turbulence. The red dot in (a) marks the location of the HALO lidar and the white dots refer to the distances at the abscissa of (c).

2 introduced an anti-correlation between both values in the framework of the ejection-sweep-pattern.

6.1.2 RHI Measurements

In the upper left edge of Figure 6.1(a), a red dot marks the location of the WLS200 lidar. The black line leading from there to the southeast represents the location of the RHI scan at an angle of 135°. The dashed circles mark the range in kilometers regarding the WLS200 lidar. Within the HOPE campaign, the WLS200 operated in a regular scan mode that provides PPI scans at two different elevations of 5° and 75°; furthermore, the measurements of four RHI scans allow researchers to interpret the surrounding wind field regarding its three-dimensional structure. The RHI scans are conducted at azimuth angles of 0°, 45°, 90°, and 135° and cover elevation angles from 0° to 135° for each scan. However, two of these six scans captured wind information within the domain of the dual-Doppler data set. The PPI, at an elevation angle of 5°, gives an overview of the horizontal wind field. The first example in Figure 6.1(c) shows a nocturnal situation at 22:29 UTC on 5 April, 2013. The turbulence production at this time was exclusively held out by shear ($u_* = 0.13\,\mathrm{m\,s^{-1}}$), as the measured sensible heat flux was $H_0 = -4\,\mathrm{W\,m^{-2}}$. According to the conceptual model in Figure 2.3 and the statistical evaluation in Chapter 4, this situation is characterized as S^-B^-, with no coherent structures to expect. If the mechanically-generated turbulence suffices, low-intensity organization might occur. Figure 6.1(d) displays r-φ-measurements of the radial velocity above the black line within the dual-Doppler domain in 6.1(a). The black solid line at the bottom represents the height of the dual-Doppler retrieval data. Negative radial velocities indicate motions directed towards the lidar, and positive values represent air moving away from the lidar. The maximum range of WLS200 measurements is at distances of 4 km, so the RHI does not cover the complete dual-Doppler data set. In all further images regarding RHI measurements, the range of the colors is adjusted to the mean wind vector in the domain. For that reason, red colors display high values

and blue colors display low values, which are not necessarily positive or negative.

6.2 Vertical Extent of Coherent Structures

This section shows two examples that represent different wind situations. The first example is based on a sequence of three consecutive snapshots in the morning boundary layer between 07:39 UTC to 9:42 UTC on 8 April 2013. This situation shows the development of the mixed layer in the morning and how the length of the coherent structures compares to the increasing mixed layer height. The second example presents a situation with low wind speeds but with a serious buoyancy driving.

6.2.1 Coherent Structures in the Morning Boundary Layer

In the morning of 8 April 2013 at 07:39 UTC, the horizontal wind field (Figure 6.2(a)) shows some small coherent structures organized as streaks. At this time, the atmosphere was considerably affected by medium shear of $u_* = 0.27\,\mathrm{m\,s^{-1}}$ and by medium buoyancy with $H_0 = 41\,\mathrm{W\,m^{-2}}$. from the experience of Section 4.2.2, this situation is categorized as a S^+B^--situation with expected small coherent structures. Since the sensible heat flux is not negligible, buoyancy might have already affected the boundary layer so it is debatable if this situation could also be defined as an S^+B^+-situation. In Figure 6.2(a) some small coherent structures with lengths up to 1 km and widths of about 100 m are present, which are orientated in the mean wind direction. Figure 6.2(c) shows the evolution of the vertical wind speed between 07:28 UTC and 07:50 UTC and between -3 km and 3 km away from the lidar. Above 1.3 km agl, the vertical profile is affected by noise. Near to the ground, vertical mixing processes reaching to heights of 250 m agl indicate that the turbulence already affects height levels above the surface layer, which is caused by buoyancy. With the influence of buoyant turbulence in height levels above the surface layer, this situation now clearly shows characteristics of an S^+B^+ event. Between the mixed layer and residual layer,

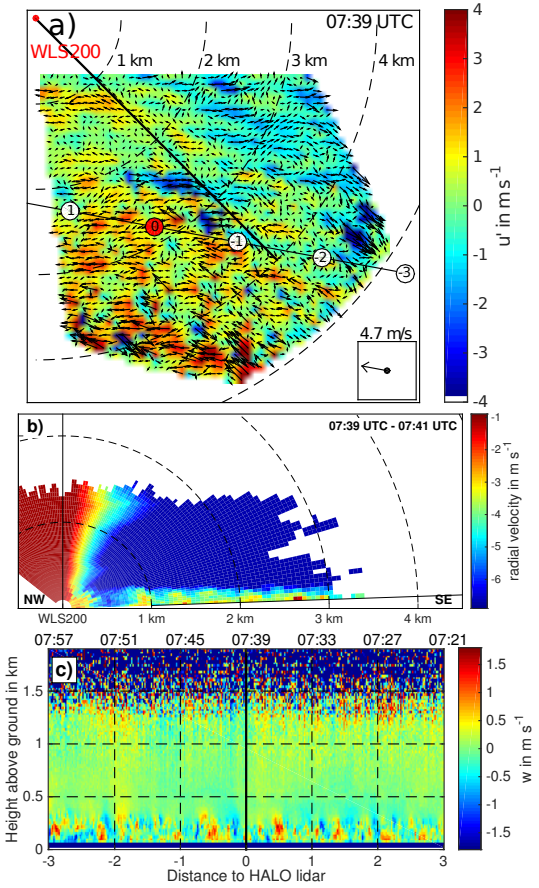

Figure 6.2: Various lidar scans on 8 April, 2013. (a) dual-Doppler retrieval measurements at 07:39 UTC, (b) RHI scan at azimuth angle of 135° of WLS200 between 07:39 UTC and 07:41 UTC. (c) vertical HALO measurements between 07:28 UTC and 07:50 UTC. This diagram compares to Figure 6.1.

no considerable vertical movements are prevalent. Singular coherent structures in Figure 6.2(a) cannot be compared to singular updrafts in Figure 6.2(c), as the accuracy of Taylor's hypothesis of frozen turbulent does not suffice to compare very small elements. Nevertheless, the dimensions of the up- and downdrafts compare to the lengths of the coherent structures, which are several hundred meters long. Furthermore, the up- and downdrafts show some kind of regularity. The major updrafts occur at the locations -0.4 km, 0.5 km, and 1.4 km with a mean spacing of 900 m. The major downdrafts are located at -0.8 km, 0.0 km, and one relatively far away from the other ones at -2.6 km. The first two downdrafts have a spacing of 800 m. These distinct structures fulfill the requirements of spatial and temporal coherence, as well as have the regularity to be defined as coherent structures. Figure 6.2(b) shows the RHI scan capturing the radial velocity within the dual-Doppler measurement domain and is conducted between 07:39 UTC and 07:41 UTC. The considerably negative values of radial velocity originate from the wind moving towards the lidar at medium wind speeds. At altitudes below 250 m agl, the radial velocity exhibits higher values. Here the ground friction affects the flow and reduced the absolute wind speed. The wind speed was not reduced evenly in the whole domain. Areas with higher wind speeds of about $-3.0\,\mathrm{m\,s^{-1}}$ alternate with areas of lower wind speed $-4.5\,\mathrm{m\,s^{-1}}$. The horizontal as well as the vertical extent of these structures of about ≈ 200 m agl compares to the mixed layer height in Figure 6.2(c). Because at low altitudes the RHI measurements are nearly independent from the vertical wind speed, the radial velocity is a wind component that represents the horizontal wind speed and thus compares to u. The regularities in Figure 6.2(b) are not as distinct as in Figure 6.2(c), so interpretations about the spacing and the distances might be misleading, especially because the RHI scan is directed in mean wind direction. But areas with a low radial velocities in Figure 6.2(b) – e.g. at 1.2 km away from the WLS200 – correlate with $u' > 0\,\mathrm{m\,s^{-1}}$ in Figure 6.2(a). Furthermore higher radial velocities correlate with $u' < 0\,\mathrm{m\,s^{-1}}$. Because the air masses move towards the lidar and the color scale is adjusted to the mean wind speed, red colors indicate $u' < 0\,\mathrm{m\,s^{-1}}$ and blue colors indicate $u' > 0\,\mathrm{m\,s^{-1}}$. From that point of

view, the RHI absolutely agrees with the dual-Doppler retrieval. This correlation enables researchers to conclude that horizontal coherent structures also seem to have a vertical structure. As the information on the vertical extent for both additional measurements in Figure 6.2(b) and (c) are similar, up- and downdrafts are also related to horizontal coherent structures. The connection between horizontal coherent structures and vertical wind speed was introduced in Section 2.2.3, where u' and w' exhibit an anticorrelation.

About an hour later, at 08:29 UTC on the same day, higher values of buoyancy ($H_0 = 67\,\mathrm{W\,m^{-2}}$) and increasing wind speeds of $6.9\,\mathrm{m\,s^{-1}}$ are prevalent. With higher values of shear ($u_* = 0.30\,\mathrm{m\,s^{-1}}$), this situation is categorized as S^+B^+, which leads to the expectation of large coherent structures in the site. The dual-Doppler measurements in Figure 6.3(a) clearly shows streaky coherent structures, which are orientated exactly in mean wind direction. These structures show lengths of about 1.5 km to 2.0 km and widths of a few hundred meters. The vertical extent of the boundary layer in Figure 6.3(c) shows some distinct differences to Figure 6.2(c). The up- and downdrafts intensify and gain in height and vertical mixing is carried out within the lowest 500 m of the boundary layer. Except for the updraft located between the 2 km and the 3 km markers, though, the vertical movements ave a very chaotic appearance without any real distinction. As this major updraft region is located outside the dual-Doppler measurement domain, it is not possible to compare these structures to horizontal coherent structures in Figure 6.3(a). Moeng and Sullivan (1994) claim that in a well-mixed boundary layer, the spacing of coherent structures is $3z_i$. This example reveals a similar connection between the height of the mixed layer $z_{\mathrm{ML}} \approx 500\,\mathrm{m}$ and the length of the structures in mean wind direction $l_x \approx 2.0\,\mathrm{km}$. The RHI scan in Figure 6.3(b) shows that the vertical extent of the structures in the surface layer also increases to values of $\approx 450\,\mathrm{m}$, similar to the vertical wind speed measurements in Figure 6.3(c). Hence, the structures seem to cover nearly the entire mixed layer. The structures in Figure 6.3(b) are sufficiently distinct and the horizontal coherent structures in Figure 6.3(a) are big enough to compare both kind of structures. In the RHI in Figure 6.3(b), in a distance of about 1.1 km and from 2.0 km to

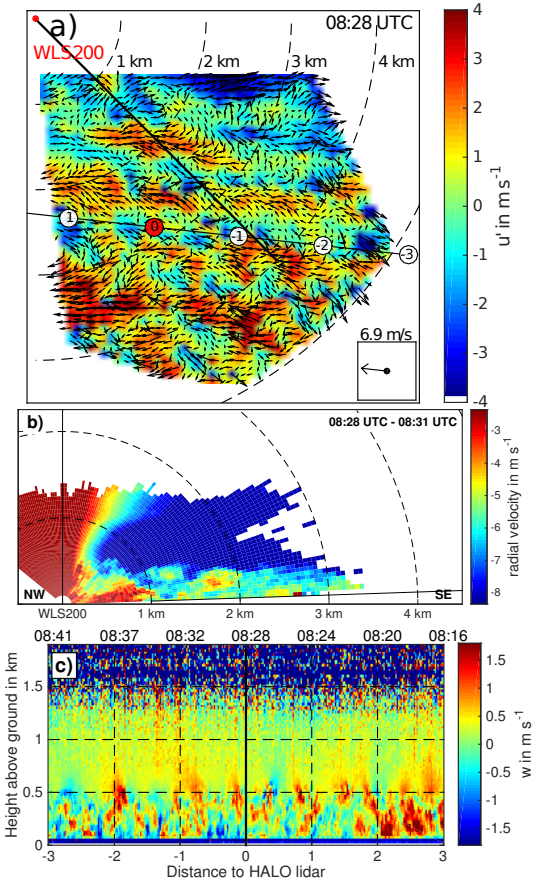

Figure 6.3: Various lidar scans on 8 April, 2013. (a) dual-Doppler retrieval measurements at 08:28 UTC, (b) RHI scan at azimuth angle of 135° of WLS200 between 08:28 UTC and 08:31 UTC. (c) vertical HALO measurements between 08:16 UTC and 08:41 UTC. This diagram compares to Figure 6.1.

2.3 km away from the WLS200, the radial velocity exhibits low values of about $-7\,\mathrm{m\,s^{-1}}$, respectively $-6\,\mathrm{m\,s^{-1}}$. These areas of low radial velocity alternate with regions of relatively increases radial velocities of $-5\,\mathrm{m\,s^{-1}}$ and $-4.5\,\mathrm{m\,s^{-1}}$, located between 1.4 km and 2.0 km and from 2.3 km to 2.7 km away from the WLS200. The corresponding areas in Figure 6.3(a) along the black solid line, show an anticorrelated behaviour. Areas with $u' \approx +3\,\mathrm{m\,s^{-1}}$ are located around 1.1 km and between 1.6 km and 2.2 km away from the WLS200. These small but distinct regions with $u' \approx -1\,\mathrm{m\,s^{-1}}$ can be seen between 1.2 km and 2.0 km and from 2.3 km to 2.7 km away from the WLS200. The RHI scan describes the same structures as in the dual-Doppler measurements.

One hour later at 09:42 UTC, the sensible heat flux again increases further to values of $H_0 = 124\,\mathrm{W\,m^{-2}}$ and at higher wind speeds of $8.3\,\mathrm{m\,s^{-1}}$; the shear also exhibits higher values of $u_* = 0.42\,\mathrm{m\,s^{-1}}$. Under the influence of buoyantly-driven and shear-generated turbulence, this situation is characterized as an S^+B^+-situation and large coherent structures are expected.

The coherent structures in Figure 6.4(a) gained in length, width, and intensity. They are still aligned nearly parallel to the mean wind. The areas with $u' < 0\,\mathrm{m\,s^{-1}}$ exhibits lengths of ≈ 2 km and are partially broader than 500 m. In the middle of the measurement domain, a very dominant area with $u' > 0\,\mathrm{m\,s^{-1}}$ is even longer than ≈ 2 km and about 600 m thick. As the HALO measurements cut through this last-mentioned structure with $u' > 0\,\mathrm{m\,s^{-1}}$, it would have been expected to see a correspondent downdraft region due to the ejection and sweep pattern. Furthermore, some smaller structure occur between -1.0 km to 2.5 km. Generally, in Figure 6.4(b) the up- and downdraft regions reach further to heights above 1 km agl. From -2 km to 2 km, a very dominant downdraft region is prevalent, indicating anticorrelation between u' and w'. From -3 km to -2 km, an updraft reaches to the ground. Some smaller updrafts region with the horizontal extension of a few hundred meters are located at -1.5 km and -0.5 km. All in all, this example confirms the anticorrelation between u' and w'. But, in the area where the smaller structure occur, this anticorrelation is not as obvious as in the middle of distinct structures. Comparing the values of u' from the dual-

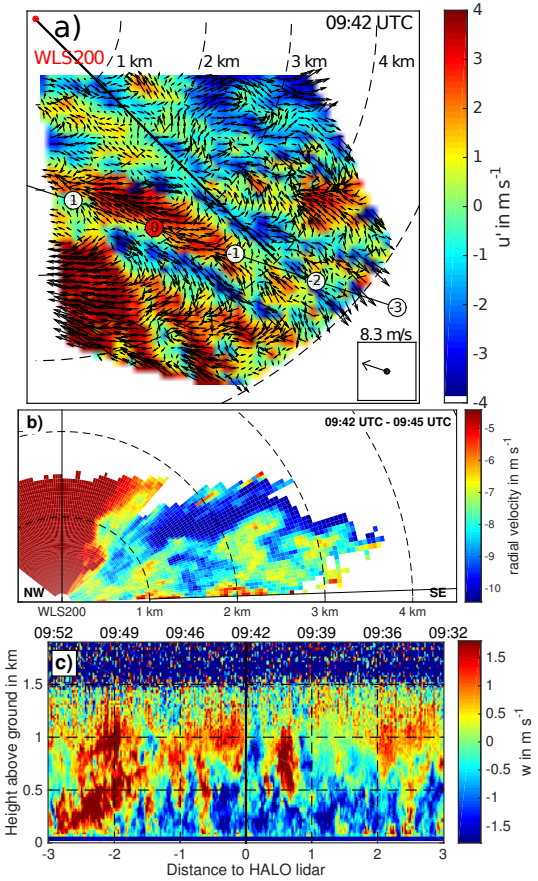

Figure 6.4: Various lidar scans on 8 April 2013. (a) dual-Doppler retrieval measurements at 09:42 UTC, (b) RHI scan at azimuth angle of 135° of WLS200 between 09:42 UTC and 09:45 UTC. (c) vertical HALO measurements between 09:32 UTC and 09:52 UTC. This diagram compares to Figure 6.1.

Doppler retrieval to the RHI radial velocities in Figure 6.4(b) results in some other suggestions regarding the structure formation processes. From 1.0 km to 1.6 km and from 2.0 km to 2.8 km away from the WLS200, negative values of $u' \approx -2.0\,\mathrm{m\,s^{-1}}$ can be found, whereas from 1.9 km to 2.0 km, the fluctuation of the wind speed u' slightly exceeds $0.5\,\mathrm{m\,s^{-1}}$. The radial velocity of the RHI again shows a contrary behaviour. From 0.8 km to 1.3 km and from 1.7 km to 2.3 km away from the WLS200, high values of $\approx -5\,\mathrm{m\,s^{-1}}$, and in between 1.3 km to 1.7 km low values of $\approx -8\,\mathrm{m\,s^{-1}}$ are depicted. There seems to be a bias, but more or less the dimensions compare. These very distinct structures near the ground have a very small vertical extension of about 300 m agl compared to the mixed layer height. At higher altitudes, there are some more structures of alternating higher and lower radial velocity. These structures seem to be torn apart and appear to have smaller intensities than the ones near to the ground. Lin et al. (1996) find, that coherent structures form in the surface layer. During their life-cycle the structures move upwards but stay aligned in the mean wind. The vertical structures in Figure 6.4(b) agree with the findings of Lin et al. (1996).

As the wind speeds are considerably high during this time, there might be a major structure generation by shear as a result of the ground friction. The automated detection method revealed in Section 5.2.2 that shear correlates with the length of the structure in an unstably stratified environment. Especially, as the shear of $u_* = 0.42\,\mathrm{m\,s^{-1}}$is considerably high, the existence of very intense eddies within the surface layer is benefited. Because the surface layer has an extension of ≈ 100 m, the small and very distinct structures around 1 km and 2 km away from the WLS200 are probably shear-generated vortices near the ground. Due to convection, vortices generated in the surface layer might be extended in height and influence the wind speeds at higher altitudes. The mixing processes are held out up to altitudes of about 1.2 km agl, which corresponds to the height of the mixed layer as approximated in Figure 6.4(b).

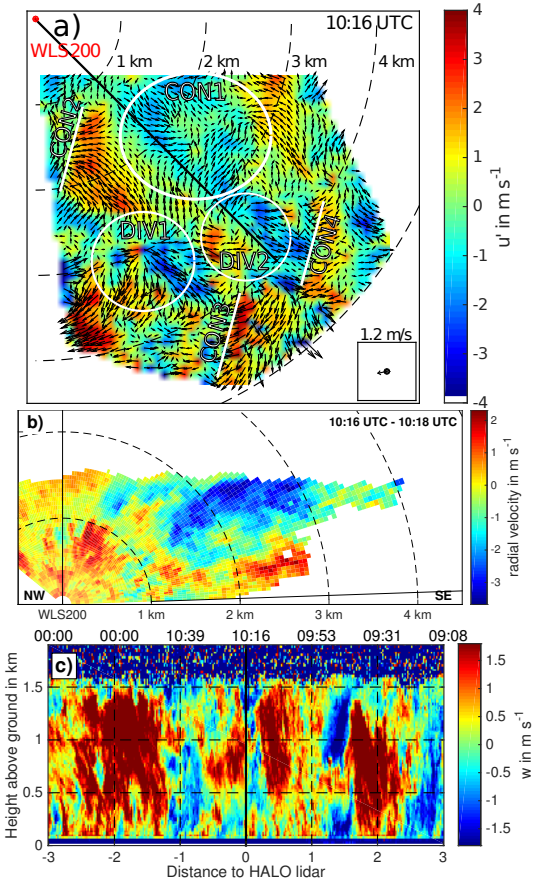

Figure 6.5: Various lidar scans on 7 April, 2013. a) dual-Doppler retrieval measurements at 10:16 UTC, (b)RHI scan at azimuth angle of 135° of WLS200 between 10:16 UTC and 10:18 UTC. (c) vertical HALO measurements between 09:08 UTC and 10:38 UTC. Unlike all previous examples, Taylor's hypothesis of frozen turbulence is not valid here. This diagram compares to Figure 6.1.

6.2.2 Buoyantly-Driven Coherent Structures

On 7 April, 2013 at 10:16 UTC, weak wind speeds of about $1.2\,\mathrm{m\,s^{-1}}$ occur. A sensible heat flux of $H_0 = 139\,\mathrm{W\,m^{-2}}$ and a friction velocity of $u_* = 0.18\,\mathrm{m\,s^{-1}}$ clearly indicate that the turbulence at this time is mainly driven by buoyancy. As the influence of mechanically- generated turbulence is subordinate to the buoyantly-induced turbulence, and because the wind speed is very low at this time, these situations are categorized as an S^-B^+-situation. As previously mentioned in Chapter 2, coherent cellular structures are not expected to appear frequently and only under highly buoyantly-driven atmospheric conditions in calm wind situations. Therefore, these structures are not considered in the manual characterization analysis from Chapter 4.

In Figure 6.5(a), the structures are not aligned as streaks parallel to the mean wind direction. The organization pattern shows patchy areas with different lengths and shapes, and also with reduced and enhanced wind speed. Ellipses and lines illustrate some of the features within this wind field. The white ellipses DIV1 and DIV2 represent areas where, according to the flow visualization, the flow diverges. The green ellipse CON1 represents an area where the flow is converging. The lines CON2, CON3, and CON4 represent lines where the field converges. Assuming the horizontal structures in this example are dependent on up- and downdrafts, the analysis of Figure 6.5(c) would be essential. In contrast to prior analysis within a calm wind situation, though, it is not valid to assume Taylor's hypothesis of frozen turbulence. However, Figure 6.5(c) shows that during this situation major up- and downdrafts reached up to heights of about 1.6 km agl and probably affected the horizontal wind field. It is unfortunate that the single structures cannot refer to single up- and downdrafts. The RHI in Figure 6.5(b) indicates turbulence reaching up to the boundary layer height of about 1.6 km agl. In general, the RHI scan agrees with the dual- Doppler retrieval wind field in Figure 6.5(a); for example, around 2 km away from the 07:39 UTC to 9:42 UTC WLS200, the wind comes from the north-westerly direction and manifests as positive radial velocities in the RHI scan. But Figure 6.5(b) hardly shows any

information about the vertical shape of the structures.
The prior figures have focused on coherent structures aligned as streaks in the wind field. Cellular structures as described by Feingold et al. (2010) have not yet been measured. The measurements from 7 April 2013 look quite promising. Throughout the time from 10:00 UTC to 14:00 UTC, many areas with diverging and converging wind fields are present. This example illustrates that coherent structure in a buoyantly-driven environment strongly depend on up- and downward air motions. The height of the structures in Figure 6.5(b) compares to the height of the boundary layer. The horizontal wind field shows large areas of divergence and convergence, probably corresponding to up- and downdrafts within the site.

6.3 Summary and Conclusion

This study introduces lidar measurements, which are able to show the vertical shape and the extent of horizontal coherent structures. The first example, from 5 April 2013 at 22:29 UTC, has shown that low-intensity structures within an $S^{-}B^{-}$-situation refer to turbulence that is only driven by minor shear. All scans show weakly developed structures reaching to heights of about 400 m agl and refer to the height level influenced by shear. The development of coherent structures in the morning of 8 April 2013, between 07:39 UTC to 9:42 UTC, shows how the atmospheric boundary layer gains in size and the horizontal structures also gain in length. The first image (Figure 6.2) presents small streak-like coherent structures with lengths of about 1 km within an $S^{+}B^{-}$-situation. These streaks are aligned in the mean wind direction and the structures occur within the whole shear-induced layer, which reaches to heights of about 250 m agl. The vertically staring HALO lidar, as well as the RHI scan of the WLS200, show that the structures, as well as the up- and downdrafts, have a horizontal spacing between 800 m and 900 m. Moeng and Sullivan (1994) claim that in a well-mixed boundary layer, coherent structures have a spacing of $3z_i$. This example provides information that demonstrates how small coherent structures in a shear-driven

boundary layer exhibit a similar spacing. The structure spacing is approximately three times larger than the shear-driven layer. One hour later (Figure 6.3), the buoyantly-driven turbulence increases considerably (S^+B^+-situation). Thermals reach to heights of about 500 m agl and the horizontal streaks also gain in size. The majority of the structures in the domain have a length between 1.5 km and 2.0 km in the mean wind direction. Due to higher buoyantly-driven turbulence, at 9:42 UTC the thermals cover the whole height of the well-mixed boundary layer (S^+B^+-situation). The streaks are aligned in the mean wind direction and exhibit lengths between 2 km and 3 km. Furthermore, this example confirms results of Lin et al. (1996), where coherent structures form in the surface layer due to shear-driven turbulence. During their life-cycle the coherent structures move upwards. Figure 6.4(b) shows that very intense structures can be found within the lowest 200 m agl. Above that level the structures are torn apart and less intense.
So far the vertical shape of structures within situations with S^-B^-, S^+B^-, and S^-B^+ have been analysed. Figure 6.5 shows the most promising picture to investigate a situation with dominant buoyant turbulence (S^-B^+). The horizontal wind field shows areas with converging and diverging patterns, the vertical measurements also show up- and downdrafts. Due to the low wind speeds, Taylor's hypothesis of frozen turbulence is not valid and therefore the vertical measurements cannot be transferred to horizontal locations within the dual-Doppler domain. Additionally, the RHI scan does not reveal the vertical shape of the horizontal coherent structures. In the lack of vertical measurements, the existence of cellular structures as illustrated by Feingold et al. (2010) can neither be proven nor disproven. But this example illustrates how a situation dominated by buoyancy form structures with the longest dimension in vertical direction. This also agrees with the findings of Section 5.2.2, where buoyant situation do not coincide with large structures lengths.

7 Summary and Conclusions

In the scope of this thesis the development of a dual-Doppler scan algorithm yielded a horizontal wind field data set with a temporal resolution of 12 s and a horizontal resolution of 60 m within a domain of 10 km^2 (Chapter 3). Measurements were gathered during the HOPE field campaign in Jülich, Germany in April and May 2013. 320 hours of measurement data under various meteorological conditions allow to analyse coherent structures within the atmospheric boundary layer from different perspectives.

Many researchers have intensively studied the existence of coherent structures. Drobinski et al. (1998) use Doppler lidar measurements as well as in-situ measurements to analyse coherent structures stating that the formation of coherent structures depends on both buoyantly-driven turbulence and shear-generated turbulence. Barthlott et al. (2007) and Thomas and Foken (2005) utilize in-situ measurement to show that an unstably stratified boundary layer tends to form elongated coherent structures. Using LES model simulations, Lin et al. (1996) are able to show that coherent structures form in the surface layer and move upwards during their life-cycle. Furthermore, Lin et al. (1997) find that the strength of the coherent structures depends on the surface roughness. Young et al. (2002) review studies related to coherent structures and emphasize the importance of shear-generated, respectively buoyantly-driven turbulence as important mechanisms for the formation of coherent structures.

In the horizontal wind field coherent structures manifest as enclosed regions of enhanced and reduced wind speed in an alternating manner. The development of a conceptual model in Section 2.2.3 helps characterizing coherent structures with

regards to the driving mechanisms of shear and buoyancy. Assuming that coherent structures are caused by eddies within the boundary layer leads to the explanation of many features of coherent structures, e.g. the characteristic ejection- and sweep pattern (Section 2.2.3). The friction of the earth's surface induces mechanically generated turbulence to the air masses. In the surface layer, which is around 100 m high, the horizontal wind speed increases logarithmically with height. A sufficient amount of shear is able to form, respectively maintaining eddies in the surface layer. These eddies influence the wind speed near the ground. Eddies moving with the mean wind cause a relative reduction and thus reduce the horizontal wind speed relative to the mean flow. An increase of buoyantly-driven turbulence forces air masses to rise. Thermals induced by buoyancy reach to the mixed layer during daytime and cause mixing processes above the surface layer. Under the influence of buoyantly-driven turbulence, eddies are able to exceed the height of the surface layer considerably. Eddies with a greater extension cover a larger spatial domain and therefore the coherent structures also gain in size. For this reason it is expected that coherent structures under the influence of buoyantly-driven turbulence are significantly larger than exclusively shear-driven coherent structures. In the absence of shear, coherent structures relate to up- and downdrafts and Khanna and Brasseur (1998) as well as Feingold et al. (2010) expect cellular coherent structures with a hexagonal horizontal shape. These structures compare to Rayleigh-Bénard cellular pattern and are characterized by weak updraft regions surrounded by stronger but thinner regions of downdrafts, respectively weak downdraft regions surrounded by stronger but thinner regions of updrafts.

The application of a manual characterization method (Chapter 4) allows to classify the whole data set in terms of the containing coherent structures. The characterization scheme is designed to distinguish between events with large coherent structures (≥ 1 km), small coherent structures (< 1 km), patterns in the horizontal wind field which exhibit organization on a low intensity (low-intensity events), and events with no containing coherent structures. Every ten-minute time inter-

val is assessed regarding these four classes, resulting in a data set representing coherent structures with respect to their appearance. Comparing the data set to the friction velocity u_* determines how shear and mechanically generated turbulence affects the appearance and the occurrence of coherent structures, respectively. The buoyantly-driven turbulence is represented by the sensible heat flux H_0 comparisons to the classification data show that events with no containing coherent structures take place when $H_0 \leq 0\,\mathrm{W\,m^{-2}}$ and $u_* \leq 0.2\,\mathrm{m\,s^{-1}}$. Fifty-two percent of all nocturnal events represent homogeneous wind fields with no containing structures. In contrast to that, large coherent structures occur when $H_0 > 70\,\mathrm{W\,m^{-2}}$. Generally, large coherent structures are a dominant feature of the atmospheric boundary layer during daytime (49 % of all events). Low-intensity turbulence occurs at nighttime and in the morning and evening hours. Small coherent structures also occur mostly during nighttime and in the evening and morning hours, but also are a feature of the boundary layer at daytime. Small coherent structures appear in 23 % of all nocturnal cases. These results agree with the conceptual model describing the driving mechanisms. Homogeneous events take place in the absence of buoyancy and shear. An increase in shear leads to low-intensity turbulence and small coherent structures. These organization patterns are able to occur during nighttime, when eddies form due to shear within the nocturnal stable boundary layer and in the morning and the evening hours, when the boundary layer is neutrally stratified. Under neutral conditions, shear is restricted to the surface layer. Therefore structures in the morning and evening hours are less distinct with regards to their intensity and horizontal extent. For this reason, low-intensity organization patterns are a dominant feature in the morning and evening. During daytime, when the boundary layer is dominated by buoyantly-driven turbulence, coherent structures are considerably larger. These results are in accordance to the findings of Thomas and Foken (2005) and Barthlott et al. (2007) stating that the length and also the elongation of coherent structures depend on an unstably stratified boundary layer.

As the manual characterization classifies coherent structures in a subjective way,

an independent analysis demands an objective analysis of the data set. An automated detection method (Chapter 5) is able to automatically detect coherent structures in the horizontal wind field data set. The method is threshold-based and represents coherent structures as ellipses. The characteristics of the ellipses – their length, width, and aspect ratio – can be analysed regarding the underlying meteorological conditions. Many results confirm the findings of the manual characterization. Large coherent structures ($\geq 1000\,\mathrm{m}$) mainly occur during the daytime hours, whereas during nighttime coherent structures are considerably smaller. Especially during the morning and evening hours many very small coherent structures are detected ($\approx 600\,\mathrm{m}$). Whereas during daytime buoyancy is able to form eddies with the extent of the mixed layer, during nighttime eddies are generated within the nocturnal, stable boundary layer and thus are considerably smaller. Within the morning and evening hours shear is only available in the surface layer yielding very small structures, defined as low-intensity turbulence. The automated detection method enables discussions regarding quantitative values of the length of the coherent structures. Therefore the dependence of the length to atmospheric parameters is feasible. The lengths of the detected coherent structures do not correlate with H_0. Coherent structures exhibit maximum horizontal extent and elongation when $50\,\mathrm{W\,m^{-2}} \leq H_0 < 80\,\mathrm{W\,m^{-2}}$. In contrast to the influence of buoyantly-driven turbulence, shear-induced turbulence provides for longer coherent structures. The structure length, as well as the aspect ratio, strongly correlates with the friction velocity. This analysis shows that large coherent structures depend on buoyantly-driven turbulence, but a huge amount of buoyancy does not provide for very large structures. A higher amount of mechanically generated turbulence accounts for longer coherent structures. A possible explanation for this behaviour originates in considerations regarding the amount of shear available. Within a strongly sheared surface layer very intense eddies are able to form. Intense eddies contain a significant amount of energy. Analysis regarding the energy transported by coherent structures show, that the energy correlates with the friction velocity u_* and not with the sensible heat flux H_0. Eddies in the mean flow dissipate their energy in leeward direction. Intense eddies affect

a larger area compared to less-intense ones. Therefore the shear – which correlates with the transported energy – causes longer and more elongated coherent structures with reduced wind speed.

A three-dimensional examination of coherent structures leads to another perspective. All prior results describe horizontal coherent structures with regards to their characteristics and formation processes. Chapter 6 uses additional lidar systems to gain information about the vertical extent of coherent structures. A vertically staring Doppler lidar (HALO) within the dual-Doppler measurement domain, and a lidar performing an RHI scan (WLS200) resolving coherent structures in three dimensions. This analysis presents two case studies: one illustrates the development of the boundary layer in the morning, affecting the coherent structure's appearance. When buoyancy is less prevalent and the structures are mainly dependent on wind shear, coherent structures are relatively small ($\approx 500\,\mathrm{m}$). With an increase in buoyancy-induced turbulence, the thermals rise above the surface layer and the coherent structures considerably gain in size ($\approx 1000\,\mathrm{m}$). In a well-mixed boundary layer, the thermals reach the boundary layer height; due to larger eddies, coherent structures reach lengths $\geq 2000\,\mathrm{m}$. During this development the boundary layer is also affected by a huge amount of shear. This example also shows that in the presence of buoyancy coherent structures are able to form in the surface layer. Distinct and strong turbulences occur up to heights of a few hundred meters. In contrast to that, coherent structures in the mixed layer are less intense and seem to be torn apart. Lin et al. (1996) postulate that coherent structures are generated in the surface layer and move upwards during their life-cycle. The RHI scan seems to be feasible to capture this formation process in the framework of a case study. The second case study is related to atmospheric conditions with dominant buoyant forcing. A calm wind situation with high sensible heat fluxes exhibits areas with converging and diverging horizontal winds. The structures have a horizontal extent of $\approx 1.3\,\mathrm{km}$. The vertically staring HALO lidar observed strong up- and downdrafts, probably related to the horizontal structures. Even if an explicit assignment of each particular structure

is not possible, this example illustrates that buoyantly-driven coherent structures rather gain in depth than in horizontal extent. These results support the findings of the automated detection method: the horizontal extent does not correlate with the sensible heat flux. In the absence of shear, very large coherent structures rarely form.

Using three complementary methods to analyse the wind field during the HOPE field campaign yielded a conceptual model explaining coherent structures in the atmospheric boundary layer. In the presence of buoyancy during daytime, coherent structures with sizes ≥ 1000 m are able to form and considerably gain in size under the influence of shear. During shear-driven nighttime situations, intense but significantly smaller structures are present. In the morning and evening hours, structures with low intensities appear very frequently. Shear enables the formation of elongated streak-like coherent structures aligned parallel to the mean wind, whereas under buoyantly-driven conditions the horizontal wind field includes areas with converging and diverging flows – probably related to up- and downdrafts.

This thesis characterizes coherent structures in the horizontal wind field and identifies triggering mechanisms of coherent structure formation. The development of a characterization method describing coherent structures with regards to their intensity and their horizontal extent allows to compare coherent structures to the underlying meteorological conditions. Conclusions can be drawn that the formation of coherent structures depends on buoyantly-driven turbulence as well as mechanically-generated turbulence. All analysis support the notion of a conceptual model summarizing coherent structure formation processes within the atmospheric boundary layer. Mechanically-driven coherent structures are generated by eddies occurring in the lowest part of the boundary layer due to wind shear. In an unstably, respectively neutrally stratified boundary layer, shear occurs within the surface layer, whereas an unstably stratified boundary layer often provides shear also at higher altitudes. During daytime buoyancy is able to form

eddies with the size of the mixed layer, which are considerably larger. These results suggest that the length of coherent structures depends on the size of the corresponding eddies. Therefore the appearance of coherent structures underlie a diurnal cycle. The characteristics of the coherent structures enable parametrizations for further studies and helps to distinguish between different types of coherent structures.

Bibliography

Adrian, R., Meinhart, C., and Tomkins, C. (2000). Vortex organization in the outer region of the turbulent boundary layer. *J. Fluid. Mech.*, 422:1–54.

Adrian, R. J. (2007). Hairpin vortex organization in wall turbulence. *Phys. Fluids*, 19(4):041301.

Balaji, V., Redelsperger, J., and Klaassen, G. (1993). Mechanisms for the mesoscale organization of tropical cloud clusters in GATE Phase III. Part I. Shallow cloud bands. *J. Atmos. Sci.*, 50(21):3571–3589.

Banta, R., Newsom, R., Lundquist, J., Pichugina, Y., Coulter, R., and Mahrt, L. (2002). Nocturnal low-level jet characteristics over Kansas during CASES-99. *Bound.-Lay. Meteorol.*, 105(2):221–252.

Barthlott, C., Drobinski, P., Fesquet, C., Dubos, T., and Pietras, C. (2007). Long-term study of coherent structures in the atmospheric surface layer. *Bound.-Lay. Meteorol.*, 125(1):1–24.

Bergström, H. and Högström, U. (1989). Turbulent exchange above a pine forest II. Organized structures. *Bound.-Lay. Meteorol.*, 49(3):231–263.

Browning, K. and Wexler, R. (1968). The determination of kinematic properties of a wind field using Doppler radar. *J. Appl. Meteorol.*, 7(1):105–113.

Calhoun, R., Heap, R., Princevac, M., Newsom, R., Fernando, H., and Ligon, D. (2006). Virtual towers using coherent Doppler lidar during the Joint Urban 2003 dispersion experiment. *J. Appl. Meteorol.*, 45(8):1116–1126.

Choukulkar, A., Calhoun, R., Billings, B., and Doyle, J. D. (2012). A modified optimal interpolation technique for vector retrieval for coherent Doppler lidar. *IEEE Geosci. Remote. S.*, 9(6):1132–1136.

Collineau, S. and Brunet, Y. (1993). Detection of turbulent coherent motions in a forest canopy part I: wavelet analysis. *Bound.-Lay. Meteorol.*, 65(4):357–379.

Damian, T., Wieser, A., Träumner, K., Corsmeier, U., and Kottmeier, C. (2014). Nocturnal low-level jet evolution in a broad valley observed by dual Doppler lidar. *Meteor. Z.*, 23(3):305–313.

Deardorff, J. (1983). A multi-limit mixed-layer entrainment formulation. *J. Phys. Oceanogr.*, 13(6):988–1002.

Demtröder, W. (2010). *Experimentalphysik 3 Atome, Moleküle und Festkörper*. Springer Berlin Heidelberg New York.

Doms, G., Förstner, J., Heise, E., Herzog, H., Mironov, D., Raschendorfer, M., Reinhardt, T., Ritter, B., Schrodin, R., Schulz, J.-P., et al. (2011). A description of the nonhydrostatic regional COSMO model. *Part II: Physical Parameterization. Tech. rep., Consortium for Small-Scale Modeling*.

Drobinski, P., Carlotti, P., Newsom, R. K., Banta, R. M., Foster, R. C., and Redelsperger, J.-L. (2004). The structure of the near-neutral atmospheric surface layer. *J. Atmos. Sci.*, 61(6):699–714.

Drobinski, P., Flamant, P. H., Pelon, J., et al. (1998). Evidence of organized large eddies by ground-based Doppler lidar, sonic anemometer and sodar. *Bound.-Lay. Meteorol.*, 88(3):343–361.

Drobinski, P. and Foster, R. C. (2003). On the origin of near-surface streaks in the neutrally-stratified planetary boundary layer. *Bound.-Lay. Meteorol.*, 108(2):247–256.

Eder, F., Schmidt, M., Damian, T., Träumner, K., and Mauder, M. (2015). Mesoscale eddies affect near-surface turbulent exchange: Evidence from lidar and tower measurements. *J. Appl. Meteorol.*, 54(1):189–206.

Feingold, G., Koren, I., Wang, H., Xue, H., and Brewer, W. A. (2010). Precipitation-generated oscillations in open cellular cloud fields. *Nature*, 466(7308):849–852.

Fried, D. (1967). Optical heterodyne detection of an atmospherically distorted signal wave front. *Proc. IEEE*, 55(1):57–77.

Garratt, J. R. (1994). *The atmospheric boundary layer*. XVIII ed. Cambridge University Press Cambridge.

Grant, H. (1958). The large eddies of turbulent motion. *J. Fluid. Mech.*, 4(02):149–190.

Grund, C. J., Banta, R. M., George, J. L., Howell, J. N., Post, M. J., Richter, R. A., and Weickmann, A. M. (2001). High-resolution Doppler lidar for boundary layer and cloud research. *J. Atmos. Ocean. Tech.*, 18(3):376–393.

Halliday, D., Resnick, R., and Walker, J. (2009). *Physik*. 2., überarb. und erg. Aufl. Wiley-VCH Weinheim.

Head, M. and Bandyopadhyay, P. (1981). New aspects of turbulent boundary-layer structure. *J. Fluid. Mech.*, 107:297–338.

Hellsten, A. and Zilitinkevich, S. (2013). Role of convective structures and background turbulence in the dry convective boundary layer. *Bound.-Lay. Meteorol.*, 149(3):323–353.

Hussain, A. F. (1983). Coherent structures – reality and myth. *Phys. Fluids*, 26(10):2816–2850.

Inagaki, A. and Kanda, M. (2010). Organized structure of active turbulence over an array of cubes within the logarithmic layer of atmospheric flow. *Bound.-Lay. Meteorol.*, 135(2):209–228.

Iwai, H., Ishii, S., Tsunematsu, N., Mizutani, K., Murayama, Y., Itabe, T., Yamada, I., Matayoshi, N., Matsushima, D., Weiming, S., et al. (2008). Dual-Doppler lidar observation of horizontal convective rolls and near-surface streaks. *Geophys. Res. Lett.*, 35(14):L14808.

Johnson, S. C. (1967). Hierarchical clustering schemes. *Psychometrika*, 32(3):241–254.

Kalthoff, N., Adler, B., Wieser, A., Kohler, M., Träumner, K., Handwerker, J., Corsmeier, U., Khodayar, S., Lambert, D., Kopmann, A., et al. (2013). KITcube - a mobile observation platform for convection studies deployed during HyMeX. *Meteor. Z.*, 22(6):633–647.

Khanna, S. and Brasseur, J. G. (1998). Three-dimensional buoyancy-and shear-induced local structure of the atmospheric boundary layer. *J. Atmos. Sci.*, 55(5):710–743.

Kim, S.-W. and Park, S.-U. (2003). Coherent structures near the surface in a strongly sheared convective boundary layer generated by large-eddy simulation. *Bound.-Lay. Meteorol.*, 106(1):35–60.

Kline, S., Reynolds, W., Schraub, F., and Runstadler, P. (1967). The structure of turbulent boundary layers. *J. Fluid. Mech.*, 30(04):741–773.

Kolmogorov, A. N. (1941). Dissipation of energy in locally isotropic turbulence. In *Dokl. Akad. Nauk SSSR*, volume 32, pages 19–21.

Kottmeier, C. (1982). *Die Vertikalstruktur nächtlicher Grenzschichtstrahlströme*. Institut für Meteorologie und Klimatologie der Universität Hannover.

LeMone, M. A. and Meitin, R. J. (1984). Three examples of fair-weather mesoscale boundary-layer convection in the tropics. *Mon. Weather Rev.*, 112(10):1985–1998.

LeMone, M. A. and Pennell, W. T. (1976). The relationship of trade wind cumulus distribution to subcloud layer fluxes and structure. *Mon. Weather Rev.*, 104(5):524–539.

Lin, C.-L., McWilliams, J. C., Moeng, C.-H., and Sullivan, P. P. (1996). Coherent structures and dynamics in a neutrally stratified planetary boundary layer flow. *Phys. Fluids*, 8(10):2626–2639.

Lin, C.-L., Moeng, C.-H., Sullivan, P. P., and McWilliams, J. C. (1997). The effect of surface roughness on flow structures in a neutrally stratified planetary boundary layer flow. *Phys. Fluids*, 9(11):3235–3249.

Mann, J., Cariou, J.-P., Courtney, M. S., Parmentier, R., Mikkelsen, T., Wagner, R., Lindelöw, P., Sjöholm, M., and Enevoldsen, K. (2008). Comparison of 3D turbulence measurements using three staring wind lidars and a sonic anemometer. In *IOP Conference Series: Earth and Environmental Science*, volume 1, page 012012. IOP Publishing.

Maurer, V., Kalthoff, N., Wieser, A., Kohler, M., and Mauder, M. (2015). Observed spatial variability of boundary-layer turbulence over flat, heterogeneous terrain. *Atmos. Chem. Phys. Discuss.*, 15(13):18011–18064.

Meschede, D. (2010). *Gerthsen Physik*. 24. überarb. Aufl. Springer Berlin Heidelberg New York.

Moeng, C.-H. and Sullivan, P. P. (1994). A comparison of shear-and buoyancy-driven planetary boundary layer flows. *J. Atmos. Sci.*, 51(7):999–1022.

Müller, D., Etling, D., Kottmeier, C., and Roth, R. (1985). On the occurrence of cloud streets over northern Germany. *Q. J. R. Meteorol. Soc.*, 111(469):761–772.

Newsom, R., Calhoun, R., Ligon, D., and Allwine, J. (2008). Linearly organized turbulence structures observed over a suburban area by dual-Doppler lidar. *Bound.-Lay. Meteorol.*, 127(1):111–130.

Newsom, R. K., Ligon, D., Calhoun, R., Heap, R., Cregan, E., and Princevac, M. (2005). Retrieval of microscale wind and temperature fields from single-and dual-Doppler lidar data. *J. Appl. Meteorol.*, 44(9):1324–1345.

Oke, T. R. (1993). *Boundary layer climates*. 2. ed. Routledge London.

Pichugina, Y. L., Banta, R., Kelley, N., Sandberg, S., Machol, J., and Brewer, W. (2004). Nocturnal low-level jet characteristics over southern Colorado. In *Preprints, 16th Symp. On Boundary Layers and Turbulence, Portland, ME, American Meteorological Society, CD-ROM*, volume 4.

Prandtl, L., Oswatitsch, K., and Wieghardt, K. (1990). *Führer durch die Strömungslehre*. 9. Aufl. Vieweg Braunschweig.

Raasch, S. and Schröter, M. (2001). PALM–a large-eddy simulation model performing on massively parallel computers. *Meteor. Z.*, 10(5):363–372.

Rayleigh, L. (1916). On convection currents in a horizontal layer of fluid, when the higher temperature is on the under side. *Philos. Mag.*, 32(192):529–546.

Richardson, L. F. (2007). *Weather prediction by numerical process*. 2. ed. Cambridge University Press Cambridge.

Robinson, S. K. (1991). Coherent motions in the turbulent boundary layer. *Ann. Rev. Fluid Mech.*, 23(1):601–639.

Röhner, L. and Träumner, K. (2013). Aspects of convective boundary layer turbulence measured by a dual-Doppler lidar system. *J. Atmos. Ocean. Tech.*, 30(9):2132–2142.

Segalini, A. and Alfredsson, P. H. (2012). Techniques for the eduction of coherent structures from flow measurements in the atmospheric boundary layer. *Bound.-Lay. Meteorol.*, 143(3):433–450.

Shadden, S. C., Lekien, F., and Marsden, J. E. (2005). Definition and properties of Lagrangian coherent structures from finite-time Lyapunov exponents in two-dimensional aperiodic flows. *Physica D*, 212(3-4):271–304.

Stawiarski, C. (2014). *Optimizing Dual-Doppler Lidar Measurements of Surface Layer Coherent Structures with Large-Eddy Simulations*, volume 64. KIT Scientific Publishing Karlsruhe.

Stawiarski, C., Träumner, K., Knigge, C., and Calhoun, R. (2013). Scopes and challenges of dual-Doppler lidar wind measurements an error analysis. *J. Atmos. Ocean. Tech.*, 30(9):2044–2062.

Stawiarski, C., Träumner, K., Kottmeier, C., Knigge, C., and Raasch, S. (2015). Assessment of surface-layer coherent structure detection in dual-Doppler lidar data based on virtual measurements. *Bound.-Lay. Meteorol.*, 156(3):371–393.

Stull, R. B. (1988). *An introduction to boundary layer meteorology*, volume 13. Kluwer Dordrecht Boston London.

Takimoto, H., Inagaki, A., Kanda, M., Sato, A., and Michioka, T. (2013). Length-scale similarity of turbulent organized structures over surfaces with different roughness types. *Bound.-Lay. Meteorol.*, 147(2):217–236.

Tang, W., Chan, P. W., and Haller, G. (2011). Lagrangian coherent structure analysis of terminal winds detected by lidar. Part II: Structure evolution and comparison with flight data. *J. Appl. Meteorol.*, 50(10):2167–2183.

Theodorsen, T. (1952). Mechanisms of turbulence. In *Proceedings of the Midwestern Conference on Fluid Mechanics*.

Thom, A., Stewart, J., Oliver, H., and Gash, J. (1975). Comparison of aerodynamic and energy budget estimates of fluxes over a pine forest. *Q. J. R. Meteorol. Soc.*, 101(427):93–105.

Thomas, C. and Foken, T. (2005). Detection of long-term coherent exchange over spruce forest using wavelet analysis. *Theor. Appl. Climatol.*, 80(2):91–104.

Tipler, P. (2000). *Physik*. 3. korr. Nachdr. der 1. Aufl. Spektrum Akademischer Verlag GmbH Heidelberg.

Träumner, K., Damian, T., Stawiarski, C., and Wieser, A. (2015). Turbulent structures and coherence in the atmospheric surface layer. *Bound.-Lay. Meteorol.*, 154(1):1–25.

Träumner, K., Kottmeier, C., Corsmeier, U., and Wieser, A. (2011). Convective boundary-layer entrainment: Short review and progress using Doppler lidar. *Bound.-Lay. Meteorol.*, 141(3):369–391.

Wulfmeyer, V., Mayor, S., Spuler, X., Brewer, W., Hardesty, R., Rye, B., and Bollig, C. (2003). *Doppler lidar design study*. Institut für Physik und Meteorologie Universität Hohenheim, 109pp.

Young, G. S., Kristovich, D. A., Hjelmfelt, M. R., and Foster, R. C. (2002). Rolls, streets, waves, and more: A review of quasi-two-dimensional structures in the atmospheric boundary layer. *Bull. Amer. Meteo. Soc.*, 83(7):997–1001.

Zeeman, M. J., Eugster, W., and Thomas, C. K. (2013). Concurrency of coherent structures and conditionally sampled daytime sub-canopy respiration. *Bound.-Lay. Meteorol.*, 146(1):1–15.

List of Figures

List of Tables

Danksagung

Die Anfertigung dieser Arbeit wäre ohne die Unterstützung weiterer Personen nicht möglich gewesen. Daher möchte ich mich ganz herzlich bei allen Menschen bedanken, die mir während meiner Promotionszeit den Rücken frei gehalten haben, die mit mir Geduld hatten und - am allerwichtigsten - die an mich geglaubt haben.

Im Besonderen möchte ich Prof. Dr. Christoph Kottmeier danken, der in mich viel Vertrauen gesetzt hat und mir in sehr guten anregenden Gesprächen viele Ideen mit auf den Weg gegeben hat. PD Michael Kunz danke ich, dass er die Mühen eines Korreferats auf sich nimmt und auch dafür, dass er mir wertvolle Tipps für die Fertigstellung meiner Dissertation gab. Dr. Norbert Kalthoff und Dr. Katja Träumner bin ich sehr dankbar, dass sie mich während meiner Promotion fachlich wie auch persönlich unterstützt haben und ebenfalls sehr viele konstruktive Vorschläge mit eingebracht haben. Dr. Christina Stawiarski sei sehr gedankt für eine tolle Büroatmosphäre und für die Unterstützung in so vielen Bereichen. Also I'd like to thank PhD Robert Banta and PhD Aditya Choukulkar who supervised me during my time at the NOAA. I really liked to work at your institute and I enjoyed spending time with you!

Meinen Bürokollegen Sebastian Helgert und Alberto Caldaz-Alvarez danke ich für ein harmonisches Miteinander und für die vielen netten Gespräche am Schreibtisch. Generell bin ich sehr glücklich über die vielen privaten Unternehmungen, die ich mit meinen Kollegen, Mit-Doktoranden und Freunden am IMK erlebt habe. Danke euch allen. Ihr habt meine Promotionszeit zu etwas Besonderem werden lassen! Darüber hinaus vielen Dank an die Werkstadt, die mir während der HOPE Kampagne geholfen hat, einen tollen Datensatz an Messdaten zu erstellen. Dr. Andreas Wieser hat mir in Fragen bezüglich der Lidar-Messung

immer seine helfende Hand angeboten. Danke auch an Dr. Ulrich Corsmeier, Dr. Jan Handwerker, Bernhard Mühr und Dr. Luisa Röhner. Auch wenn wir während meiner Dissertation fachlich nicht an den gleichen Themen gearbeitet haben, seid ihr doch sehr wichtige Ansprechpartner für mich gewesen. Gabi Klinck hat mir bei technischen Fragen und bei Problemen mit der PC-Administration immer unterstützend zur Seite gestanden. Mit der Hilfe von Rosalba Gräbener, Friederike Schönbein, Doris Stenschke und Sylvia Deckert konnte ich kleine Probleme immer deutlich schneller lösen.

Selbst mit der besten fachlichen Unterstützung schreibt man nicht einfach so eine Dissertation. Danke an die vielen Stützen meines privaten Lebens. Markus, Christoph, Gabriel, danke dass ihr immer da wart, wenn ich mal wieder vor lauter Wald den Baum kaum sah. Markus, dir auch danke fürs Korrekturlesen und deine Karteikartensammlung. Ich möchte auch meinen Eltern und meiner Familie herzlich danken. Ihr habt mich speziell in der Endphase meiner Arbeit immer wieder aufgebaut und mir ein Ohr geschenkt, wenn ich es brauchte. Es ist so gut zu wissen, dass es euch alle gibt! Außerdem danke an alle meine Freunde, die immer und jederzeit für mich da waren. Ihr habt mir so viel gegeben und ich weiß, was ich an euch habe.

Der abschließende Dank gilt meiner Freundin Rike. Ich habe mit dir schon so viel erlebt und ohne dich wäre ich ein anderer Mensch. Ich freue mich auf das gemeinsame Leben mit dir und freue mich, auch wieder mehr Zeit mit dir verbringen zu können. Ich werde sie genießen. Danke, dass ich ein Teil deines Lebens sein darf!